Processing and Properties of Nanostructured Solid-State Energy Storage Devices

Chun Huang, Trinity College

Doctor of Philosophy, Michaelmas Term 2013

Abstract

A scalable spray processing technique was used to fabricate carbon nanotube (CNT)-based film electrodes and solid-state supercapacitors. The sprayed CNT-based electrodes comprised a randomly interconnected meso-porous network with a high electrical conductivity. Layer-by-layer (LbL) deposition of functionalised and oppositely charged single-wall carbon nanotubes (SWNTs) increased the electrode density and improved charging and discharging kinetics when compared with carboxylic functionalised only SWNT electrodes. The capacitance was further increased to 151 F g^{-1} at 2 mV s^{-1} and 120 F g^{-1} at 100 mV s^{-1} after vacuum and H_2 heat treatments that removed the functional groups, and resulted in a hybrid microstructure of SWNTs and multi-layer graphene sheets from unzipped SWNTs.

Flexible solid-state supercapacitors were fabricated by directly spraying multi-wall carbon nanotube (MWNT)-based aqueous suspensions onto both sides of a Nafion membrane and dried. A single cell with MWNT-only electrodes had a capacitance of 57 F g^{-1} per electrode at 2 mV s^{-1} and 44 F g^{-1} at 150 mV s^{-1}. Cells with MWNT/ionomer electrodes showed a higher H^+ mobility and a lower charge transfer resistance, and the capacitance increased to 145 F g^{-1} at 2 mV s^{-1} and 91 F g^{-1} at 150 mV s^{-1}.

Finally, MWNT/TiO_2 nanoparticle/ionomer hybrid electrodes were used in the same solid-state supercapacitor configuration and provided a capacitance of 484 F g^{-1} per electrode at 5 mV s^{-1} and 322 F g^{-1} at 100 mV s^{-1}. A qualitative model of the charge storage mechanism was developed, where TiO_2 promoted H^+ ions via redox reactions that fed protons into the proton-conducting ionomer coating over the MWNTs (in which the TiO_2 was embedded), while electrons were readily conducted through the MWNT scaffold. This solid-state supercapacitor provided both attractive energy (31.8 Wh kg^{-1}) and power (14.9 kW kg^{-1}) densities, where such high energy density is difficult to achieve for MWNTs alone and such high power density is difficult for metal oxides alone, especially in the solid state.

Processing and Properties of Nanostructured Solid-State Energy Storage Devices



Chun Huang

Doctor of Philosophy

Department of Materials

Trinity College

Michaelmas Term 2013

Acknowledgements

This DPhil thesis describes the research carried out by the author in the Department of Materials at the University of Oxford from October 2010 to October 2013, under the supervision of Professor Patrick Grant. This thesis would not have reached its present form without the help and support of many kind people. In what follows, grateful acknowledgements are given to everyone who assisted and inspired me throughout this work.

The author is grateful to KETEP and Professor Jong Min Kim for generous financial support and valuable advice; and to my research group for all the state-of-the-art and originally built laboratory facilities which otherwise would not have made my experiments possible.

Special thanks must go to my supervisor, Professor Patrick Grant, for all the inspiration of my research and investment of his time on my DPhil studies over the past few years. His diligence, thoroughness and research acumen will no doubt guide my future career. I would also like to thank Dr Colin Johnston, for many little discussions on my results which have helped shape my research.

I would like to thank the many members at Oxford University who have helped me during the course of this work, particularly Professor John Sykes for his guidance on elec-

trochemistry, Professor Malcolm Green for his suggestions on carbon nanotube steam purification, Professor Nicole Grobert for her advice on spectroscopy characterisation of carbon nanotubes, Dr Alison Crossley for her help on X-ray photoelectron spectroscopy, Dr Neil Young for his microscopy characterisation training, Dr Andrew Watt for the provision of some laboratory facilities and advice, and Mr Robin Vincent for his laboratory support.

I have been extremely lucky to have worked in a big friendly research group which has made my DPhil life happy. Many thanks go to Miss Laura O'Neill, Dr Enzo Liotti, Mr Amoghavarsha Mahadevegowda, Mr Mike Gorley, Dr Claire Dancer, Miss Yunqi Wang, Dr Atsushi Sato and Miss Qin Lei, all of them deserve a special mention.

Finally, I would like to thank my parents, for everything they have given me.

Contents

1 Introduction **1**

1.1 Background 1

1.2 Applications and markets for supercapacitors 4

1.3 Development and current challenges 7

1.4 Thesis objectives 9

2 Literature Review **15**

2.1 Two types of supercapacitors 15

2.1.1 Electric double layer capacitors 15

2.1.2 Pseudo-capacitors 21

2.2 Electrode materials 23

2.2.1 Activated carbon 23

2.2.2 Carbon nanotubes and their composites 25

2.2.3 Metal oxides and their composites 30

2.2.4 Polymers and their composites 37

2.3 Cell configuration 41

2.3.1 Symmetric cells 41
2.3.2 Asymmetric cells 43
2.3.3 Solid-state cells 44
2.4 Processing 49
2.4.1 Manufacture of commercial supercapacitors 49
2.4.2 Vacuum filtration 50
2.4.3 Electrophoretic deposition 51
2.4.4 Electrospinning 53
2.4.5 Electrostatic spray deposition 54
2.4.6 Atomisation spray deposition 56

3 Experimental Techniques **71**

3.1 Carbon nanotube treatment 71
3.1.1 Steam purification 72
3.1.2 Functionalisation 72
3.2 Electrode and supercapacitor fabrication 73
3.2.1 Suspension preparation 73
3.2.2 Spray deposition of electrodes 76
3.2.3 Spray deposition of flexible solid-state supercapacitors 77
3.3 Physical characterisation 79
3.3.1 Electrode thickness 79
3.3.2 Raman spectroscopy 80

3.3.3 X-ray photoelectron spectroscopy 80
3.3.4 Scanning electron microscopy 80
3.3.5 Transmission electron microscopy 81
3.4 Electrochemical characterisation 82
3.4.1 Cyclic voltammetry 82
3.4.2 Galvanostatic charge/discharge 84
3.4.3 Electrochemical impedance spectroscopy 86
3.4.4 Cycling 86

4 Layer-by-layer spray deposition and heat treatments of single-wall carbon nanotube-based thin film electrodes for supercapacitors 89

4.1 Introduction 89
4.2 Materials and methods 92
4.2.1 LbL spray deposition of functionalised SWNTs 92
4.2.2 Characterisation 93
4.3 Results and discussion 94
4.3.1 Surface chemistry and density of functionalised SWNT electrodes 94
4.3.2 Electrical conductivity of SWNT-based electrodes 100
4.3.3 Electrochemical properties of SWNT-based electrodes 101
4.3.4 Microstructure of SWNT-based electrodes 106
4.4 Conclusions 114

5 Spray processing of multi-wall carbon nanotube-based solid-state su-

percapacitors **121**

5.1 Introduction 121

5.2 Materials and methods 125

5.2.1 Fabrication of solid-state supercapacitors by spray deposition . . 125

5.2.2 Characterisation 126

5.3 Results and discussion 127

5.3.1 MWNT-only electrode in an aqueous electrolyte 127

5.3.2 Solid-state supercapacitor with MWNT-only electrodes 128

5.3.3 Solid-state supercapacitor with MWNT/ionomer electrodes . . . 132

5.3.4 Solid-state supercapacitor devices made of cell stacks 143

5.4 Conclusions 147

6 Spray processing of TiO_2 nanoparticle/ionomer coatings on carbon nanotube scaffold-based electrodes for solid-state supercapacitors **156**

6.1 Introduction 156

6.2 Materials and methods 159

6.2.1 Fabrication of MWNT/TiO_2/ionomer solid-state supercapacitors by spray deposition 159

6.2.2 Characterisation 160

6.3 Results and discussion 161

6.3.1 Electrode surface chemistry 161

6.3.2 Electrode microstructure 164

6.3.3 Electrochemical characterisation of the solid-state supercapacitor 164

6.4 Conclusions 175

7 Conclusions and Future Work **182**

7.1 Conclusions 182

7.2 Suggestions for future work 185

List of Figures

1.1 A Ragone plot for various energy storage and conversion devices [5] © 2013 Elsevier. 3

2.1 A schematic diagram of an EDL capacitor with charge separation taking place between the electrode surface and the solvated ions in the solution near the electrode interface. 16

2.2 Schematic diagrams of the EDL charge storage interface according to (a) Helmholtz model; (b) Gouy-Chapman model; and (c) Stern model, where IHP is the inner Helmholtz plane and OHP is the outer Helmholtz plane [5] © 2009 Royal Society of Chemistry. 17

2.3 A schematic diagram of the inside porous structure of AC particles [10] © 2002 Elsevier. 24

2.4 (a) Scanning electron micrograph (SEM) of the dip deposited MWNT network. Reprinted with permission from [22]. Copyright (2009) American Chemical Society; (b) cyclic voltammogram (CV) of a MWNT electrode in 6 M KOH at 1 mV s^{-1} [23] Copyright (2000) AIP Publishing LLC; and (c) CVs of various functionalised MWNTs in 1 M H_2SO_4 at 1 mV s^{-1}, where c-MWNT is carboxylic functionalised MWNT, p-MWNT is purified MWNT, b-MWNT is butyl functionalised MWNT, o-MWNT is octyl functionalised MWNT and d-MWNT is dodecyl functionalised MWNT [24] Copyright (2005) AIP Publishing LLC. 27

2.5 MnO_2/CNT hybrid co-axial nanotubes: (a) low and (b) high resolution SEM images showing the co-axial nature of the nanotube; and (c) SEM image and a schematic representation of a single co-axial nanotube [26] © 2012 John Wiley and Sons. 31

2.6 (a) SEM image showing aligned CNT/AuNW segments and the Cu back layer; (b) high resolution SEM image showing the interface between the CNT and AuNW segments; (c) TEM image showing the CNT/AuNW interface; and (d) high resolution TEM image showing the graphitic walls of CNT, approximately 15 nm thick. A schematic diagram of a single hybrid nanowire is shown [26] © 2012 John Wiley and Sons. 32

2.7 (a) SEM image of a spray deposited Fe_3O_4 nanoparticle film; (b) TEM image of the Fe_3O_4 nanoparticles; (c) SEM image of a spray deposited Fe_3O_4 nanorod film; (d) TEM image of the Fe_3O_4 nanorods; (e) SEM image of a spray deposited Fe_3O_4 nanowire film; and (f) TEM image of the Fe_3O_4 nanowires. The inset in (b) shows the octahedral Fe_3O_4 nanoparticles at higher magnification with diameter of *ca.* 100 nm. The inset in (f) shows a high resolution TEM image of a Fe_3O_4 nanowire [33] © 2010 Royal Society of Chemistry. 35

2.8 A schematic diagram of redox deposition under "poorly controlled" (left) versus "self-limiting" (right) conditions. Reprinted with permission from [40]. Copyright (2013) American Chemical Society. 38

2.9 (a) A schematic diagram of a commercial spirally wound supercapacitor; (b) an assembled device weighing 500 g and rated for 2600 F; and (c) a small button cell of 1.6 mm in height that stores 5 F. Both (b) and (c) operate at 2.7 V [11] © 2008 Nature Publishing Group. 42

2.10 Schematic representation of CVs for three different configurations of aqueous-based supercapacitors in which areas shaded in red and blue represent the potential window of the positive and negative electrodes, respectively for: (a) symmetric $MnO_2//MnO_2$ in 0.5 M K_2SO_4; (b) asymmetric MnO_2//AC in 0.5 M K_2SO_4; and (c) asymmetric PbO_2//AC in 1 M H_2SO_4 [8] © 2011 Cambridge University Press. 45

2.11 A schematic diagram of doctor blade processing by which 40-200 μm thick carbon films are produced. 50

2.12 Surface morphology of the buckypaper of a mixture of SWNTs and CNFs with a weight ratio of (a) 1:3; and (b) 1:5 [62] © 2010 Elsevier. 52

2.13 A schematic diagram of simple electrophoretic deposition processing. . 53

2.14 (a) Electrospinning technique (left) is used to make nylon 6,6 fibre mats of 200-250 mm diameter (right); and (b) a schematic representation and top-down (centre column) and cross-sectional (right) SEMs of the fabricated nylon 6,6 fibre mat [66] © 2009 Nature Publishing Group. 55

2.15 A schematic diagram of electrostatic spray deposition system [67] © 2006 Elsevier. 57

3.1 A schematic diagram of the spray deposition configuration. 77

3.2 (a) Nozzle parts; and (b) a schematic diagram of the five ports directed to the main nozzle body. 78

3.3 (a) A Swagelok cell used for the full cell electrochemical tests; and (b) a stack of three solid-state supercapacitors which was simply exposed to air without any packaging during testing. 83

4.1 X-ray photoelectron spectroscopy (XPS) wide scan spectra of the as-sprayed SWNT electrode with SDBS surfactant; as-sprayed SWNT-COOH electrode; as-sprayed LbL SWNT-COOH/SWNT-NH_2 electrode; and the LbL electrode after heating in vacuum at 150 ^{o}C and H_2 at 300 ^{o}C. . . 95

4.2 X-ray photoelectron spectroscopy detailed scan spectra from the various sprayed SWNT-based electrodes: (a) C_{1s} for SWNT-COOH; (b) N_{1s} for SWNT-COOH; (c) N_{1s} for SWNT-NH_2; and (d) N_{1s} for LbL SWNT-COOH/SWNT-NH_2 after heating in vacuum at 150 ^{o}C for 30 mins. . . 97

4.3 Cyclic voltammograms of the SWNT-based electrodes in 1 M H_2SO_4: (a) as-sprayed steam purified SWNT; (b) as-sprayed SWNT-COOH; (c) as-sprayed LbL SWNT-COOH/SWNT-NH_2; and (d) LbL SWNT-COOH/SWNT-NH_2 after vacuum and H_2 heat treatments. 102

4.4 A summary of specific capacitance of the SWNT-based electrodes in 1 M H_2SO_4 over a wide range of scan rates. 105

4.5 Scanning electron micrographs of the SWNT-based electrodes: (a) plan view of the as-sprayed SWNT network; (b) plan view of the as-sprayed SWNT-COOH network; (c) plan view of the LbL SWNT-COOH/SWNT-NH_2 electrode after heating in vacuum at 150 ^{o}C for 30 min; (d) cross-section view of the interface between the as-sprayed LbL SWNT-COOH/SWNT-NH_2 electrode and the substrate; and (e) plan view of the LbL electrode after heating in vacuum at 150 ^{o}C for 30 mins and in H_2 at 300 ^{o}C for 2 hrs. 108

4.6 TEM images: (a) nanoplate from the LbL electrode after vacuum and H_2 heating; (b) the edge of the nanoplate, where a selected area aperture has been inserted, diffraction pattern was taken. 109

4.7 (a) Electron diffraction pattern of multi-layer graphene with the peaks labelled by Miller-Bravais indices; (b) diffracted intensity taken along the 1-210 to -2110 axis for the pattern shown in (a). 110

4.8 (a) High-angle annular dark-field (HAADF) image of the LbL electrode after vacuum and H_2 heating, where a region of interest was drawn to measure intensities over an area (the width of the rectangle was 10 pixels); and (b) an example of intensity histograms obtained from A to B, 20 intensity profiles were obtained and the average calculated. 111

4.9 Schematic of the as-sprayed LbL electrode, and the hybrid structure of SWNT/multi-layer graphene sheets after post-spray treatments. 114

5.1 (a) A flexible Nafion membrane covered with spray deposited MWNT-based electrodes on both sides; (b) a schematic diagram of the fabricated solid-state supercapacitor full cell including Cu foil current collectors; and (c) a fabricated simple "stack" of three solid-state supercapacitor cells and the corresponding schematic diagram. 124

5.2 (a) Cyclic voltammograms for a MWNT-only electrode fabricated by spraying in 0.5 M H_2SO_4; (b) the corresponding DC galvanostatic charge/discharge curves at 1 A g^{-1}; (c) Nyquist plot for the MWNT-only electrode fabricated by spraying in DI water; and (d) Nyquist plot for the MWNT-only electrode fabricated by spraying in 0.5 M H_2SO_4, all tested in 1 M H_2SO_4 in a three-electrode configuration. 129

5.3 (a) Cyclic voltammograms of a full cell membrane-based solid-state supercapacitor with MWNT-only electrodes; (b) the same cyclic voltammograms normalised by the square root of the scan rate; (c) DC galvanostatic charge/discharge curves of the same solid-state supercapacitor at 1 A g^{-1}; and (d) the complementary Nyquist impedance plot. 131

5.4 (a) Scanning electron micrograph of the spray deposited MWNT/ionomer hybrid electrode; and (b) transmission electron micrograph of the MWNTs with an ionomer coating. 133

5.5 (a) Cyclic voltammograms of a full cell membrane-based solid-state supercapacitor with MWNT/ionomer electrodes; (b) the same voltammograms normalised by the square root of the scan rate; (c) a plot of redox peak height from the voltammograms in (a) against square root of scan rate; (d) DC galvanostatic charge/discharge curves of the same solid-state supercapacitor at 1 A g^{-1}; and (e) the complementary Nyquist impedance plot. 135

5.6 (a) Equivalent circuit model that the Nyquist plots of solid-state supercapacitors were fitted to; and (b) Nyquist impedance plot for the solid-state supercapacitor with MWNT/ionomer hybrid electrodes and the fitted data according to the equivalent circuit model in (a). 137

5.7 (a) DC galvanostatic charge/discharge curves charged to 2 V at 1 A g^{-1} for a full cell solid-state supercapacitor with MWNT/ionomer electrodes; and (b) specific energy and power densities against an increasing voltage window from 2 to 2.7 V. 142

5.8 A schematic diagram of a full cell solid-state supercapacitor with a detailed structure of the MWNT/ionomer hybrid electrodes. 144

5.9 (a) Cyclic voltammograms of a stack of two solid-state supercapacitors connected through Cu foils at a variety of scan rates; and (b) DC galvanostatic charge/discharge curves of a stack of three solid-state supercapacitors charged to 3 V at a current density of 2 A g^{-1}. 145

6.1 An as-sprayed 18 cm x 10 cm flexible solid-state supercapacitor (before addition of Cu foil current collectors). 158

6.2 Raman spectra for an as-sprayed MWNT-only electrode and an as-sprayed MWNT/anatase TiO_2 electrode. 162

6.3 XPS spectra of (a) wide scan for the as-received TiO_2 powder; (b) wide scan for the as-sprayed MWNT/TiO_2/ionomer electrode. 163

6.4 XPS spectra of (a) detailed Ti_{2p} scan for the as-received TiO_2 nanoparticles; and (b) detailed O_{1s} scan for as-received TiO_2 powder, as-sprayed MWNT/TiO_2/ionomer electrode and dried then rehydrated MWNT/TiO_2/ionomer electrode. 165

6.5 (a) SEM image of the as-sprayed MWNT/TiO_2/ionomer electrode; (b) TEM image of the electrode; and (c) HRTEM image of the MWNTs and a TiO_2 nanoparticle partially covered with an ionomer coating. 166

6.6 (a) Cyclic voltammograms of a solid-state supercapacitor with MWNT/TiO_2/ionomer electrodes; and (b) cyclic voltammograms of the same solid-state supercapacitor after 300 cycles when the hydroxyl group reaction faded. . . . 168

6.7 (a) Galvanostatic charge/discharge cycles of a solid-state supercapacitor with MWNT/TiO_2/ionomer electrodes at 1 A g^{-1}; and (b) galvanostatic charge/discharge curves of the symmetric solid-state supercapacitors with MWNT/TiO2/ionomer, MWNT/ionomer and MWNTs-only electrodes, all at 1 A g^{-1}. 169

6.8 (a) Nyquist plot of a solid-state supercapacitor with MWNT/TiO_2/ionomer electrodes between 10^6 Hz and 0.01 Hz under normal light; (b) a graph of imaginary part of the capacitance vs frequency from the EIS results in (a) to estimate relaxation time τ_0; and (c) Nyquist plots in the high frequency region of a solid-state supercapacitor with MWNT/TiO_2/ionomer electrodes tested under a Xenon lamp and in darkness. 170

6.9 (a) Cyclic voltammograms of the a solid-state supercapacitor immediately after dehydrating in vacuum at 105 ^{o}C for 16 hrs; (b) cyclic voltammograms of (a) after exposing to laboratory air on the bench for 3 hrs; (c) cyclic voltammograms of (a) after rehydrating over steam for 2 hrs; and (d) a plot of CV normalised peak current in (c) against the square root of scan rate. 173

6.10 A Ragone plot of power density against energy density for supercapacitors and LiBs, and different types of solid-state supercapacitor performances taken from the literature, where PANI is an abbreviation of polyaniline [21], PEDOT is poly(3,4-ethylenedioxythiophene) [22] and PAAK is potassium polyacrylate [23]. 174

6.11 A schematic diagram of the MWNT/TiO_2/ionomer solid-state supercapacitor full cell and the hybrid electrode structure in detail to show the pseudo-capacitive reaction in the TiO_2 nanoparticle to generate H^+, which was transported by the ionomer coating on both of the nanoparticles and MWNTs. 176

List of Tables

2.1 A summary of the commercially available EDL capacitors [6] 20

3.1 A summary of the suspensions for the four types of electrode materials used in this thesis. 75

4.1 A summary of the SWNT-based electrodes prepared by spray deposition, their heat treatments, densities and electrical conductivities after the heat treatments (LbL is an abbreviation of layer-by-layer assembly of ten alternating layers of SWNT-COOH and SWNT-NH_2). 99

5.1 Components of the equivalent circuit fitted for the impedance spectra for the solid-state supercapacitors with MWNT/ionomer hybrid electrodes and MWNT-only electrodes. 138

5.2 A summary of the performances of MWNT-based electrodes in 1 M H_2SO_4 and in a solid-state symmetrical membrane-based cell configuration. All values were calculated per electrode. 141

Chapter 1

Introduction

1.1 Background

Limited natural resources, concerns over environmental pollution and increasing fuel prices stimulate an increasing demand for renewable energy resources and more efficient energy management. Energy storage is a key component in the energy conversion-storage-delivery chain and electrical energy storage systems are one of the most important [1]. The high demand for compact and efficient electrical energy storage devices have led to the innovation and development of batteries and electrochemical capacitors (also called supercapacitors) [2].

Batteries store charge in bulk electrodes at a constant potential where electron transfer takes place in the electroactive materials through redox and or intercalation reactions. Among the most promising batteries are lithium ion batteries (LiBs) that offer a high

energy density and a relatively high power density. Supercapacitors store charge mainly by electrostatic adsorption of electrolyte ions on a high electrode surface area (1000-3000 $m^2\ g^{-1}$). Although LiBs have higher specific energy (70-100 Wh kg^{-1}) than supercapacitors (5 Wh kg^{-1}), supercapacitors exhibit higher specific power (5-10 kW kg^{-1}) than LiBs (0.5-1 kW kg^{-1}) [3], and have a very high cycle life of 10^6 compared with typically 3,000 cycles for LiBs. At short charging times below 10 s, supercapacitors capture more specific energy than LiBs, and can discharge approximately 95% of the stored energy within seconds [4]. On the other hand, supercapacitors provide 2-3 orders of magnitude higher energy density than conventional electrostatic capacitors due to the very large electrode surface area. Fig. 1.1 is a Ragone plot showing the supercapacitors filling the gap between batteries and conventional electrostatic capacitors in terms of the specific energy versus specific power.

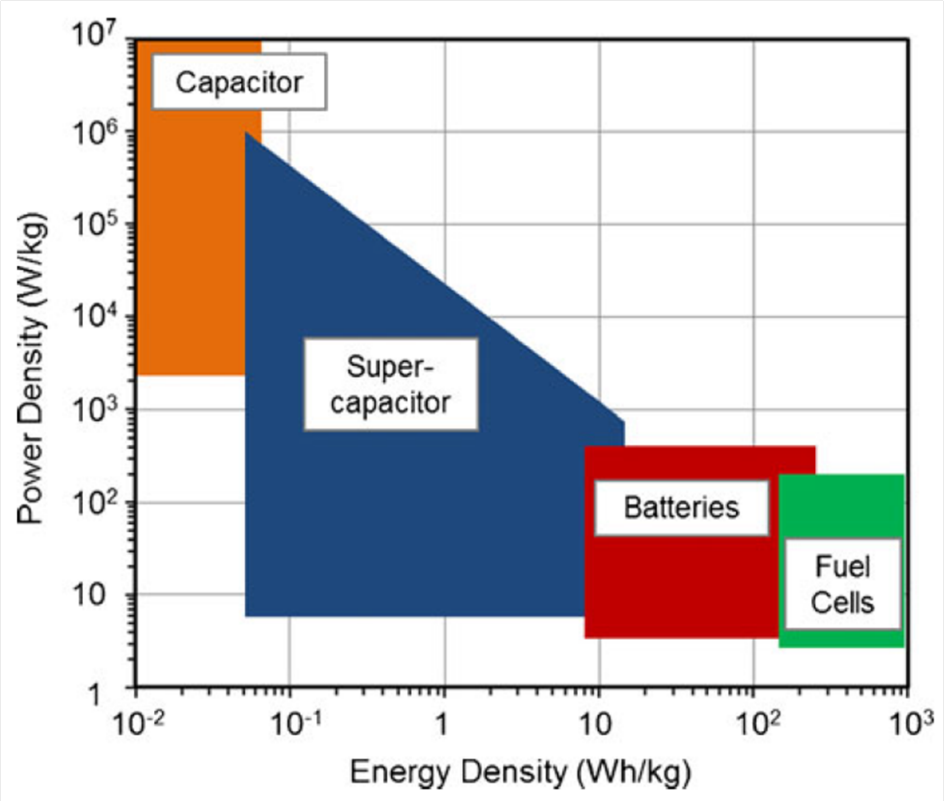


Figure 1.1: A Ragone plot for various energy storage and conversion devices [5] © 2013 Elsevier.

1.2 Applications and markets for supercapacitors

Current supercapacitor applications mainly focus on their high power properties. At a large scale, supercapacitors have been proposed for bulk energy storage in smart grid to store off-peak electricity at a range of timescales from a few seconds to minutes to replace "spinning reserve" for imbalances in load and generation. A successful realisation of this bulk storage concept could mean that approximately 20% of the energy needed during the day would be stored from the evening before, and translates into a more efficient use of the distribution system with less investment in extra production capacity just to accommodate transitory peak loads [4]. Most storage media such as lead acid batteries or LiBs are too expensive with a low cycle life and concerns over flammability for this purpose [4].

A high power capability, such as provided by supercapacitors, is very attractive for energy regenerative systems, where the system needs to be capable of efficiently storing energy during relatively short times when available; and then releasing energy when needed. For example, a hybrid diesel-electric gantry crane that uses supercapacitor energy storage to couple with diesel engines, so that the supercapacitor captures energy during lowering movement, which would otherwise be wasted as heat, and uses this energy in the next repetitious up movement of carrying heavy shipping containers, saving ∼40 % fuel and associated emissions [4].

Supercapacitors are used in emission-free electric vehicles (EVs), which have been popular due to the environmental concerns arising from the generation of "greenhouse gases" by vehicles burning carbonaceous fuels. Supercapacitors have been used to power all-electric city buses, which can store ∼8 kWh energy and require a limited range of only ∼15 km. The buses need to be charged at the end of each circuit, which takes less than 15 min to achieve, and experience hundreds of start/stop cycles during a day [6]. Supercapacitor-powered buses are in operation in Shanghai using an extended charging arm over each bus stop to charge for ∼20 s, after which the bus proceeds to the next stop [6].

Much attention has been directed to the development of hybrid EVs with a combination of LiBs and supercapacitors to balance energy and power delivery. The supercapacitor meets peak power demands during acceleration and up-hill driving while the LiB size can be reduced, and operates in the "cruise", extending battery life and range. This concept arises from the perceived high power density of the supercapacitor – although at a relatively low energy density – and the high energy density of the LiB, so the hybrid combination has a better overall power and energy density performance than either component alone. However, additional power electronics are required to manage the duty between the two energy storage device types. Another type of EV uses a combination of fuel cell and supercapacitor where the fuel cell generates electrical energy from onboard stored hydrogen, hydrogen-rich gases or liquid fuels such as methanol [7], and the supercapacitor prevents a high voltage drop (fuel starvation) caused by

fast energy demand over occasional short time periods [8], which would be otherwise hazardous for the fuel cell stack [9]. Supercapacitors can also capture recovered energy during braking cycles to power the next acceleration: normal braking lasts from 5 to 10 s, which is the total time span available for kinetic energy to be captured and stored, which fits well with their inherent fast charging property. A light-rail electric train with an onboard supercapacitor storage system can store regenerated braking energy and for train stations separated by 4 km, ∼30 % energy savings are achieved [6].

Current small volume supercapacitor applications include stand-by power for random access memory (RAM) devices and elements for long time-constant circuits [2]. Portable electronic devices such as notebook computers, wearable displays, electronic skins and some medical implantable devices are increasingly seeking thin, lightweight and flexible energy storage technologies to enable future designs [10] [11]. The primary energy storage technologies for these existing designs are LiBs, although there are niche applications emerging for higher power density but lower energy density supercapacitors [2, 12, 13]. As the size of the implantable medical devices decreases to millimeter scales and beyond, current liquid electrolyte-based batteries are far too big for the available volume [14]. Flexible solid-state supercapacitors in the form of size-tailorable thin films and with no packaging requirements to contain any liquid electrolytes may offer some benefits in some of these applications.

In summary, supercapacitors are playing an increasingly important role in energy har-

vesting and portable electronics. Although the current supercapacitors represent only ∼1% of the world market for electrical energy storage, an approximate 11% annual growth rate of supercapacitor market has been achieved since 2010, and it is expected that over £877m worldwide sales will be generated from this market by 2014 [15].

1.3 Development and current challenges

The first supercapacitor product was introduced into market for a memory back-up device by Nippon Electric Company (NEC) in 1979 [2]. In the last two decades, the developments in pseudo-capacitance, electrochemically active polymer electrodes and organic and ionic liquid electrolytes have assisted supercapacitors to play an increasingly important role as mentioned in Section 1.2.

The majority of current commercial supercapacitor electrodes use activated carbon (AC) due to its large surface area ($\sim$ 2000 m^2 g^{-1} [16]) and low cost (\$50-100 kg^{-1} [17]), and their fabrication method is based on doctor blading of an AC paste mixture with binders and conductivity enhancers onto a current collector. Although these supercapacitors dominate commercial applications and provide many attractive performance characteristics, as the potential for new supercapacitor applications grow, some aspects are limiting. In particular, the need to use binders to hold the AC electrode together, carbon black additions to improve electrical conductivity, constant porosity through-

out, and the inability to process nanoscale materials especially with aspect ratio >1, undermind performance. Nanomaterials have the potential for improving performance through a larger charge storage capacity and a higher contribution of active material in a confined volume. A key research challenge is therefore to select a suitable material or composite, which will bring the supercapacitor energy density closer to that of batteries without compromising the high power density. A key strategy in this respect is the use of "pseudo-capacitor" materials that show some battery-like behaviour, but usually only in the near surface region.

Doctor blading has several disadvantages including the capability of only making relatively thick (40-200 μm) electrodes, a low active material utilisation efficiency and a poor control over the electrode structure and morphology, although this method is cheap, robust and scalable. A new or modified scalable processing technique that can produce homogeneously distributed nanomaterial-based electrodes with controlled structure and morphology to tailor the performance, without an impractical surge in cost, might enable new supercapacitor materials beyond AC - especially pseudo-capacitors.

Finally, commercial supercapacitors use Li-ion-containing organic liquid electrolytes, very similar to those used in a LiB. This provides a high working voltage window ($\sim$3 V) that boosts energy density, but has some restrictions relating to the inherent flammability of the resulting supercapacitor, and some costs associated with fabrication in the necessarily moisture-free environment. Aqueous electrolytes reduce the operat-

ing voltage window (∼1 V), but offer higher inherent safety. Solid-state electrolytes are safer still and obviate expensive packaging, but ion mobilities are normally considered too slow to be useful. However, fine scale materials combined with thin solid-state electrolytes using novel process opportunities may be attractive.

1.4 Thesis objectives

Flexible atomisation spray processing technique has been developed at Oxford University for the manufacture of electrodes [18, 19, 20, 21] and is used in this thesis. The first objective is to investigate if this process can be modified to offer a degree of control over the resulting density and microstructure of the fabricated nanomaterial-based electrodes by spray processing. Although the spray processing route has already been shown to be attractive, especially for nanomaterials, there has been no attempt to manipulate resulting microstructure by physical or chemical manipulations in the process. Manufactured electrodes are characterised using a range of microscopy and electrochemical testing to explore the process-microstructure-performance combinations and to understand how microstructural manipulations for better performance can be achieved.

The second objective is to fabricate thin and flexible solid-state supercapacitors by spray deposition for the first time, and this time to characterise full supercapacitor cells to understand the charge storage mechanisms within the solid-state cells, and to

compare them with more conventional liquid electrolyte equivalents.

The third objective is to explore and optimise the energy and power densities of flexible solid-state supercapacitors by using the spray process to achieve novel combinations of different nanomaterials, opening the potential for their use in portable and wearable electronic applications.

Bibliography

[1] P. Simon and Y. Gogotsi, "Materials for electrochemical capacitors," *Nature Materials*, vol. 7, no. 11, pp. 845–854, 2008.

[2] B. E. Conway, *Electrochemical Supercapacitors, Scientific Fundamentals and Technological Applications*. Kluwer Academic / Plenum Publishers, 1999.

[3] P. J. Hall, M. Mirzaeian, S. I. Fletcher, F. B. Sillars, A. J. R. Rennie, G. O. Shitta-Bey, G. Wilson, A. Cruden, and R. Carter, "Energy storage in electrochemical capacitors: designing functional materials to improve performance," *Energy & Environmental Science*, vol. 3, no. 9, pp. 1238–1251, 2010.

[4] J. R. Miller and P. Simon, "Materials science - electrochemical capacitors for energy management," *Science*, vol. 321, no. 5889, pp. 651–652, 2008.

[5] G. Yu, X. Xie, L. Pan, Z. Bao, and Y. Cui, "Hybrid nanostructured materials for high-performance electrochemical capacitors," *Nano Energy*, vol. 2 (2), pp. 213–234, 2013.

[6] F. Beguin and E. Frackowiak, eds., *Supercapacitors - Materials, Systems, and Applications*. Wiley-VCH, 2013.

[7] S. R. Phatiphat Thounthong, "The benefits of hybridization," *IEEE Industrial Electronics Magazine*, vol. 25, pp. 26–37, 2009.

[8] A. V. W. Schmittinger, "A review of the main parameters influencing long-term performance and durability of pem fuel cells," *Journal of Power Sources*, vol. 180, pp. 1–14, 2008.

[9] B. E. Conway and W. G. Pell, "Double-layer and pseudocapacitance types of electrochemical capacitors and their applications to the development of hybrid devices," *Journal of Solid State Electrochemistry*, vol. 7, no. 9, pp. 637–644, 2003.

[10] T. H. Kim, K. S. Cho, E. K. Lee, S. J. Lee, J. Chae, J. W. Kim, D. H. Kim, J. Y. Kwon, G. Amaratunga, S. Y. Lee, B. L. Choi, Y. Kuk, J. M. Kim, and K. Kim, "Full-colour quantum dot displays fabricated by transfer printing," *Nature Photonics*, vol. 5, pp. 176–182, 2011.

[11] J. Bae, Y. J. Park, M. Lee, S. N. Cha, Y. J. Choi, C. S. Lee, J. M. Kim, and Z. L. Wang, "Single fiber based hybridization of energy converters and storage units using graphene as electrodes," *Advanced Materials*, vol. 23 (30), pp. 3446–3449, 2011.

[12] K. T. Nam, D. Kim, P. J. Yoo, C. Y. Chiang, N. Meethong, P. T. Hammond, Y. M. Chiang, and A. M. Belcher, "Virus-enabled synthesis and assembly of nanowires for lithium ion battery electrodes," *Science*, vol. 312, pp. 885–888, 2006.

[13] K. Naoi, W. Naoi, S. Aoyagi, J.-I. Miyamoto, and T. Kamino, "New generation "nanohybrid supercapacitor"," *Accounts of Chemical Research*, vol. 46 (5), pp. 1075–1083, 2013.

[14] C. Meng, O. Z. Gall, and P. P. Irazoqui, "A flexible super-capacitive solid-state power supply for miniature implantable medical devices," *Biomed Microdevices*, vol. DOI 10.1007/s10544-013-9789-1, 2013.

[15] G. Wang, L. Zhang, and J. Zhang, "A review of electrode materials for electrochemical supercapacitors," *Chemical Society Reviews*, vol. 41, pp. 797–828, 2012.

[16] E. Frackowiak and F. Beguin, "Carbon materials for the electrochemical storage of energy in capacitors," *Carbon*, vol. 39, no. 6, pp. 937–950, 2001.

[17] A. Burke, "Ultracapacitors: why, how, and where is the technology," *Journal of Power Sources*, vol. 91, pp. 37–50, 2000.

[18] X. Zhao, B. T. T. Chu, B. Ballesteros, W. Wang, C. Johnston, J. M. Sykes, and P. S. Grant, "Spray deposition of steam treated and functionalized single-walled and multi-walled carbon nanotube films for supercapacitors," *Nanotechnology*, vol. 20, no. 6, 2009.

[19] B. Mendoza-Sanchez, B. Rasche, V. Nicolosi, and P. S. Grant, "Scaleable ultra-thin and high power density graphene electrochemical capacitor electrodes manufactured by aqueous exfoliation and spray deposition," *Carbon*, vol. 52, pp. 337–346, 2012.

[20] C. Huang, N. Grobert, A. A. R. Watt, C. Johnston, A. Crossley, N. P. Young, and P. S. Grant, "Layer-by-layer spray deposition and unzipping of single-wall carbon nanotube-based thin film electrodes for electrochemical capacitors," *Carbon*, vol. 61, pp. 525–536, 2013.

[21] C. Huang and P. S. Grant, "One-step spray processing of high power all-solid-state supercapacitors," *Scientific Reports*, vol. 3 : 2393, p. DOI: 10.1038/srep02393, 2013.

Chapter 2

Literature Review

In this literature review, two main types of supercapacitors – electric double layer (EDL) capacitors and pseudo-capacitors – will be discussed. This review will focus on the materials selection for the electrodes, and the associated processing techniques that may contribute to their economic manufacture on a near-industrial scale.

2.1 Two types of supercapacitors

2.1.1 Electric double layer capacitors

Electric double-layer (EDL) capacitors store charge electrostatically by ion adsorption onto the interface between an electrolyte and a porous high surface area carbon-based electrode. EDL capacitors contain one positive electrode with electron deficiency, one negative electrode with electron excess and an insulating, porous separator, normally

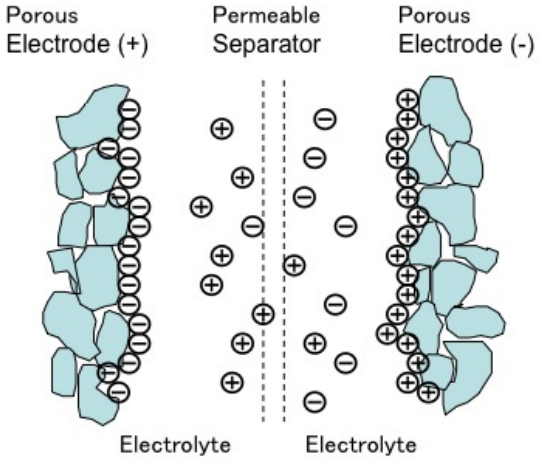


Figure 2.1: A schematic diagram of an EDL capacitor with charge separation taking place between the electrode surface and the solvated ions in the solution near the electrode interface.

immersed in a liquid electrolyte (Fig. 2.1). During charging, electrons are transferred from the positive electrode to the negative electrode from an external current source and a layer of positive charges formed at the internal surface of one electrode causes attraction of negative ions from the electrolyte to form the Helmhotz double layer, while a layer of negative charges at the internal surface of the other electrode causes attraction of positive ions from the electrolyte [1]. During discharging, the electrons shift from the negative electrode to the positive electrode through an external load, and the ions return from the electrode surface into the volume of electrolyte.

To study the charge storage interface futher, a Helmholtz model can be assumed that consists of two array layers of opposite charges, separated by a small distance d (0.05 - 0.2 nm [2]), and facing each other [3] (Fig. 2.2(a)). On the electrode side, a controllable surface density of excess positive (or negative) charges arises and the gradient of electron

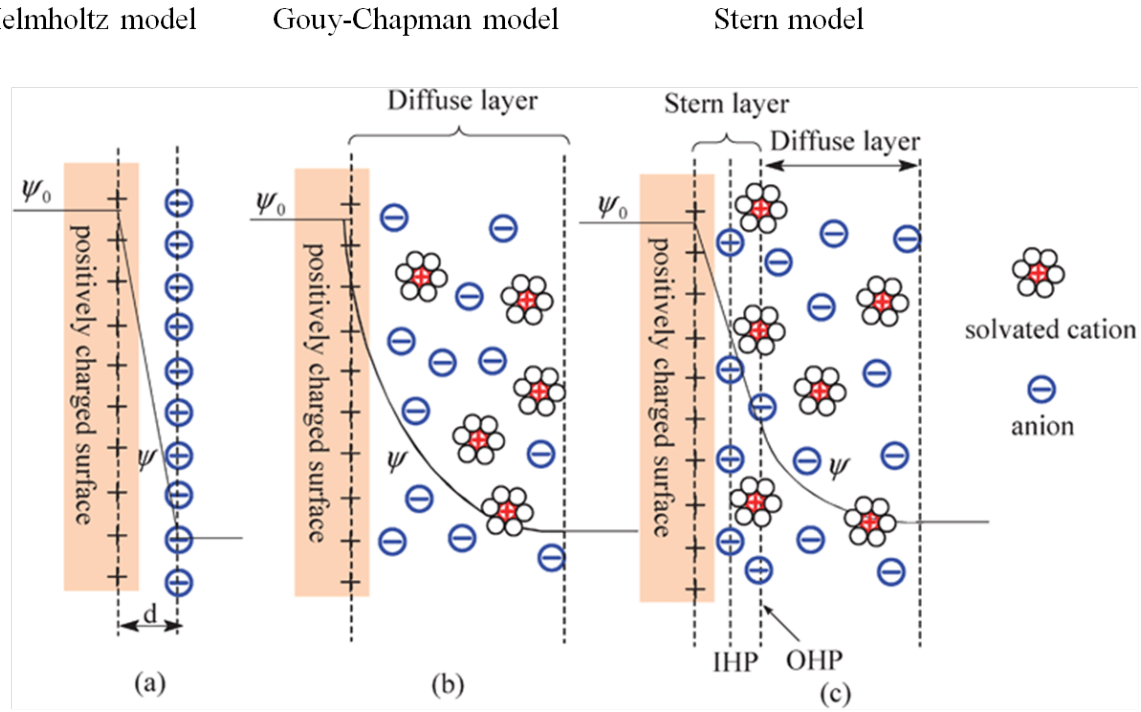


Figure 2.2: Schematic diagrams of the EDL charge storage interface according to (a) Helmholtz model; (b) Gouy-Chapman model; and (c) Stern model, where IHP is the inner Helmholtz plane and OHP is the outer Helmholtz plane [5] © 2009 Royal Society of Chemistry.

density at a charged metal interface is highly localised. The finite size of ions from the electrolyte determines their distance of closest approach to the electrode surface. The dipoles of these adsorbed solvent ions and their potential-dependent orientations in the double layer determine the capacitance [3]. The Gouy-Chapman model introduced a diffuse layer where the counter charge is permitted to come near to the electrode surface (Fig. 2.2(b)), and the Stern model in Fig. 2.3(c) combines these two models together [4].

As shown in Equation 2.1, capacitance C depends on the surface area S of the electrode material and the thickness d of the double layer, where ε equals the electric constant ε_0

(8.85 x 10^{-12} m^{-3} kg^{-1} s^4 A^2) times the relative dielectric constant of the electrolyte ε_r. Therefore, capacitance can be improved with large surface area and minimised thickness.

$$C = \frac{S\varepsilon}{d} \tag{2.1}$$

As mentioned above, the charged electrolyte ions are localised at the electrode surface over a distance of 0.05 to 0.2 nm plus a diffusion layer, so a suitable value of d is normally taken as 0.5 nm [4]. To measure ε_r, pure water is placed between the plates of a parallel plate capacitor and the capacitance is determined [4]. In an electric field between the electrode and outer Helmholtz plane, only a small fraction of water dipoles are free to rotate and change orientations with the field, and ε_r is estimated to have an average value of 10 [4].

Equation 2.2 shows the specific capacitance C also depends upon the extent of charge acceptance of the electrode $\triangle q$ and the change of potential $\triangle V$.

$$C = \frac{d(\triangle q)}{d(\triangle V)} \tag{2.2}$$

Commercial EDL capacitors use high surface area porous carbon ($\sim$2000 m^2 g^{-1}) as electrodes, and non-aqueous electrolytes such as tetraethylammonium tetrafluoborate in organic solvents of propylene carbonate (PC) or acetonitrile (AN). Conductivity en-

hancers such as carbon black and graphite are added to improve electron transport within porous carbon electrodes. With a nominal specific capacitance of about 25 μF cm^{-2} for high surface area porous carbon [3], an overall capacitance of 500 F g^{-1} and an energy density of 500 J g^{-1} at 1 V operating potential are theoretically possible, but only about 20% or less of the theoretical value can be realised in commercial EDL capacitors. This is due to the polymer binder, usually 5-10 wt% polytetrafluoroethylene (PTFE), covering part of the carbon particle surface and lowering exposed area at the interface with the electrolyte; blocking the available surface by the compaction of the electrode, resistance between particles, etc. The carbon material used may also have impurities, and once charged the residual ash reacts with the electrolyte, again reducing practical performance. Electronic interface resistances at termination post, aluminium lid and can, internal aluminium-to-aluminium welds, current collector foils etc also reduce the power density of the device. Table 2.1 shows the capacitance and cell voltage of commercially available EDL capacitors.

Other than the organic electrolytes commonly used in commercial supercapacitors, much research has been done on room temperature ionic liquid (RTIL) electrolytes for EDL capacitors due to their large operating voltage window (2-4 V) and non-flammable and non-volatile properties. RTILs are molten salts composed of a mixture of anions and cations, common types include 1-ethyl-3-methylimidazolium dicyanamide [emim][$N(CN)_2$] and 1-ethyl-3-methylimidazolium tetrafluoroborate [emim][BF_4], but RTILs are very sensitive to temperatures as they have a tendency to crystallise below

Company name	Device name	Capacitance (F)	Cell/module voltage (V)	Type
Asahi Glass	EDLC	500-2000	3	Carbon/non-aqueous
AVX	Bestcap	0.022-0.56	3.5-12	Carbon/polymer/aqueous
Cap-XX	Supercapacitor	0.09-2.8	2.25-4.5	Carbon/non-aqueous
Cooper	PowerStor	0.47-50	2.3-5	Aerogel/non-aqueous
ELNA	Dynacap	0.333-100	2.5-6.3	Carbon/non-aqueous
Epcos	Ultracapacitor	5-5000	2.3-2.5	Carbon/non aqueous
Evans	Capattery	0.01-1.5	5.5, 11	Carbon/aqueous
Maxwell	Boostcap/PowerCache	1.8-2600	2.5	Carbon/non-aqueous
NEC	Supercapacitor	0.01-6.5	3.5-12	Carbon/aqueous; carbon/organic
Nippon Chemi-Con	DLCAP	300-3000	2.3, 2.5	Carbon/non-aqueous
Ness	NessCap	3-5000	2.3, 2.7	Carbon/organic
Matsushita/Panasonic	Gold capacitor	0.1-2500	2.3-5.5	Carbon/organic
Tavrima/ECOND	Supercapacitor	0.13-160	14-300	Carbon/aqueous

Table 2.1: A summary of the commercially available EDL capacitors [6]

the melting temperature and deteriorate the supercapacitor performance [7].

Aqueous electrolytes (ACl, A_2SO_4 and ANO_3, where A = H, Li, Na and K) offer higher ionic conductivities and minimise the need for extensive purification and handling under a controlled atmosphere such as a dry room or glove box, and simplify the fabrication and packaging process [8]. However, aqueous electrolytes have a narrow operate voltage ($\sim$ 1 V) due to electrolysis of water and evolution of hydrogen.

Solid-state electrolytes (described more fully later) provide the highest theoretical operating voltage window as no liquids are involved, but restricted ionic mobility undermines the power density and are comparatively under-explored. In summary, a fine balance among the ionic mobility, voltage window, safety and fabrication process needs to be considered for individual specifications.

2.1.2 Pseudo-capacitors

Pseudo-capacitance arises at the electrode surface where reversible battery-like faradaic redox reactions occur. There are three ways to obtain pseudo-capacitance: (a) by the charge required for deposition of adatoms; (b) by absorption or insertion into an intercalation host; and (c) by conversion of an oxidised species to a reduced species and *vice-versa* in a redox system [3]. An example of type (a) mechanism is H adsorption at a Pt electrode. Type (b) is most common in Li^+ intercalation in LiBs. Type (c) is most commonly used in pseudo-capacitors and has attracted significant research in

transition metal oxides because transition metals have more than one oxidation state and electrons are transferred between an oxidised species Ox and a reduced species Red according to Equation 2.3, where z is the number of electrons involved:

$$Ox + ze \rightleftharpoons Red \tag{2.3}$$

To compare the amount of stored charges in an electrode material of EDL capacitors, pseudo-capacitors and batteries, up to 0.17-0.20 electrons per atom of accessible surface between electrode and electrolyte are stored in EDL capacitors, 2.5 electrons per atom for the electroactive material in pseudo-capacitors, and 1 to 3 electrons per atom or molecule of the bulk phase in batteries [3]. Hence, supercapacitors have a low energy density where delocalised electrons can only be accumulated on the electrode surface, compared with faradaic charge transfer stored in the bulk of battery electrodes. Similarly, the number of electrons exchanged in a pseudo-capacitive process is much greater than the number of charges adsorbed electrostatically in an EDL capacitor with the same number of active ions; and introducing pseudo-capacitance can significantly improve the energy storage of electrode materials.

2.2 Electrode materials

2.2.1 Activated carbon

Various carbonaceous materials with high surface areas for charge adsorption can be used for EDL electrodes. Commercial supercapacitors use activated carbon (AC) powder mainly because of its ability to be engineered into a surface area of the order of 2000 $m^2\ g^{-1}$ [9], and with a controlled distribution of pores at comparatively low cost. AC can be produced from the pyrolysis of natural precursors (e.g coconut shell, phenolic resin or coal) in two steps: the carbonisation of the raw material and the activation of the carbonised product by oxidation in CO_2 or water vapour, with specific surface areas depending on activation time. A porous network in the bulk of the carbon particles is produced after activation (as shown in Fig. 2.3), with a broad pore size distribution consisting of micropores (<2 nm), mesopores (2-50 nm) and macropores (>50 nm) [classification according to IUPAC].

Considerable effort has been expended to increase the pore volume and surface area by refining the activation process [11], however some micro- and nanopores are too small to be accessible for aqueous or organic electrolytes [9]. Mesopores are required for the efficient transport of electrolyte ions to all parts of the electrode surface, especially the surface of particles in the electrode internal regions. At high discharge currents, the specific capacitance of mesoporous AC can be even higher than that of microporous AC [1], despite the lower overall area. Therefore, this shows that optimisation based



Figure 2.3: A schematic diagram of the inside porous structure of AC particles [10] © 2002 Elsevier.

on Equation 2.1 only is too simplistic - not only must the surface area S large, but also the distribution of pore diameters. A general rule is that the pores that have a sufficient size to adsorb nitrogen molecules at 77 K (0.5 nm [12]) are also available for the electro-adsorption of simple hydrated ions such as OH^- ions, since the size of a single nitrogen molecule is similar to that of hydrated OH^- [9]. For other electrolyte ions such as $BF_4{}^-$ in propylene carbonate with a size of 2 nm and $((C_2H_5)_4N^+)$ of 5 nm, micropores will not contribute strongly to the total double layer capacitance of the material [9].

Since the ionic conductivity inside the tortuous internal porosity of an electrode is likely to be different from that in the bulk electrolyte, the reduced mobility of ions inside the porous electrode structure determines the rate of electrochemical accessibility. However, ion mobility is not the only factor affecting kinetics and rate performance - electron mobility is also fundamental to performance since electrons must be transferred to/from the current collectors from all regions of the electrode for high performance.

The total electrode conductivity can be considered as a network of many resistors distributed throughout the mesoporous structure [9]. Electrical conductivity is therefore closely related to the morphology of the electrode; and usually the smaller the particle size, the poorer the conductivity because of the many carbon particle - carbon particle interfaces [9]. Therefore, conductivity enhancers such as carbon black are normally added into the commercial AC electrodes.

The ACs normally have pure EDL behaviour with a capacitance reaching 150-300 F g^{-1} in aqueous electrolytes and 100-120 F g^{-1} in organic electrolytes (because the latter have larger ions and slower ionic mobility), with energy densities > 5 Wh kg^{-1} and power densities of $\sim$10 kW kg^{-1} [11]. In summary, the charge storage performance of AC depends on the distribution of pore sizes, surface morphology and ionic and electronic conductivities.

2.2.2 Carbon nanotubes and their composites

Single-wall carbon nanotubes (SWNTs) have diameters of 0.9-1.7 nm and a surface area of $\sim$ 700 m^2 g^{-1} and multi-wall carbon nanotubes (MWNTs) have diameters of 10-50 nm and a surface area of 250-300 m^2 g^{-1} [13]. High temperature ($\sim$1200 ^{o}C [14]) preparation techniques such as arc discharge or laser ablation were first used to produce carbon nanotubes (CNTs) which involve high costs. Nowadays these methods have mostly been replaced by low temperature catalytic chemical vapour deposition

(CVD) (<800 ^{o}C), where decomposition of a carbon source (e.g acetylene) by a transition metal catalyst (e.g Fe) supported on a substrate (e.g mesoporous silica) takes place and the nanotube length, diameter, purity and density can be controlled by the parameters of CVD (e.g catalyst particle size), reaching industrial-scale synthesis [15].

CNTs have been considered for a range of applications including membrane supports for electrocatalytic reduction of oxygen and oxidation of hydrogen or methanol [16] [9], actuators [17], mechanical thin film applications [18], and a range of electrochemical energy conversion and storage devices [19]. For their application in supercapacitors, compared with currently used AC electrodes, the suggested benefits of CNT electrodes are their low resisitivity ($> 5\times10^{5}$ Sm^{-1} [20]), which offers enhanced electron transport required for high power applications, and a tendency to form interconnected mesoporous structures (as shown in Fig.2.4(a)) that facilitate ions to percolate throughout the electrode to form EDL efficiently, resulting in a high charge storage efficiency and a low electrolyte resistance [21].

As mentioned in Section 2.2.1, the pore size and surface area of AC-based electrodes can be tailored by variations in particle size and distribution, and activation process parameters [11]. However, for more immature CNT-based electrodes, analogous material approaches and processes with similar flexibility are not obvious, and therefore it remains unclear how the CNT meso-structure might be "designed" for performance or selected in advance by using a technique that can scale to realistic electrode areas, and

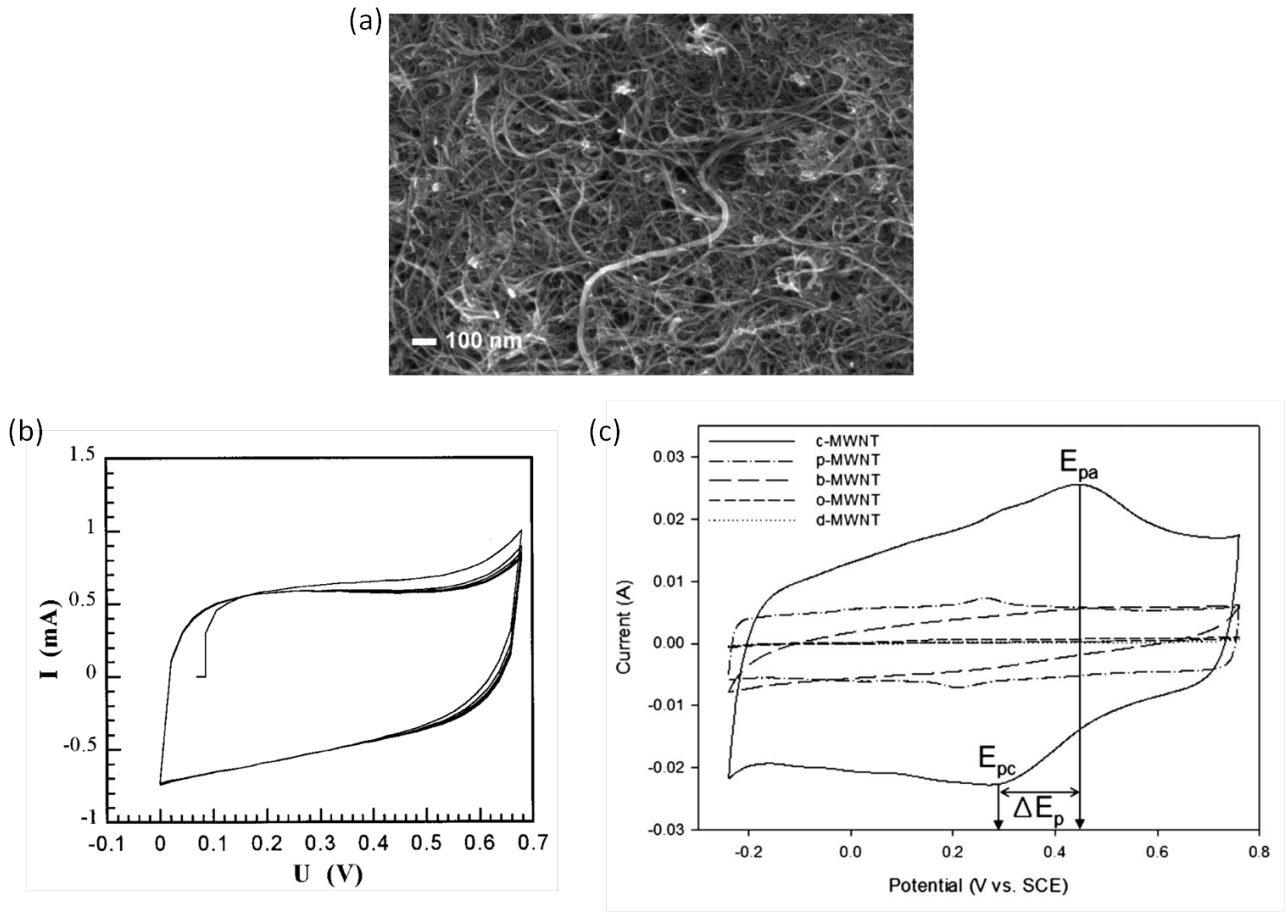


Figure 2.4: (a) Scanning electron micrograph (SEM) of the dip deposited MWNT network. Reprinted with permission from [22]. Copyright (2009) American Chemical Society; (b) cyclic voltammogram (CV) of a MWNT electrode in 6 M KOH at 1 mV s^{-1} [23] Copyright (2000) AIP Publishing LLC; and (c) CVs of various functionalised MWNTs in 1 M H_2SO_4 at 1 mV s^{-1}, where c-MWNT is carboxylic functionalised MWNT, p-MWNT is purified MWNT, b-MWNT is butyl functionalised MWNT, o-MWNT is octyl functionalised MWNT and d-MWNT is dodecyl functionalised MWNT [24] Copyright (2005) AIP Publishing LLC.

what ranges of meso-structures might be available. One solution is to use a layer-by-layer (LbL) approach in which, for example, MWNTs are functionalised with carboxylic COO^- or amine NH_3^+ groups, and then assembled together sequentially, layer-by-layer, by alternately dip coating in the oppositely charged MWNT suspensions [22]. The idea is that the MWNTs then form a less open, more compact meso-structure due to electrostatic attraction between the layers, that provides an improvement in volumetric or gravimetric performance of the electrode. An LbL film made this way improved mechanical integrity and consistency of thickness compared with pure MWNT films [22].

Covalent functionalisation of CNTs is not only used in controlling CNT structures such as producing highly packed electrodes, but more commonly used to improve the electrode capacitive behaviour through faradaic reactions, influencing wettability, and increasing electroactive surface area. Fig. 2.4(b) shows a regular, almost box-like cyclic voltammogram (CV) of a MWNT electrode in a 6 M KOH electrolyte, indicating pure EDL behaviour from which the specific capacitance was estimated to be $\sim$70 F g^{-1} at 1 mV s^{-1} [23]. Fig. 2.4(c) shows the CVs of various functionalised MWNTs in a 1 M H_2SO_4 electrolyte, in particular, the CV of carboxylic functionalised MWNTs (c-MWNT) had a pair of reversible peaks at around 0.45 V and 0.3 V and the specific capacitance of c-MWNT was enhanced to 120 F g^{-1} at 1 mV s^{-1} [9]. In this case, the reactions in Equations 2.4 to 2.6 show how the functional surface groups enhanced capacitance through faradaic characteristics [9]:

$$-C-OH \rightleftharpoons -C=O+H^{+}+e^{-} \tag{2.4}$$

$$-C=O+e^{-} \rightleftharpoons -C-O^{-} \tag{2.5}$$

$$-COOH \rightleftharpoons -COO^{-}+H^{+}+e^{-} \tag{2.6}$$

Other than carboxylic functionalisation, doping CNTs with nitrogen heteroatoms can enhance capacitance through the increase in electron donor capabilities [25]. In particular, substitution of C with N in the peripheral pyridinic groups played a useful role because of the strong electron donor characteristic of N heteroatoms, where the donor filled a conduction band by electrons, and in turn more ions were adsorbed [25]. The specific capacitance increased from 83 F g^{-1} to 126 F g^{-1} in a 1 M H_2SO_4 electrolyte with increasing N content from 7.4 wt% to 11.7 wt% [25].

There have been several attempts to fabricate 1D core-shell hybrid nanostructured electrodes to combine pseudo-capacitance from metal oxide tubes, and high electrical conductivity and mechanical stability from CNTs. For example, co-axial nanotubes of MnO_2 and CNTs were fabricated by vacuum infiltration of manganese nitrate solution into the channels of alumina template for MnO_2 and subsequent chemical vapour deposition to allow the CNTs to grow in the inner cores left by the MnO_2 shells [26]. Fig.

2.5 shows that the electrode was porous and the MnO_2 nanotube wall thickness was approximately 10 nm.

Another type of CNT-based 1D hybrid nanostructure is the heterojunction of CNTs with another material. Figs. 2.6(a) and (b) show an aligned multi-segmented CNT/AuNW hybrid electrode structure, where the CNT electrode was grown from the Au nanowire current collector ((c) and (d)) to reduce the electrode/current collector resistance and provided a high power density of 48 kW kg^{-1}, compared with ∼10 kW kg^{-1} for AC electrodes [27].

2.2.3 Metal oxides and their composites

Metal oxides can exhibit pseudo-capacitance because they have a range of oxidation states. Ruthenium oxide displays excellent electron and proton conduction and shows significant pseudo-capacitative behaviour in aqueous acid solutions over a 1.4 V range [28]. Faradaic reactions associated with a change in the ruthenium oxidation state in the potential region from 0.1 to 0.3 V in aqueous acid solutions are caused by the processes of intercalation and diffusion of protons, which are represented in the following manner, where $0<\delta<1$ [3]:

On the positive electrode:

$$HRuO_2 \rightleftharpoons H_{1-\delta}RuO_2 + \delta H^+ + \delta e \tag{2.7}$$

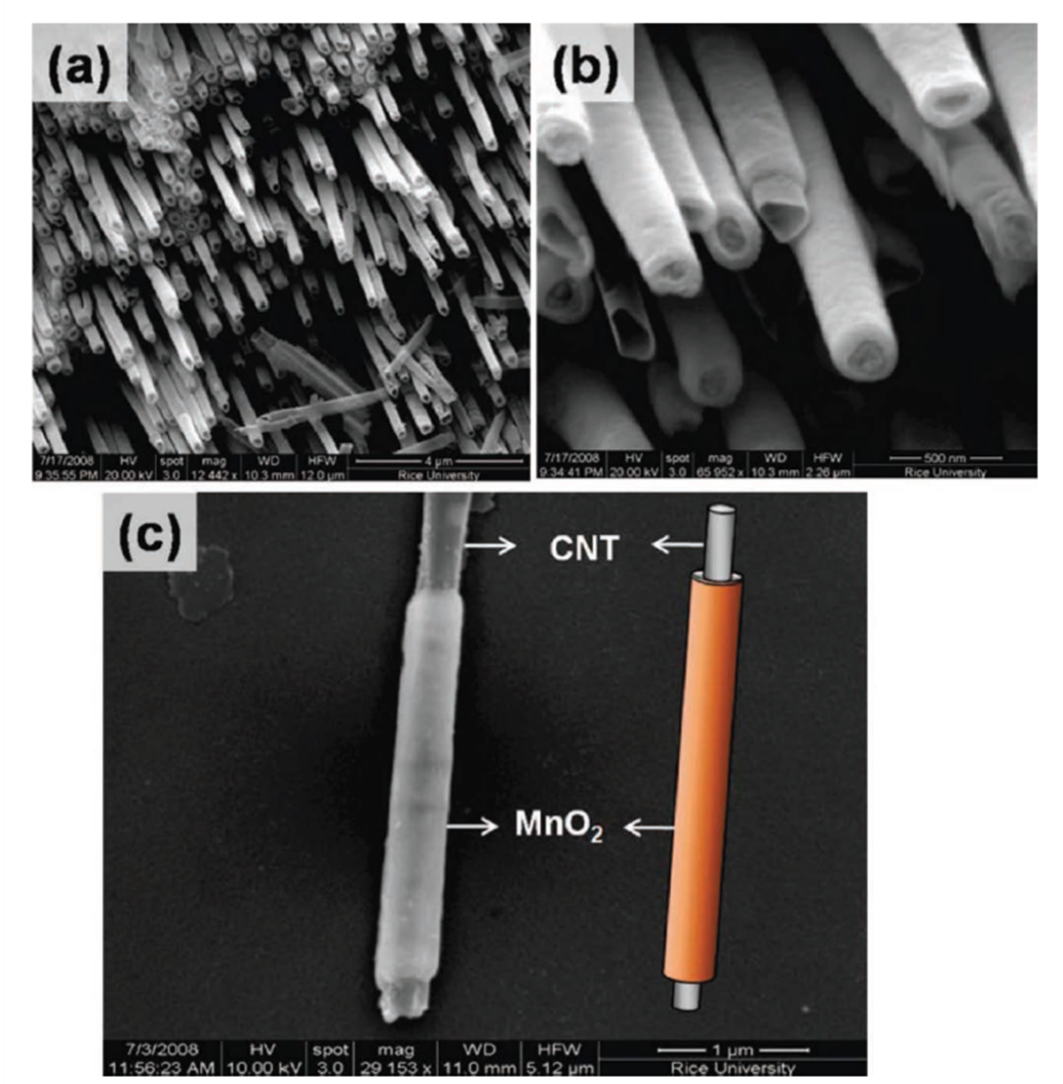


Figure 2.5: MnO_2/CNT hybrid co-axial nanotubes: (a) low and (b) high resolution SEM images showing the co-axial nature of the nanotube; and (c) SEM image and a schematic representation of a single co-axial nanotube [26] © 2012 John Wiley and Sons.

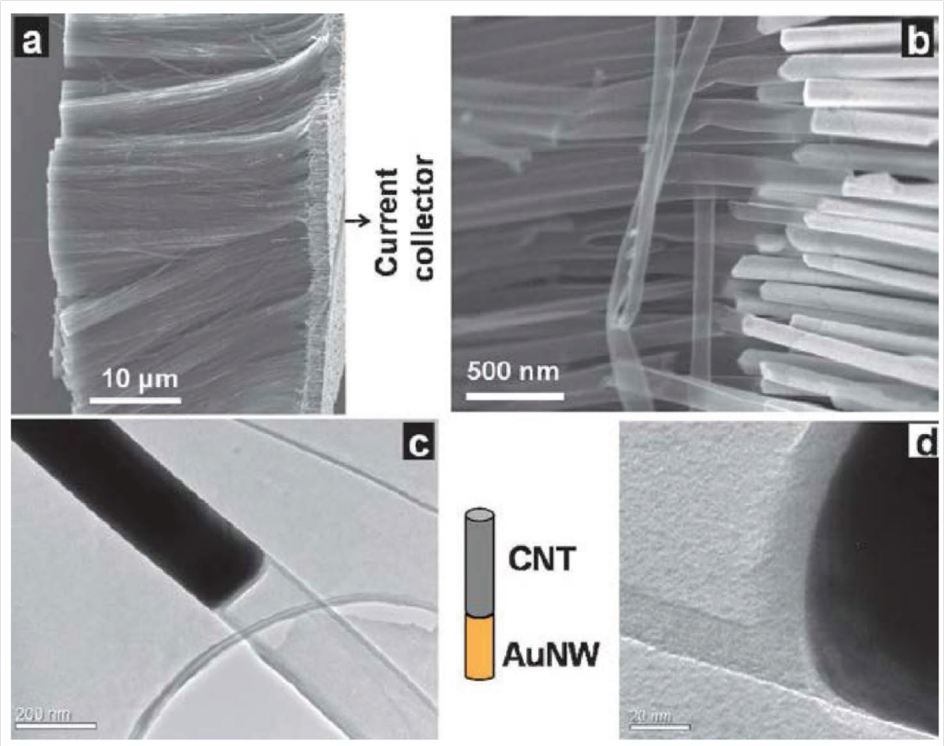


Figure 2.6: (a) SEM image showing aligned CNT/AuNW segments and the Cu back layer; (b) high resolution SEM image showing the interface between the CNT and AuNW segments; (c) TEM image showing the CNT/AuNW interface; and (d) high resolution TEM image showing the graphitic walls of CNT, approximately 15 nm thick. A schematic diagram of a single hybrid nanowire is shown [26] © 2012 John Wiley and Sons.

On the negative electrode:

$$HRuO_2 + \delta H^+ + \delta e \rightleftharpoons H_{1+\delta}RuO_2 \tag{2.8}$$

And the overall reaction:

$$HRuO_2 + HRuO_2 \rightleftharpoons H_{1-\delta}RuO_2 + H_{1+\delta}RuO_2 \tag{2.9}$$

Redox reactions can occur both on the surface and in the bulk in amorphous $RuO_2{\cdot}xH_2O$ phase [28], and the specific capacitance of $RuO_2 \cdot xH_2O$ (768 F g^{-1}) was much larger than that of crystalline RuO_2 films (380 F g^{-1}) [29]. A very high energy density of 8.3 Wh kg^{-1} and a power density of 30 kW kg^{-1} were achieved in a prototype 25 V capacitor where individual $RuO_2 \cdot xH_2O$ supercapacitors were stacked together in series [3]. However, amorphous $RuO_2 \cdot xH_2O$ may lead to depletion of the inner region of electrode where the semi-infinite array of ion cores are, which may put constraints on the maximum charge-discharge rate and stability [28].

Inevitably, the high cost of RuO_2 restricts its broad practical use, and other materials with similar properties but at lower costs have been sought. Manganese oxide MnO_2 has a lower cost and toxicity than RuO_2, and has oxidation states including Mn(II), Mn(III), Mn(IV), Mn(V), Mn(VI), and Mn(VII) [30], although it has a lower electron conductivity and no significant proton conductivity. A MnO_2 electrode in a NaCl elec-

trolyte exhibited a specific capacitance of 224 F g^{-1} at 10 mV s^{-1}, and 199 F g^{-1} at 50 mV s^{-1} [31]. NiO electrodes in a 1 M KOH electrolyte provided a specific capacitance of 278 F g^{-1} at 20 mV s^{-1}, but only within a narrow 0.5 V potential window due to its high reactivity [32] (compared with 1.4 V for RuO_2). One-dimensional magnetite (Fe_3O_4) nanowires can form a randomly oriented interpenetrating network for electrodes (Fig. 2.7) and had a capacitance of 106 F g^{-1} at 0.1 mA cm^{-2} in 0.1 M Na_2SO_3 between -1.2 and 0 V with a high energy density of 5.3 Wh kg^{-1}, compared with only 12 F g^{-1} at the same current density for more densely packed Fe_3O_4 nanoparticles because the nanowire electrode had sufficient mesoporosity facilitating ion transportation as well as providing a large area of microporosity for EDL formation [33]. The Fe_3O_4 nanowire aspect ratio was adjusted by varying the concentrations of NaOH and poly(ethylene glycol) (PEG) during synthesis [33], where PEG normally serves as a ligand to form chain-like complexes with transition metal cations such at Ti(IV), Sn(II), In(III) and Pb(II) upon heating and encourages the anisotropic nanowire growth [34].

TiO_2 is non-toxic and has favourable photoelectrochemical properties for dye-sensitised solar cells (DSSCs) [35]. Bare TiO_2 has a low EDL capacitance of 5-40 μF cm^{-2} and non-faradaic charge storage mechanism [36]. Treating TiO_2 to attach -OH groups can increase pseudo-capacitance and altering the TiO_2 lattice stoichiometry also increases capacitance. Two approaches for the latter have been used: one is by heat treatment [36], and the other is by cathodic reduction [37]. Heating TiO_2 aligned nanotubes in Ar at 630 ^oC for 2 hrs induced oxygen depletion of the structure, and increased capacitance

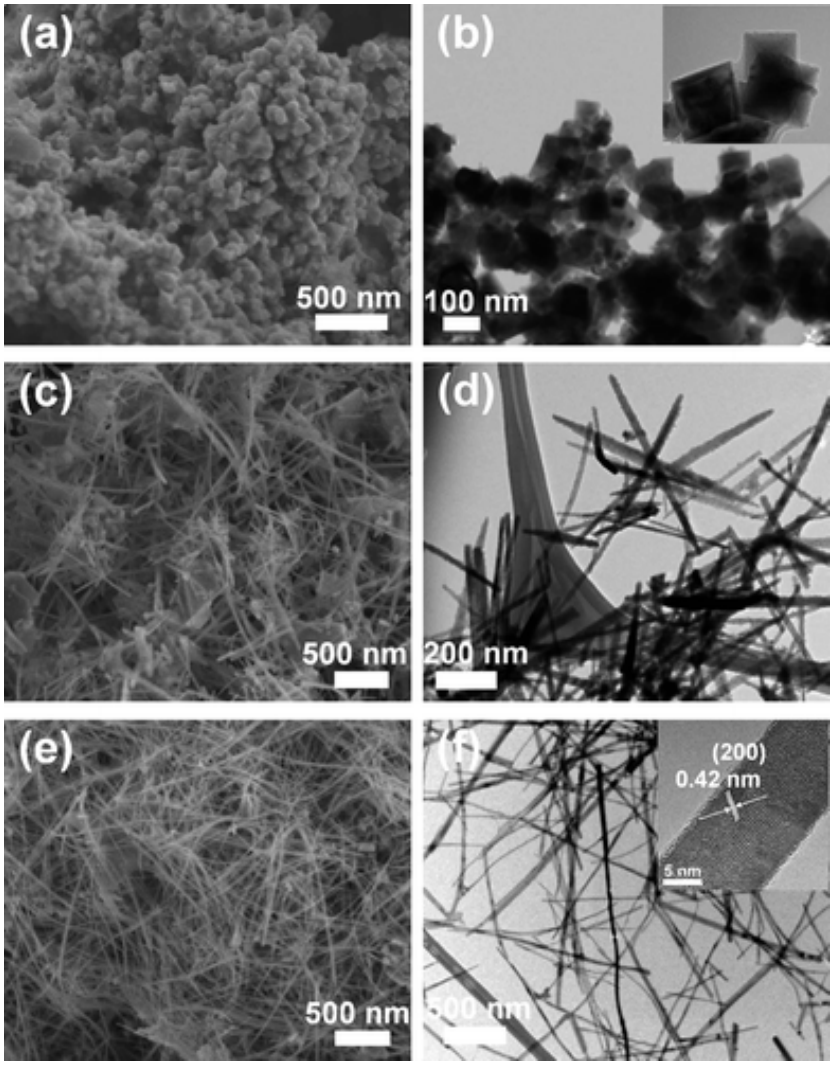


Figure 2.7: (a) SEM image of a spray deposited Fe_3O_4 nanoparticle film; (b) TEM image of the Fe_3O_4 nanoparticles; (c) SEM image of a spray deposited Fe_3O_4 nanorod film; (d) TEM image of the Fe_3O_4 nanorods; (e) SEM image of a spray deposited Fe_3O_4 nanowire film; and (f) TEM image of the Fe_3O_4 nanowires. The inset in (b) shows the octahedral Fe_3O_4 nanoparticles at higher magnification with diameter of *ca.* 100 nm. The inset in (f) shows a high resolution TEM image of a Fe_3O_4 nanowire [33] © 2010 Royal Society of Chemistry.

to 911 μF cm^{-2} at 1 mV s^{-1} in a 1 M KCl electrolyte [36]. Cathodic reduction of TiO_2 nanotubes at +4 V in 0.1 M Na_2SO_4 for 20 minutes increased capacitance by $\sim$20 times to 845 μF cm^{-2} at 10 μA cm^{-2} in a 0.5 M Na_2SO_4 electrolyte [37]. Areal instead of gravimetric units were sometimes used for "thin" film electrodes when the uncertainty in mass measurement was high. It is noted that the thin film itself almost always shows good behaviour because problems with ion mobility are not so evident in thin films, especially in half cells.

The majority metal oxide composite electrodes are fabricated by mixing a metal oxide powder with a carbon powder or CNTs to increase electrical conductivity, because metal oxides have more sluggish charging mechanism than EDL charging due to redox reactions. The specific capacitance of Co_3O_4 films was 165 F g^{-1} at 10 mV s^{-1} in 1.0 M KOH [38], and the composite of MWNTs and Co_3O_4 showed a specific capacitance of 201 F g^{-1} at 10 mV s^{-1} [39], which was also significantly greater than that of pure MWNTs ($\sim$70 F g^{-1} at 1 mV s^{-1} [23]). Here, the overall capacitance comprised EDL capacitance due to the MWNTs and pseudo-capacitance due to the Co_3O_4. These results on metal oxides indicate the importance of matching electrolytes to the specific oxide and electrochemical voltage window used.

Engineering the composite electrodes into designed nanostructures which can enlarge the electrode/electrolyte contact area per unit mass, provide more ion adsorption sites and charge-transfer reactions is a critical parameter for achieving a high capacitance

and high charge/discharge characteristics. Other than increasing the electrode conductivity, depositing metal oxides onto high surface area and 3D structured carbon may facilitate "wiring" of the metal oxide, in terms of ion transport. For example, permanganate (MnO_4^-) was used to react with acetylene black to form a layer of MnO_2 coating on the 3D carbon structure. Fig. 2.8 is a schematic diagram showing the deposition of metal oxide on a carbon structure, the diagram shows the difference between "self-limiting" and "poorly controlled" deposition, where the "self-limiting" deposition provided an almost homogeneous coating to maintain the complex pore structure [40]. The "self-limiting" deposition may be controlled by reaction conditions such as temperature and is the objective of many research investigations. The MnO_2-modified 3D carbon demonstrated an enhanced capacitance of 173 F g^{-1} at 5 mV s^{-1} compared with 105 F g^{-1} for the native carbon, but the capacitance decreased to 166 F g^{-1} with more MnO_2 loading as the mesopore channels were clogged [40], indicating further the importance of "self-limiting" deposition coating. Other than depositing onto porous carbon, MnO_2 was also deposited onto a CNT network on carbon fiber papers and exhibited an impressive 322 F g^{-1} capacitance at 1 mV s^{-1} in 0.65 M K_2SO_4 [41].

2.2.4 Polymers and their composites

Electrochemically active polymers such as polyaniline (PANI) and polypyrrole are another category of materials offering pseudo-capacitance for supercapacitor electrodes. They have a large degree of π-orbital conjugation that gives rise to electronic conduc-

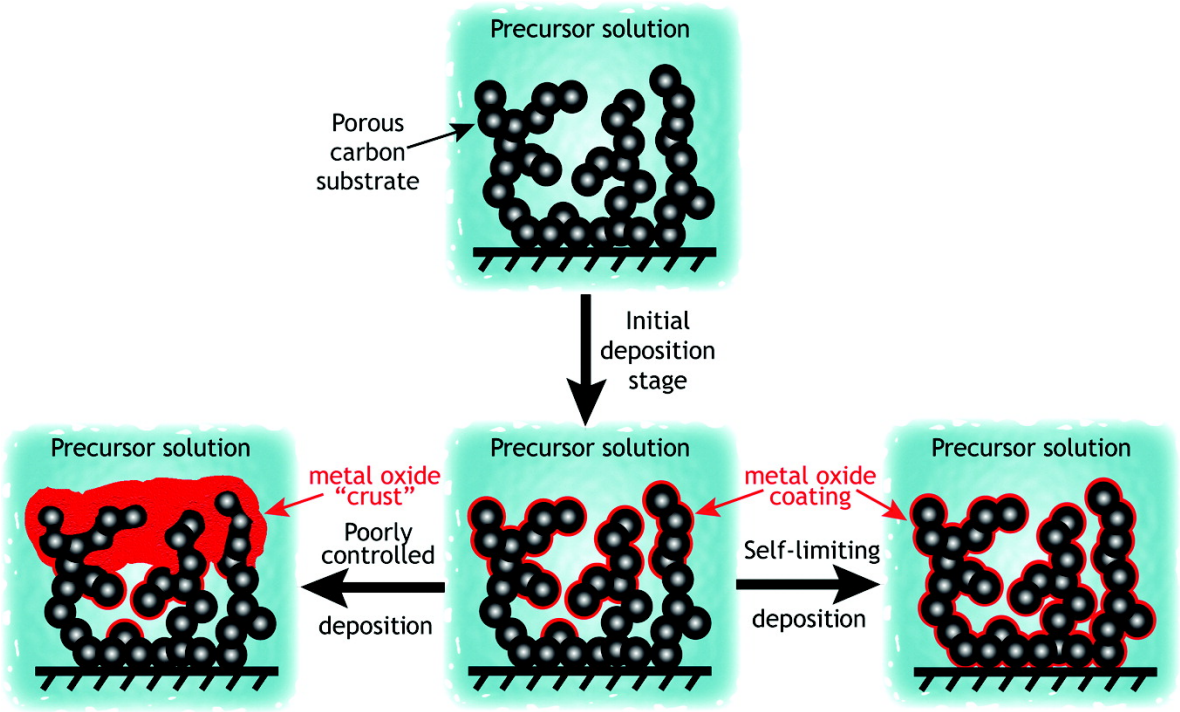


Figure 2.8: A schematic diagram of redox deposition under "poorly controlled" (left) versus "self-limiting" (right) conditions. Reprinted with permission from [40]. Copyright (2013) American Chemical Society.

tivity and the capability of being oxidised or reduced by withdrawal or injection of electrons [3]. When electrons are extracted from the polymer backbone to the external circuit, the polymer becomes positively charged, or "p-doped", and attracts anions from the electrolyte into the polymer film to counter-balance the positive charge; and *vice-versa* for n-doped polymers [42]. Most of these polymers are synthesised by oxidation of relevant monomer in solution, and the as-formed polymers tend to be in the oxidised or "p-doped" state and have a comparatively high electronic conductivity in the range of 1-100 S cm^{-1} [42]. Such polymer materials can be much cheaper than metal oxides and can generate comparably large specific capacitances because they have a continuous range of oxidation states with increasing electrode potential, and the voltage range can be extended to higher than 3 V by employing n- and p-dopable polymers in non-aqueous electrolytes [42].

However, being organic chemicals in nature and subject to periodic oxidations and reductions, these polymers do not have a very long-term stability or cycle life ($< 10^4$). Eventually, there would be an exhaustive state because valence-band electron transfer occurs with a phase change, and this may change the conductive structure of polymers; and the polymer fibres may start to grow into each other after a number of cycles, limiting ionic diffusion [43]. Coating pyrrole onto the surface of metal oxide, such as Fe_3O_4 nanowires gave a higher overall specific capacitance (190 F g^{-1}) than Fe_3O_4 nanowires alone (106 F g^{-1}) and a high durability (the specific capacitance was retained above 160 F g^{-1} after 500 cycles) [33]. Here, a thin layer of polypyrrole contributed both EDL

and pseudo-capacitance to the overall capacitance, and the polypyrrole had a higher stability when supported by a more stable Fe_3O_4 nanowire interconnected structure. Polypyrrole/graphite composite electrodes have been fabricated so that the graphite network provided an electronically conductive skeletal current-collector for the electroactive polymer, where porosity and contact surface area of the composite electrodes were both comparatively high, and ionic diffusion was fast for the polymer oxidation and reduction [44]. A specific capacitance of 440 F g^{-1} at 10 mV s^{-1} was obtained for the polypyrrole/graphite composite electrode in a KCl electrolyte after 5 polymerisation cycles [44]. Unfortunately, due to the high chemical-activity of pyrrole, the oxidative polymerisation of pyrrole on the surface of the graphite had to be performed in a glove box flushed with nitrogen gas [44], which restrictd its potential use in mass production. PANI-graphene nanocomposites have also been investigated as an electrode material, with the graphene flakes embedded in the PANI network [45]. A prototype supercapacitor was fabricated using PANI-graphene films on graphite electrodes and a 2 M H_2SO_4 electrolyte, providing specific capacitances of 300-500 F g^{-1} at a current density of 0.1 A g^{-1} [45].

2.3 Cell configuration

2.3.1 Symmetric cells

The conventional configuration of a supercapacitor is an ion-permeable, electrically insulating separator sandwiched between two identical very high surface area electrodes (usually based on AC) flooded with a liquid electrolyte and sealed in a package that is required to retain the electrolyte (preventing leakage and possible combustion) and to provide mechanical integrity. Commercial supercapacitors are usually either in a jelly-roll form, where a pair of double-side coated electrodes, porous paper separator and aluminium foil current collector are wound to form a cylindrical complex, as shown in Fig. 2.9(a) and (b), or in a flat form, such as a small button cell in Fig. 2.9(c).

Since a full cell is essentially two electrostatic capacitors connected together in series, the overall capacitance is always lower than either of the electrode capacitance, and can be calculated from Equation 2.10:

$$C_{tot} = \frac{C_1 \cdot m_1 \cdot C_2 \cdot m_2}{C_1 \cdot m_1 + C_2 \cdot m_2} \tag{2.10}$$

where C_{tot} is the overall capacitance of two electrode full cell, C_x is the specific capacitance of an individual electrode, and m_x is the mass of an individual electrode.

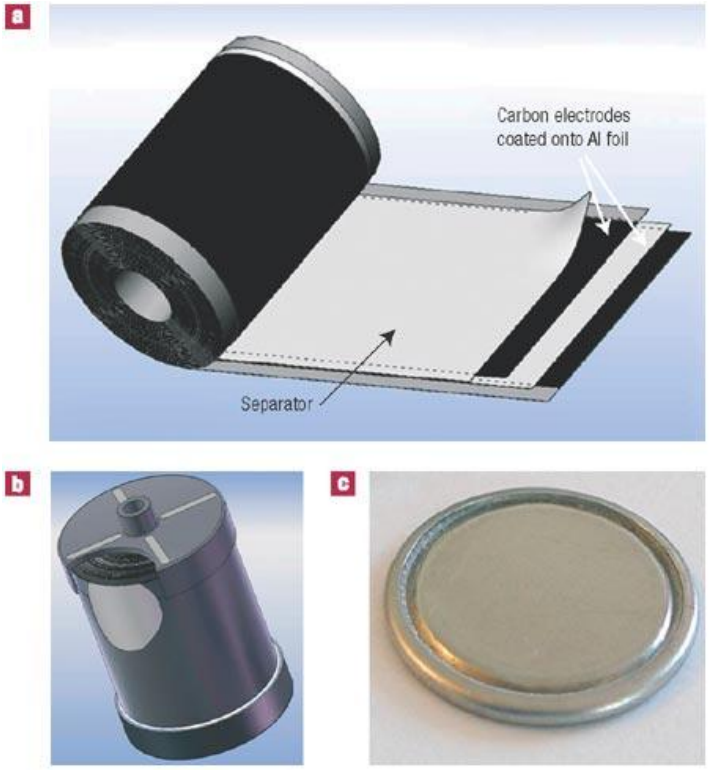


Figure 2.9: (a) A schematic diagram of a commercial spirally wound supercapacitor; (b) an assembled device weighing 500 g and rated for 2600 F; and (c) a small button cell of 1.6 mm in height that stores 5 F. Both (b) and (c) operate at 2.7 V [11] © 2008 Nature Publishing Group.

2.3.2 Asymmetric cells

The specific energy can be enhanced further by asymmetric configurations where a pseudo-capacitive material such as MnO_2 is used for the positive electrode, and high surface-area carbon is used for the negative electrode. This asymmetric design increases charge storage by redox reactions at the positive electrode, while maintaining fast charge-discharge response by EDL mechanism at the negative electrode [8].

One of the main advantages of asymmetric cells is an increase in the overall operating voltage range compared with that of symmetric cells, because the pseudo-capacitive material in the positive electrode and the carbonaceous material in the negative electrode can extend the effective electrochemical stability window (ESW) beyond the thermodynamic limit of 1.2 V in aqueous electrolytes, as illustrated in Fig. 2.10. The increase in the voltage window increases energy density and the asymmetric supercapacitor with MnO_2 and carbon electrodes (MnO_2//carbon) has demonstrated promising specific energies ranging from 10 to 28 Wh kg^{-1} at an ESW of 2 V [46]. Asymmetric NiOOH//carbon (8 - 10 Wh kg^{-1}) and PbO_2//carbon (25 Wh kg^{-1}) supercapacitors have already been commercialised by Nesscap for applications in uninterruptable power supplies and grid scale storage respectively.

2.3.3 Solid-state cells

The majority of current supercapacitors use liquid electrolytes and the risk of electrolyte leakage is one of the key concerns particularly for wearable and implantable applications. The need to package and contain the liquid electrolytes also severely restricts the development of thin, lightweight and flexible supercapacitors. Solid-state supercapacitors are attracting attention in recent years, where a solid-state electrolyte is used, which normally also acts as an electrically insulating separator. However, limited number of mobile ions and low ionic conductivity typically observed in the solid state restrict high power performance, which is the main advantage of supercapacitors. Most current studies try to improve ionic conductivity by hot pressing the electrodes onto an electrolyte gel to promote infiltration and to form a thin supercapacitor of 80-350 μm, but it is hard to regulate and difficult to avoid electrical shorts across the cell. The stability and performance of the solid-state supercapacitors to environmental conditions over time also need further research.

CNTs, graphene, graphite or their composites with metal oxides have been used as film electrode materials for the solid-state supercapacitors [47, 48, 49], and these materials are similar to the ones mentioned in the previous sections. Another main component of the solid-state supercapacitor is its electrolyte, which needs to have a high ionic conductivity, prevent short circuits across the cell and provide mechanical stability and flexibility.

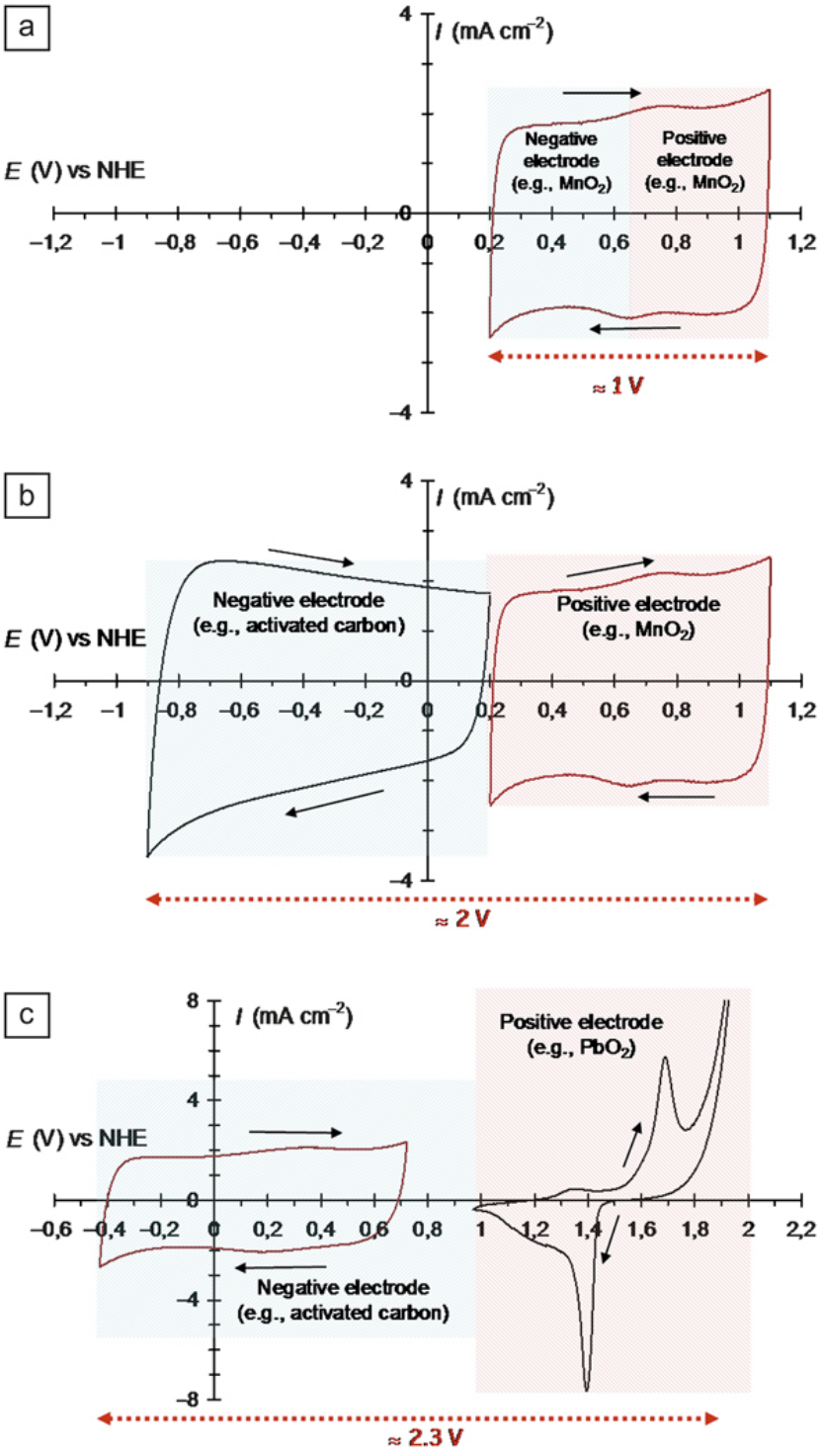


Figure 2.10: Schematic representation of CVs for three different configurations of aqueous-based supercapacitors in which areas shaded in red and blue represent the potential window of the positive and negative electrodes, respectively for: (a) symmetric $MnO_2//MnO_2$ in 0.5 M K_2SO_4; (b) asymmetric $MnO_2//AC$ in 0.5 M K_2SO_4; and (c) asymmetric $PbO_2//AC$ in 1 M H_2SO_4 [8] © 2011 Cambridge University Press.

Many solid-state cells in the research literature replace the ion conducting polymeric gel with a proton conducting Nafion membrane, produced by Du Pont, which is a functionalised polymer bearing negatively charged perfluorosulfonate (-SO_2F-) groups in the main structure, promoting proton hopping through -SO_3-H^+- groups [50] [51]. This membrane is suitable for use with H^+ containing electrolytes; it can also be treated by soaking to provide Na^+ and K^+ mobility for alternative electrolytes. A solid-state supercapacitor was fabricated by hot pressing two AC electrodes onto a Nafion (160 μm) membrane and achieved a capacitance of 130 F g^{-1} at 10 mV s^{-1}, which was comparable with the equivalent liquid electrolyte supercapacitor although the conductivity of Nafion membrane was 6 x 10^{-2} S cm^{-1} compared with 2 x 10^{-1} S cm^{-1} for a 1 M H_2SO_4 electrolyte [52]. Another solid-state supercapacitor was fabricated comprising functionalised reduced graphene oxide electrodes (5 μm) and a solvent-cast Nafion membrane (20 μm), where the film electrodes were made by vacuum filtering and a viscous Nafion solution was slowly poured onto the electrode followed by annealing and hot pressing [53]. This solid-state supercapacitor achieved 119 F g^{-1} at 1 A g^{-1}, but the cell required re-immersion in 1 M H_2SO_4 prior to testing.

Returning to gel electrolytes, one of the most-researched solid-state gel electrolytes comprises a basic polymer such as polyvinyl alcohol (PVA) mixed with a strong acid such as H_2SO_4 or H_3PO_4. The acid protonates the polymer and proton conductivity occurs along the ${SO_4}^{2-}/{HSO_4}^-$ or ${HPO_4}^{2-}/{H_2PO_4}^-$ anionic hydrogen-bonded chains

[54]. The Lewis acid-base interaction between the PVA polymer with the acid molecules determines the attractive energy and together solubility, wettability, adsorption and crystallinity of the gel electrolytes [55]. This type of polymer complex is normally prepared by a solution cast technique, followed by hot pressing to make a solid-state supercapacitor. The polymer complexes exhibit a relatively high proton conductivity both in dehydrated and hydrated states (for example at 30 ^{o}C the protonic conductivity of PVA-H_3PO_4 complex was 10^{-3} S cm^{-1} [56]), but their mechanical and chemical stability is relatively poor. A solid-state supercapacitor with PANI/CNT electrodes (22-37 μm) and a H_2SO_4-PVA gel electrolyte (30-45 μm) achieved a capacitance of 332 F g^{-1} at 1 A g^{-1}, but with a low power density of 2.1 kW kg^{-1} [47]. A solid-state supercapacitor with carboxylic functionalised SWNTs on cotton paper as electrodes and a H_3PO_4-PVA gel electrolyte provided 116 F g^{-1} at 2 mV s^{-1} [49]. A capacitance of 477 F g^{-1} at 0.4 μA mm^{-2} was reported for a solid-state supercapacitor with PANI/SWNT/TiO_2 nanocomposite on highly oriented pyrolytic graphite (HOPG) electrodes and a H_3PO_4-PVA electrolyte [57]. A solid-state supercapacitor with TiO_2 nanowires with a thin carbon shell grown on carbon fabrics and a H_2SO_4-PVA gel electrolyte exhibited a volumetric capacitance of 0.125 F cm^{-3} for the entire device at a current density of 0.1 mA cm^{-2}, and a maximum energy and power densities of 0.011 mW h cm^{-3} and 0.019 W cm^{-3} [58].

PVA can also be mixed with a heteropoly acid, either $H_4SiW_{12}O_{40}$ (SiWA) or $H_3PSiW_{12}O_{40}$ or a mixture of (SiWA)-H_3PO_4 to form polymer electrolytes, retaining a Keggin struc-

ture with crystallised protonated water in the form of $H_5O_2^+$ and which was more mechanically stable but less flexible than the gel electrolyte [59]. The polymer electrolyte (45-50 μm) was made by casting and followed by hot pressing, and the heteropoly acid-base electrolyte had a conductivity of $\sim$1.3 x 10^{-2} S cm^{-1}, while the solid-state supercapacitor with graphite electrodes and SiWA-H_3PO_4-PVA electrolyte had a capacitance of 0.7 mF cm^{-2} even at a very fast scan rate of 20 V s^{-1} [60].

Aromatic polymers such as poly(4-phenoxybenzoyl-1,4-phenylene) (PPBP) and poly(oxy-1,4-phenyleneoxy-1,4-phenylenecarbonyl-1,4-pheneylene) (PEEK) have been used as proton-conducting gel electrolytes. Both need to be sulfonated by concentrated acid such as H_2SO_4 first to attach SO_3H groups to the aromatic rings. The sulfonation can be controlled by reaction conditions to prevent polymer degradation or crosslinking. The proton conductivity of sulfonated PPBP (S-PPBP) was 10^{-2} S cm^{-1} and 10^{-5} S cm^{-1} for PEEK (S-PEEK) both with 65 mol% sulfonation because the S-PPBP normally has a tendency to include higher amounts of bound water resulting in a higher conductivity at high temperatures and low humidities [54]. The solid-state supercapacitor with a S-PEEK electrolyte and PANI/carbon powder/S-PEEK electrodes had a capacitance of 480 F g^{-1} where the mass only referred to the mass of PANI and the preparation of S-PEEK membrane was complicated with multiple mixing, drying, degassing and curing [38].

2.4 Processing

2.4.1 Manufacture of commercial supercapacitors

As mentioned in Section 2.2.1, current commercial supercapacitors use AC electrodes, produced by doctor blading. The carbon powder is generally pre-treated to remove moisture and most of the surface functional groups to improve stability during cycling, since both can be responsible for capacitance fading [11]. Fig. 2.11 is a schematic diagram of doctor blade processing of the AC slurries with polymer binders (usually 5 wt% poly(tetrafluoroethylene) (PTFE)) and conductivity enhancers (usually carbon black), and such fabrication can only produce relatively 40-200 μm thick electrodes. The electrodes are generally rolled (calendered) to increase density but the final electrode porosity between the powders and additives may be too tortuous for electrolyte ions to penetrate efficiently under all conditions of interest [4]. Normally only 25 - 30 F g^{-1} per cell mass has been reached [61] and the low capacitance is due to the relatively thick electrodes produced by doctor blading, which (as in batteries) is believed to be due to a large proportion of inactive material in the cell, especially far from the separator. The polymer binder used and the resistance between the electrodes and current collectors also affects the overall capacitance.

There is a technological interest in a thinner ($\leq$10 μm) and more compact structure for higher specific capacitances and power densities because the ionic diffusion channels are shorter and the active material per volume contributing to charge storage is higher.

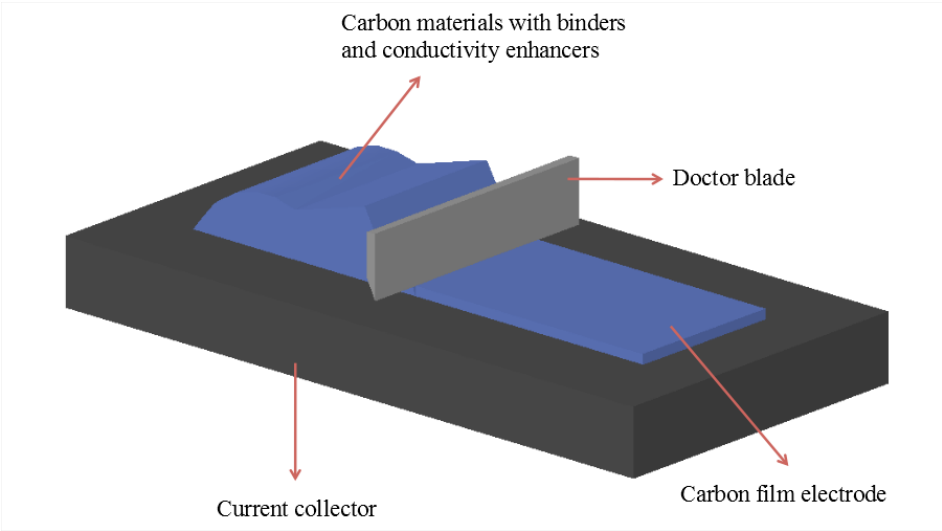


Figure 2.11: A schematic diagram of doctor blade processing by which 40-200 μm thick carbon films are produced.

Doctor blading does not allow a control over the morphology, porosity and structure of the electrode films, which are the major factors determining ionic and electronic transports of the electrode. Current manufacture is however scaleable, robust and relatively cheap. In the following sections, alternative methods of manufacture are reviewed, with a focus on those suited to exploit newer nanostructured electrodes based on materials such as CNTs.

2.4.2 Vacuum filtration

Vacuum filtration has been commonly used to fabricate free-standing thin films of buckypaper consisting CNTs and/or nanofibres (CNFs) without binders. A mixture of CNTs and CNFs is dispersed in deionised water by adding surfactants such as Triton-X (Dow) [62]. The suspension is then filtered under vacuum through a nylon membrane and the

sediment then washed thoroughly with alcohol to remove any residual surfactant. After drying, a film layer is peeled from the filter membrane to produce a free-standing buckypaper. The buckypapers produced by this method have an average thickness of 35 μm, a surface area of $\sim$ 40 m^2 g^{-1} and a porosity of 85% [62].

Figure 2.12 shows SEM micrographs of the surface morphology of buckypapers produced by vacuum filtration, using a mixture of SWNTs and CNFs with a weight ratio of 1:3 and 1:5. Vacuum filtration is more suitable for making a matrix of nanofibres of 100-200 nm in diameter and 30-100 μm long and may be less suitable for the smaller SWNTs of 0.8-1.2 nm in diameter and 100-1000 nm long. Controlling the morphology, uniformity and thickness of the film can be difficult and the film area is restricted to the filter membrane size.

2.4.3 Electrophoretic deposition

Electrophoretic deposition (EPD) is widely used in industry for the deposition of, for example, phosphor for displays [63]. Fig. 2.13 is a schematic diagram of using EPD to deposit CNTs into 1-7 μm thick films, where a stainless steel substrate and a counter electrode are immersed into a CNT suspension in methanol and a DC voltage of 2.7 V is applied between the two electrodes [63]. The CNT bundles migrate towards the positive electrode upon application of the voltage and the deposition rate is controlled by the CNT concentration and the DC current. EPD generally produces films with

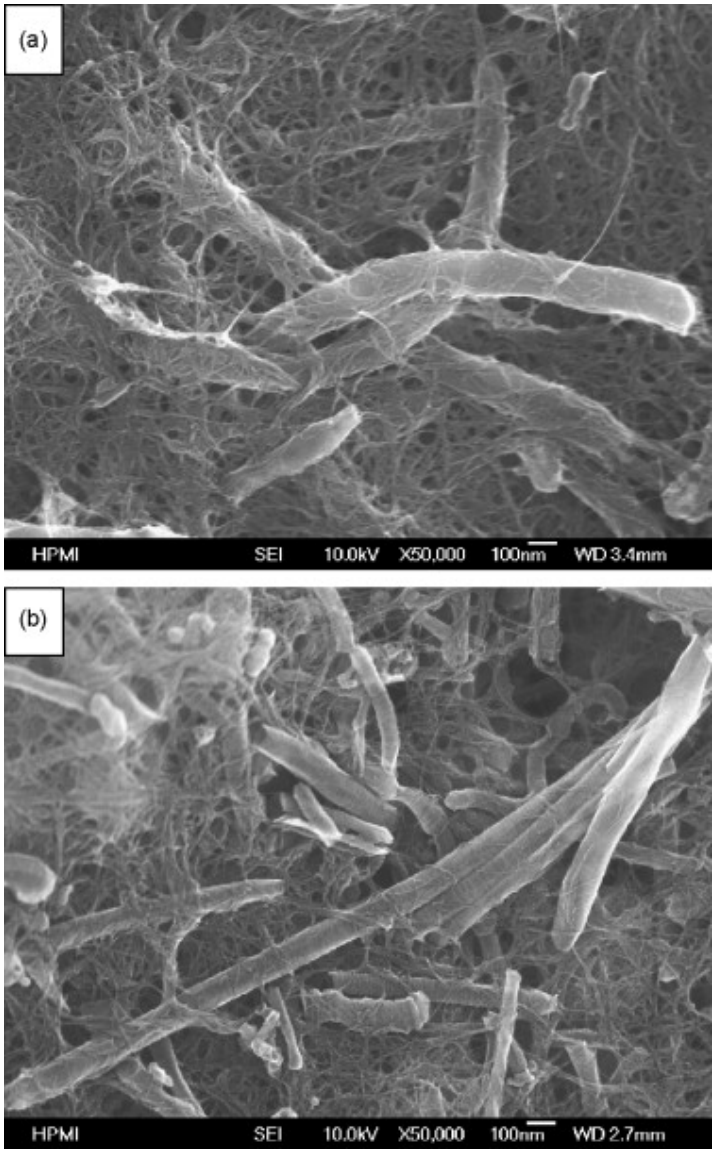


Figure 2.12: Surface morphology of the buckypaper of a mixture of SWNTs and CNFs with a weight ratio of (a) 1:3; and (b) 1:5 [62] © 2010 Elsevier.

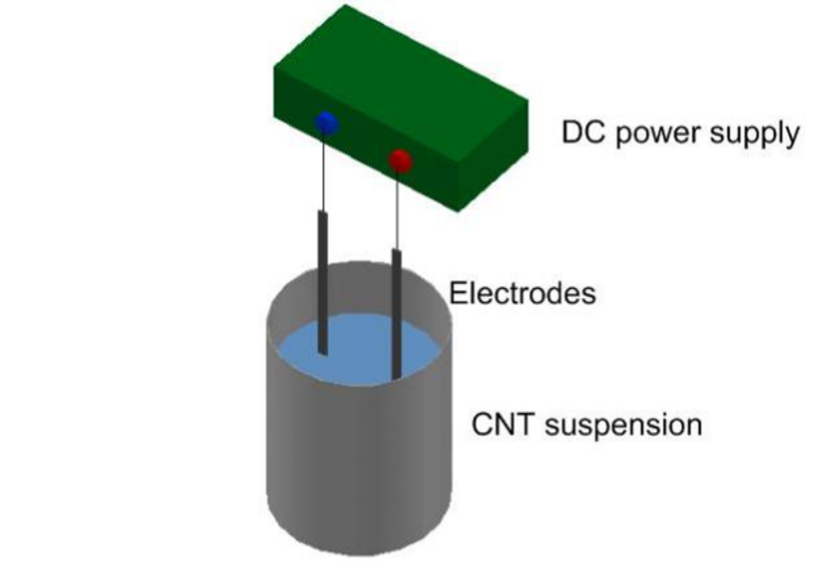


Figure 2.13: A schematic diagram of simple electrophoretic deposition processing.

a relatively good homogeneity and packing density, with good adhesion between the film and its substrate. However, controlling the nanostructure morphology is difficult to achieve by this processing technique.

2.4.4 Electrospinning

Electrospinning stretches a viscous charged fluid in an electric field and enables control over the resulting fibre diameter by a force balance between surface tension and electrostatic charge repulsion [64]. This method is most widely used in producing fibres from solutions of different polymers to make a film of polymer composite or in the field of biological and tissue engineering to make functionalised high surface-area films with proteins [65].

Fig. 2.14 shows that electrospinning is used to spray nylon 6,6 fibres, where the reser-

voir of polymer fluid is contacted with a large electric potential of 10's of kV and delivers to the tip of a small capillary at a slow flow rate of typically 0.1 ml min^{-1} [64]. The electrical charge that develops at the fluid free surface interacts with the external electrical field, resulting in the emission of a steady fluid jet that is thinned down as it accelerates downfield to produce fibres of $\sim$1 μm diameter and 20-30 μm length [64]. Producing an 8-10 inch diameter nylon 6,6 fibre membrane of 0.5 mm thick takes $\sim$40 minutes, and the surface area of the membrane is $\sim$ 37 m^2 g^{-1} [66].

An advance to this electrospinning was to fabricate nanocomposite mats such as poly (dimethyldiallylammonium chloride) (PDAC) with TiO_2 nanoparticles, where the emitted fibres bridged together to form an interconnected matrix so that multiple fibre coating matrix combinations with different morphologies and functions for membranes can be developed. However, in most operations of interest, the jet can experience instability, leading to bending and stretching of the fibres because these elastic effects in the jet are difficult to control [64].

2.4.5 Electrostatic spray deposition

A similar processing to electrospinning also under a high DC voltage is electrostatic spray deposition (ESD), which has been used to fabricate carbon-based thin film electrodes for supercapacitors [67] and other materials such as metal oxides (lithium manganese oxide and lithium cobalt oxide) for cathodes in lithium ion batteries [68] [69].

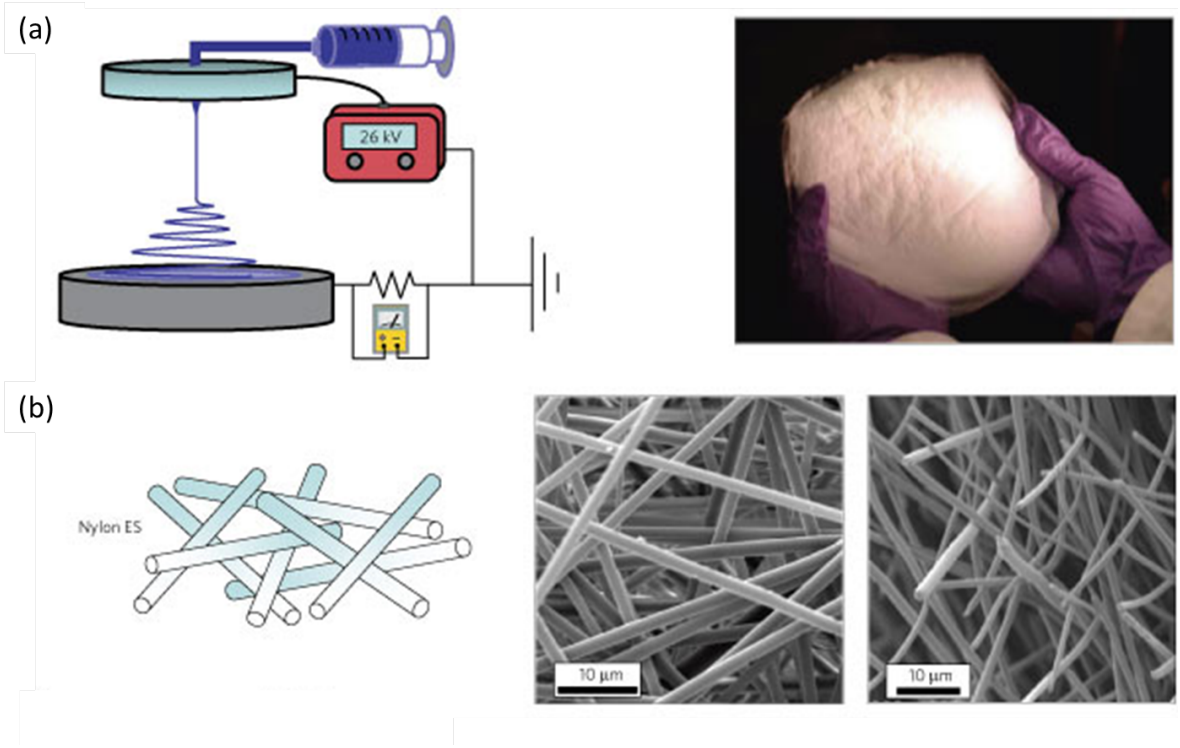


Figure 2.14: (a) Electrospinning technique (left) is used to make nylon 6,6 fibre mats of 200-250 mm diameter (right); and (b) a schematic representation and top-down (centre column) and cross-sectional (right) SEMs of the fabricated nylon 6,6 fibre mat [66] © 2009 Nature Publishing Group.

Fig. 2.15 is a schematic diagram of this processing configuration. ESD atomises a precursor solution usually dissolved in an alcohol at the needle of a syringe into an aerosol under the application of a high DC potential difference (6-22 kV) between the needle tip and a substrate, resulting in a well-defined trajectory of spray droplets being directed towards the heated substrate along the electric field [70]. The resulting film thickness is normally in the range between 1 to 40 μm, depending on the duration of spray [67]. The main advantage of ESD is good adhesion between the sprayed film and substrate due to a large potential applied between the nozzle and the substrate, so that the substrate does not need to be pre-treated. However, the slow flow rate at which the precursor solution is pumped (1-10 ml h^{-1} [67]) restricts the fabrication speed and a large potential difference is always required which limits the practical application of this processing technique.

2.4.6 Atomisation spray deposition

A faster and more flexible spray processing without the need for an electrostatic field is the atomisation spray deposition that has been developed at Oxford University [13, 71, 72, 73] and is used in this thesis. A suspension (normally aqueous-based) is prepared by sonication and then atomised continuously from a nozzle at high velocity by a compressed air stream to deposit the resulting droplets onto a substrate placed on a heating plate moving in a pre-programmed zig-zag pattern underneath the spray heads. The fine droplets are dried immediately so there is no excessive build-up of any liquids, producing a homogeneous distribution of entangled network of nanomaterials

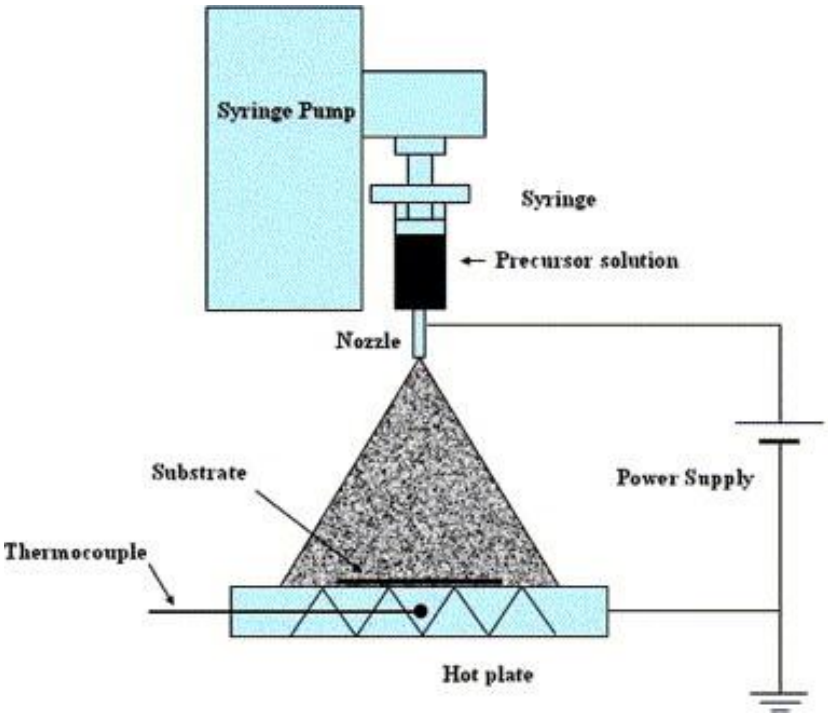


Figure 2.15: A schematic diagram of electrostatic spray deposition system [67] © 2006 Elsevier.

such as CNTs with a pre-determined thickness from a few hundred nanometres to many microns, depending upon the deposition time.

The structure of the sprayed films can be modified by for example, layer-by-layer (LbL) sequentially spraying oppositely charged functionalised SWNTs by two nozzles, which will be discussed in Chapter 4 in this thesis. Solid-state supercapacitors can also be fabricated by this reliable and straightforward processing, demonstrating the flexibility of this technique. The detailed methodology and results will be discussed in Chapters 5 and 6.

This ambient condition, low cost and automated spray approach has the advantages of scalability, control over the film thickness, manipulation of the film structure and morphology, and decreases the total process time by 25 to 100 fold [74].

Bibliography

[1] V. V. N. Obreja, "On the performance of supercapacitors with electrodes based on carbon nanotubes and carbon activated material - a review," *Physica E-Low-Dimensional Systems & Nanostructures*, vol. 40, no. 7, pp. 2596–2605, 2008.

[2] J. P. B. S. Amokrane, *Modern Aspects of Electrochemistry*. Plenum, 1992.

[3] B. E. Conway, *Electrochemical Supercapacitors, Scientific Fundamentals and Technological Applications*. Kluwer Academic / Plenum Publishers, 1999.

[4] F. Beguin and E. Frackowiak, eds., *Supercapacitors - Materials, Systems, and Applications*. Wiley-VCH, 2013.

[5] L. L. Zhang and X. S. Zhao, "Carbon-based materials as supercapacitor electrodes," *Chemical Society Reviews*, vol. 38, pp. 2520–2531, 2009.

[6] A. Pandolfo, "Carbon properties and their role in supercapacitors," *Journal of Power Sources*, vol. 157, pp. 11–27, 2006.

[7] S. I. Fletcher, F. B. Sillars, N. E. Hudson, and P. J. Hall, "Physical properties of selected ionic liquids for use as electrolytes and other industrial applications," *Journal of Chemical & Engineering Data*, vol. 55 (2), pp. 778–782, 2010.

[8] J. W. Long, D. Belanger, T. Brousse, W. Sugimoto, M. B. Sassin, and O. Crosnier, "Asymmetric electrochemical capacitors - stretching the limits of aqueous electrolytes," *Materials Research Society*, vol. 36, pp. 513–522, 2011.

[9] E. Frackowiak and F. Beguin, "Carbon materials for the electrochemical storage of energy in capacitors," *Carbon*, vol. 39, no. 6, pp. 937–950, 2001.

[10] C. Hsieh and H. Teng, "Influence of oxygen treatment on electric double-layer capacitance of activated carbon fabrics," *Carbon*, vol. 40, pp. 667–674, 2002.

[11] P. Simon and Y. Gogotsi, "Materials for electrochemical capacitors," *Nature Materials*, vol. 7, no. 11, pp. 845–854, 2008.

[12] H. Shi, "Activated carbons and double layer capacitance," *Electrochim Acta*, vol. 41, pp. 1633–9, 1996.

[13] X. Zhao, B. T. T. Chu, B. Ballesteros, W. Wang, C. Johnston, J. M. Sykes, and P. S. Grant, "Spray deposition of steam treated and functionalized single-walled and multi-walled carbon nanotube films for supercapacitors," *Nanotechnology*, vol. 20, no. 6, 2009.

[14] G. D. Nessim, "Properties, synthesis, and growth mechanisms of carbon nanotubes with special focus on thermal chemical vapor deposition," *Nanoscale*, vol. 2, no. 8, pp. 1306–1323, 2010.

[15] J. Prasek, J. Drbohlavova, J. Chomoucka, J. Hubalek, O. Jasek, V. Adam, and R. Kizek, "Methods for carbon nanotubes synthesis – review," *Journal of Materials Chemistry*, vol. 21, pp. 15872–15884, 2011.

[16] R. Smajda, A. Kukovecz, Z. Konya, and I. Kiricsi, "Structure and gas permeability of multi-wall carbon nanotube buckypapers," *Carbon*, vol. 45, no. 6, pp. 1176–1184, 2007.

[17] R. H. Baughman, C. X. Cui, A. A. Zakhidov, Z. Iqbal, J. N. Barisci, G. M. Spinks, G. G. Wallace, A. Mazzoldi, D. De Rossi, A. G. Rinzler, O. Jaschinski, S. Roth, and M. Kertesz, "Carbon nanotube actuators," *Science*, vol. 284, no. 5418, pp. 1340–1344, 1999.

[18] A. A. Mamedov, N. A. Kotov, M. Prato, D. M. Guldi, J. P. Wicksted, and A. Hirsch, "Molecular design of strong single-wall carbon nanotube/polyelectrolyte multilayer composites," *Nature Materials*, vol. 1, no. 3, pp. 190–194, 2002.

[19] D. N. Futaba, K. Hata, T. Yamada, T. Hiraoka, Y. Hayamizu, Y. Kakudate, O. Tanaike, H. Hatori, M. Yumura, and S. Iijima, "Shape-engineerable and highly densely packed single-walled carbon nanotubes and their application as super-capacitor electrodes," *Nature Materials*, vol. 5, no. 12, pp. 987–994, 2006.

[20] P. J. Hall, M. Mirzaeian, S. I. Fletcher, F. B. Sillars, A. J. R. Rennie, G. O. Shitta-Bey, G. Wilson, A. Cruden, and R. Carter, "Energy storage in electrochemical capacitors: designing functional materials to improve performance," *Energy & Environmental Science*, vol. 3, no. 9, pp. 1238–1251, 2010.

[21] C. Niu, E. K. Sichel, R. Hoch, D. Moy, and H. Tennent, "High power electrochemical capacitors based on carbon nanotube electrodes," *Applied Physics Letters*, vol. 70, no. 11, pp. 1480–1482, 1997.

[22] S. W. Lee, B. S. Kim, S. Chen, Y. Shao-Horn, and P. T. Hammond, "Layer-by-layer assembly of all carbon nanotube ultrathin films for electrochemical applications," *Journal of the American Chemical Society*, vol. 131, no. 2, pp. 671–679, 2009.

[23] E. Frackowiak, K. Metenier, V. Bertagna, and F. Beguin, "Supercapacitor electrodes from multiwalled carbon nanotubes," *Applied Physics Letters*, vol. 77, no. 15, pp. 2421–2423, 2000.

[24] Y.-T. Kim, "Drastic change of electric double layer capacitance by surface functionalization of carbon nanotubes," *Applied Physics Letters*, vol. 87, p. 234106, 2005.

[25] G. Lota, K. Lota, and E. Frackowiak, "Nanotubes based composites rich in nitrogen for supercapacitor application," *Electrochemistry Communications*, vol. 9, no. 7, pp. 1828–1832, 2007.

[26] A. L. M. Reddy, S. R. Gowda, M. M. Shaijumon, and P. M. Ajayan, "Hybrid nanostructures for energy storage applications," *Advanced Materials*, vol. 24, pp. 5045–5064, 2012.

[27] A. P. Graham, G. S. Duesberg, R. V. Seidel, M. Liebau, E. Unger, W. Pamler, F. Kreupl, and W. Hoenlein, "Carbon nanotubes for microelectronics?," *Small*, vol. 1 (4), pp. 382–390, 2005.

[28] Y. M. Vol'fkovich and T. M. Serdyuk, "Electrochemical capacitors," *Russian Journal of Electrochemistry*, vol. 38, no. 9, pp. 935–958, 2002.

[29] J. P. Zheng and T. R. Jow, "High energy and high power density electrochemical capacitors," *Journal of Power Sources*, vol. 62, no. 2, pp. 155–159, 1996.

[30] C. D. Lokhande, D. P. Dubal, and O.-S. Joo, "Metal oxide thin film based supercapacitors," *Current Applied Physics*, vol. 11, no. 3, pp. 255–270, 2011.

[31] J. H. Jiang and A. Kucernak, "Electrochemical supercapacitor material based on manganese oxide: preparation and characterization," *Electrochimica Acta*, vol. 47, no. 15, pp. 2381–2386, 2002.

[32] K. W. Nam, W. S. Yoon, and K. B. Kim, "X-ray absorption spectroscopy studies of nickel oxide thin film electrodes for supercapacitors," *Electrochimica Acta*, vol. 47, no. 19, pp. 3201–3209, 2002.

[33] X. Zhao, C. Johnston, A. Crossley, and P. S. Grant, "Printable magnetite and pyrrole treated magnetite based electrodes for supercapacitors," *Journal of Materials Chemistry*, vol. 20, no. 36, pp. 7637–7644, 2010.

[34] X. Jiang, Y. Wang, T. Herricks, and Y. Xia, "Ethylene glycol-mediated synthesis of metal oxide nanowires," *Journal of Materials Chemistry*, vol. 14, pp. 695–703, 2004.

[35] M. Gratzel, "Photoelectrochemical cells," *Nature*, vol. 414, pp. 338–344, 2001.

[36] M. Salari, K. Konstantinov, and H. K. Liu, "Enhancement of the capacitance in TiO_2 nanotubes through controlled introduction of oxygen vacancies," *Journal of Materials Chemistry*, vol. 21, pp. 5128–5133, 2011.

[37] H. Zhou and Y. Zhang, "Enhancing the capacitance of TiO_2 nanotube arrays by a facile cathodic reduction process," *Journal of Power Sources*, vol. 239, pp. 128–131, 2013.

[38] S. G. Kandalkar, J. L. Gunjakar, and C. D. Lokhande, "Preparation of cobalt oxide thin films and its use in supercapacitor application," *Applied Surface Science*, vol. 254, no. 17, pp. 5540–5544, 2008.

[39] T. Brousse and D. Belanger, "A hybrid Fe_3O_4-MnO_2 capacitor in mild aqueous electrolyte," *Electrochemical and Solid State Letters*, vol. 6, no. 11, pp. A244–A248, 2003.

[40] M. B. Sassin, C. N. Chervin, D. R. Rolison, and J. W. Long, "Redox deposition of nanoscale metal oxides on carbon for next-generation electrochemical capacitors," *Accounts of Chemical Research*, vol. 46 (5), pp. 1062–1074, 2013.

[41] T. Bordjiba and D. Belanger, "Direct redox deposition of manganese oxide on multiscaled carbon nanotube/microfiber carbon electrode for electrochemical capacitor," *Journal of Electrochemical Society*, vol. 156, pp. A378–A284, 2009.

[42] A. Rudge, J. Davey, I. Raistrick, S. Gottesfeld, and J. P. Ferraris, "Conducting polymers as active materials in electrochemical capacitors," *Journal of Power Sources*, vol. 47, no. 1-2, pp. 89–107, 1994.

[43] C. Arbizzani, M. Mastragostino, and L. Meneghello, "Polymer-based redox supercapacitors: A comparative study," *Electrochimica Acta*, vol. 41, no. 1, pp. 21–26, 1996.

[44] J. H. Park, J. M. Ko, O. O. Park, and D. W. Kim, "Capacitance properties of graphite/polypyrrole composite electrode prepared by chemical polymerization of pyrrole on graphite fiber," *Journal of Power Sources*, vol. 105, no. 1, pp. 20–25, 2002.

[45] H. Gomez, M. K. Ram, F. Alvi, P. Villalba, E. Stefanakos, and A. Kumar, "Graphene-conducting polymer nanocomposite as novel electrode for supercapacitors," *Journal of Power Sources*, vol. 196, no. 8, pp. 4102–4108, 2011.

[46] M. Hong, "Use of KCl aqueous electrolyte for 2 V manganese oxide/activated carbon hybrid capacitor," *Electrochemical and Solid State Letters*, vol. 5, pp. 227–230, 2002.

[47] C. Meng, C. Liu, L. Chen, C. Hu, and S. Fan, "Highly flexible and all-solid-state paperlike polymer supercapacitors," *Nano Letters*, vol. 10, pp. 4025–4031, 2010.

[48] H. Gao, F. Xiao, C. B. Ching, and H. Duan, "Flexible all-solid-state asymmetric supercapacitors based on free-standing carbon nanotube/graphene and Mn_3O_4 nanoparticle/graphene paper electrodes," *Applied Materials & Interfaces*, vol. 4, pp. 7020–7026, 2012.

[49] S. Hu, R. Rajamani, and X. Yu, "Flexible solid-state paper based carbon nanotube supercapacitor," *Applied Physics Letters*, vol. 100, 2012.

[50] M. Doyle, M. E. Lewittes, M. G. Roelofs, S. A. Perusich, and R. E. Lowrey, "Relationship between ionic conductivity of perfluorinated ionomeric membranes and nonaqueous solvent properties," *Journal of Membrane Science*, vol. 184, pp. 257–273, 2001.

[51] K.-D. Kreuer, "Proton conductivity: materials and applications," *Chemical Materials*, vol. 8, pp. 610–641, 1996.

[52] F. Lufrano and P. Staiti, "Performance improvement of nafion based solid-state electrochemical supercapacitor," *Electrochimica Acta*, vol. 49, pp. 2683–2689, 2004.

[53] B. G. Choi, J. Hong, W. H. Hong, P. T. Hammond, and H. Park, "Facilitated ion transport in all-solid-state flexible supercapacitors," *ACS Nano*, vol. 5, pp. 7205–7213, 2011.

[54] M. Rikukawa and K. Sanui, "Proton-conducting polymer electrolyte membranes based on hydrocarbon polymers," *Progress in Polymer Science*, vol. 25, pp. 1463–1502, 2000.

[55] F. M. Fowkes and D. O. Tischler, "Acid-base complexes of polymers," *Journal of Polymer Science*, vol. 22, pp. 547–566, 1984.

[56] P. N. Gupta and K. P. Singh, "Characterization of H_3PO_4 based PVA complex system," *Solid State Ionics*, vol. 86-88, pp. 319–323, 1996.

[57] Q. Liu, O. Nayfeh, M. H. Nayfeh, and S.-T. Yau, "Flexible supercapacitor sheets based on hybrid nanocomposite materials," *Nano Energy*, vol. 2, pp. 133–137, 2013.

[58] H. Zheng, T. Zhai, M. Yu, S. Xie, C. Liang, W. Zhao, S. C. I. Wang, Z. Zhang, and X. Lu, "TiO_2@C core-shell nanowires for high-performance and flexible solid-state supercapacitors," *Journal of Materials Chemistry C*, vol. 1, pp. 225–229, 2013.

[59] H. Gao and K. Lian, "Characterizations of proton conducting polymer electrolytes for electrochemical capacitors," *Electrochimica Acta*, vol. 56, pp. 122–127, 2010.

[60] H. Gao and K. Lian, "High rate all-solid electrochemical capacitors using proton conducting polymer electrolytes," *Journal of Power Sources*, vol. 196, pp. 8855–8857, 2011.

[61] V. V. N. Obreja, "Activated carbon based electrodes in commerical supercapacitors and their performance," *International Review of Electrical Engineering*, vol. 5, pp. 272–281, 2010.

[62] W. Zhu, D. Ku, J. P. Zheng, Z. Liang, B. Wang, C. Zhang, S. Walsh, G. Au, and E. J. Plichta, "Buckypaper-based catalytic electrodes for improving platinum utilization and PEMFC's performance," *Electrochimica Acta*, vol. 55, no. 7, pp. 2555–2560, 2010.

[63] B. Gao, G. Z. Yue, Q. Qiu, Y. Cheng, H. Shimoda, L. Fleming, and O. Zhou, "Fabrication and electron field emission properties of carbon nanotube films by electrophoretic deposition," *Advanced Materials*, vol. 13, no. 23, pp. 1770–1773, 2001.

[64] S. V. Fridrikh, J. H. Yu, M. P. Brenner, and G. C. Rutledge, "Controlling the fiber diameter during electrospinning," *Physical Review Letters*, vol. 90, no. 14, 2003.

[65] C. P. Barnes, S. A. Sell, E. D. Boland, D. G. Simpson, and G. L. Bowlin, "Nanofiber technology: Designing the next generation of tissue engineering scaffolds," *Advanced Drug Delivery Reviews*, vol. 59, no. 14, pp. 1413–1433, 2007.

[66] K. C. Krogman, J. L. Lowery, N. S. Zacharia, G. C. Rutledge, and P. T. Hammond, "Spraying asymmetry into functional membranes layer-by-layer," *Nature Materials*, vol. 8, no. 6, pp. 512–518, 2009.

[67] J. H. Kim, K. W. Nam, S. B. Ma, and K. B. Kim, "Fabrication and electrochemical properties of carbon nanotube film electrodes," *Carbon*, vol. 44, no. 10, pp. 1963–1968, 2006.

[68] W. S. Yoon, S. H. Ban, K. K. Lee, K. B. Kim, M. G. Kim, and J. M. Lee, "Electrochemical characterization of layered $LiCoO_2$ films prepared by electrostatic spray deposition," *Journal of Power Sources*, vol. 97-8, pp. 282–286, 2001.

[69] D. Shu, K. Y. Chung, W. I. Cho, and K. B. Kim, "Electrochemical investigations on electrostatic spray deposited $LiMn_2O_4$ films," *Journal of Power Sources*, vol. 114, no. 2, pp. 253–263, 2003.

[70] J. Schoonman, "Nanostructured materials in solid state ionics," *Solid State Ionics*, vol. 135, no. 1-4, pp. 5–19, 2000.

[71] B. Mendoza-Sanchez, B. Rasche, V. Nicolosi, and P. S. Grant, "Scaleable ultra-thin and high power density graphene electrochemical capacitor electrodes manufactured by aqueous exfoliation and spray deposition," *Carbon*, vol. 52, pp. 337–346, 2012.

[72] C. Huang, N. Grobert, A. A. R. Watt, C. Johnston, A. Crossley, N. P. Young, and P. S. Grant, "Layer-by-layer spray deposition and unzipping of single-wall car-

bon nanotube-based thin film electrodes for electrochemical capacitors," *Carbon*, vol. 61, pp. 525–536, 2013.

[73] C. Huang and P. S. Grant, "One-step spray processing of high power all-solid-state supercapacitors," *Scientific Reports*, vol. 3 : 2393, p. DOI: 10.1038/srep02393, 2013.

[74] S. Y. Kim, J. Hong, R. Kavian, S. W. Lee, M. N. Hyder, Y. Shao Horn, and P. T. Hammond, "Rapid fabrication of thick spray-layer-by-layer carbon nanotube electrodes for high power and energy devices," *Energy and Environmental Science*, vol. 6, pp. 888–897, 2013.

Chapter 3

Experimental Techniques

In this chapter, the experimental procedures used throughout the thesis for the fabrication of both film electrodes and solid-state full cell supercapacitors are described, along with various characterisation techniques. The specific experimental details for individual electrode materials and supercapacitors are given in the following results chapters.

3.1 Carbon nanotube treatment

Based on attractive results in the literature and from earlier work in the group, single-wall carbon nanotubes (SWNTs) were chosen first to make individual electrodes. Steam purification was conducted for the as-supplied SWNTs to remove impurities to establish the nanotube electrochemical baseline behaviour. Some SWNTs were then chemically functionalised to introduce pseudo-capacitive performance. However, since SWNTs are

almost ten times more expensive than multi-carbon nanotubes (MWNTs), the SWNTs may not be suitable for making devices in a practical scale. Therefore, MWNTs were used subsequently for making solid-state supercapacitor full cells instead.

3.1.1 Steam purification

As-supplied SWNTs (Thomas Swan & Co. Ltd, Elicarb PR0925) were steam purified according to [1] to remove impurities such as amorphous carbon, graphitic particles and catalytic metal particles in order to maximise the nanotube electrochemical performances. ∼0.5 g SWNTs were placed inside a quartz tube in an alumina tube furnace at 900 ^{o}C for 4 hrs while steam was carried through the alumina tube by bubbling Ar at 190 ml min^{-1} through hot water at 100 ^{o}C to remove any carbon-based impurities. The SWNTs were then refluxed in 6 M HCl at 100 ^{o}C for 6 hrs to remove any remaining catalytic metal particles.

3.1.2 Functionalisation

SWNTs were functionalised to attach charged functional groups on the walls to introduce pseudo-capacitance and to investigate if this strategy could be used to introduce a degree of control of the electrode structure. Two functional groups were attached on the SWNTs, one was -COOH carboxylic group and the other was -NH_2 amine group. The SWNTs were refluxed in 9 M HNO_3 at 120 ^{o}C for 10 hrs to functionalise to SWNT-

COOH. A proportion of the dried SWNT-COOHs were further refluxed with $SOCl_2$ at 70 ^{o}C for 12 hrs before reacting with $NH_2(CH_2)_2NH_2$ in dehydrated toluene at 70 ^{o}C for 24 hrs. The -OH bonds in the -COOH group were broken to be replaced by the -NH-CH_2-CH_2-NH_2 groups on the SWNT exterior walls, with the NH_2 groups at the end, and is abbreviated to SWNT-NH_2 [2]. The carboxylic functionalised SWNTs became negatively charged with -COO^- and the amine functionalised SWNTs became positively charged with -$NH_3{}^+$ in aqueous suspensions with pH values of 3 and 2.5 respectively.

3.2 Electrode and supercapacitor fabrication

The film electrodes and supercapacitors described in this thesis were produced by an atomisation spray deposition technique developed at Oxford [3, 4, 5, 6]. A homogeneous and stable suspension of the electrode nanomaterial in deionised (DI) water was firstly prepared, and then individual electrodes or full cells were fabricated.

3.2.1 Suspension preparation

Table 3.1 summarises the aqueous-based suspensions prepared for the four types of carbon nanotube (CNT)-based electrode materials described in this thesis. Suspension (a) was used to establish a baseline haviour for the electrodes and solid-state supercapac-

itors upon which further functionalisation or functional materials were incorporated. Suspension (b) was used to fabricate individual electrodes and study their structure-performance relationship (Chapter 4). Suspensions (c) and (d) were used to make solid-state supercapacitors (Chapters 5 and 6).

The CNT concentraion of all suspensions was 2 mg ml^{-1}. Nafion ionomer (Sigma-Aldrich) of 50 wt% (wt% of the CNTs in the suspension) was added in suspensions (c) and (d) in Table 3.1. ∼30 nm sized TiO_2 nanoparticles (Sigma-Aldrich) of 1 mg ml^{-1} concentration was added in suspension (d). Suspensions (a) and (d) used a 0.1 wt% sodium dodecylbenzenesulfonate (SDBS) surfactant to obtain a homogeneous dispersion, whereas (b) and (c) did not require any surfactant as the functional groups or ionomer provided sufficient nanotube stability in DI water. All suspensions appeared homogeneous to the eye after ultrasonicating (600 W, 20 kHz) for 15 mins. Detailed suspension compositions will be described again in individual corresponding chapters.

	Suspension	Composition	Solvent
(a)	Pure CNTs (both SWNTs and MWNTs)	CNT + 0.1 wt% SDBS (wt% of the CNTs)	DI water
(b)	Functionalised SWNTs	SWNT-COOH or SWNT-NH_2	DI water
(c)	MWNT/ionomer	MWNT + 50 wt% ionomer	0.5 M H_2SO_4 in DI water
(d)	MWNT/TiO_2/ionomer	MWNT + 1 mg ml^{-1} TiO_2 + 50 wt% ionomer + 0.1 wt% SDBS	0.5 M H_2SO_4 in DI water

Table 3.1: A summary of the suspensions for the four types of electrode materials used in this thesis.

3.2.2 Spray deposition of electrodes

Purified SWNT and functionalised SWNT-based electrodes were made by spray deposition of the suspensions onto ITO-coated glass slides. Fig. 3.1 shows the spray configuration, with the key parts of: a syringe pump (PUMP-NE-300-U from New Era Pump system), industrial spray nozzles (Lechler Ltd), an Al heating plate (30 cm x 30 cm, Hillesheim) and an x-y stage controlling the heating plate movement. The suspension was delivered to the nozzle by a syringe pump at 3 ml min^{-1}, and the suspension was atomised continuously in the nozzle by a compressed air stream at 310 kPa. The spray was directed vertically downwards onto a heated substrate at a spray distance of 20 cm. The substrate was placed on a heating plate at 100 ^{o}C which moved according to a pre-programmed x-y zig-zag pattern at a speed of 100 mm s^{-1} with a typical spray area of 10 cm x 10 cm. The DI water in the suspension evaporated continuously during the spray process so there was no excessive build-up of liquid on the substrate and the electrode material adhered readily. The thickness of the sprayed films was controlled by the spray duration, and all spray processing took place entirely within a dedicated fume hood. Fig. 3.1 shows that for a layer-by-layer (LbL) assembly, negatively charged SWNT-COOH and positively charged SWNT-NH_2 were sprayed sequentially by two nozzles, which will be discussed in more detail in Chapter 4.

Fig. 3.2(a) shows that the spray nozzle consisted of five parts: spreader, fluid nozzle, needle, main body and ports. Fig. 3.2(b) shows that five inlet ports were directed to

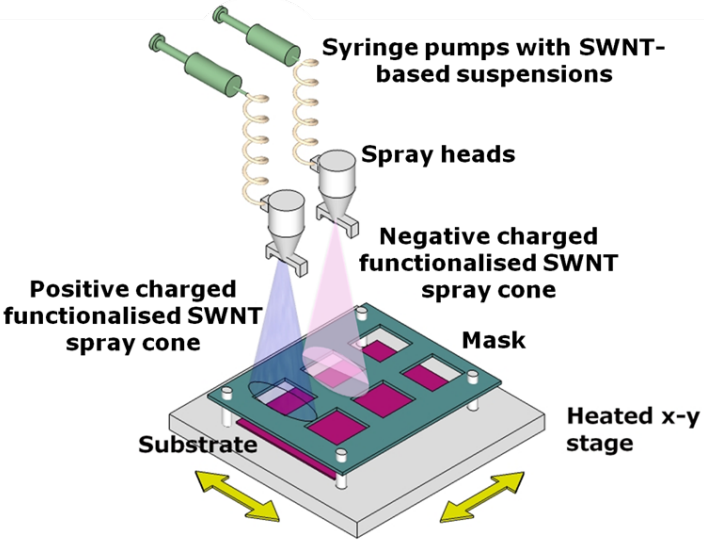


Figure 3.1: A schematic diagram of the spray deposition configuration.

the main body: one for piston air (controls the position of the needle), one for atomising air (mixes and atomises the liquid from the fluid nozzle to form fine (<50 μm) liquid droplets) and one for fan air (controls the spray cone shape). By varying the atomising and fan air pressure, the desired droplet size and spray pattern could be achieved. The other two ports were for feeding suspensions. Normally, only one suspension port was needed, but two can be used if spraying different suspensions from one nozzle is required.

3.2.3 Spray deposition of flexible solid-state supercapacitors

Membranes (Nafion, 70μm thickness, Du Pont) were pre-treated by immersing in 1 M H_2SO_4 at 60 °C for 30 min. The stable suspensions of MWNT+ionomer or MWNT+TiO_2 +ionomer were then pumped at 3 ml min^{-1} into a spray nozzle, atomised and deposited onto one side of the membrane that was maintained at 100 °C on a heating plate con-

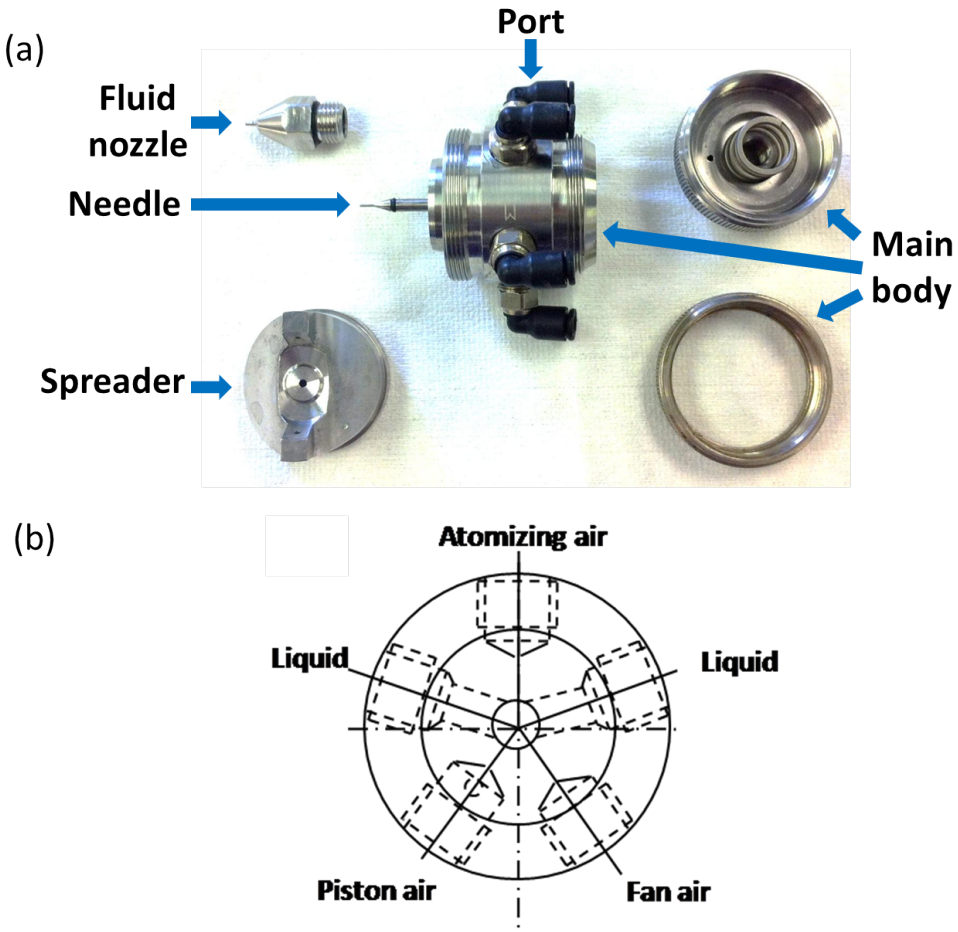


Figure 3.2: (a) Nozzle parts; and (b) a schematic diagram of the five ports directed to the main nozzle body.

nected to a vacuum chuck beneath the spray heads. For flexible substrates such as the Nafion membrane, the vacuum chuck ensured stable and reproducible close contact with heating plate. The membrane with one side covered with the sprayed thin film electrode was then flipped and sprayed on the other side using the identical procedure. A typical size for a fabricated solid-state supercapacitor was 4.5 cm x 4 cm, and the thickness of each electrode was controlled by the spraying duration to be 10-70 μm.

3.3 Physical characterisation

3.3.1 Electrode thickness

Electrode thickness was measured using a Dektak 6M profilometer (Veeco Instruments Inc) where a smooth substrate half covered with a film electrode was placed on the sample stage and a diamond-tipped stylus measured the vertical displacement of the stylus between the smooth substrate and the electrode top surface. Si substrates were used as a reference to zero the profile, and a 5 mN stylus force with a 8,000 μm scan length was used for all measurements. The film thickness was measured in five locations on each sample and an average obtained.

3.3.2 Raman spectroscopy

The bonding and structure of the as-received materials and the sprayed electrodes were characterised by Raman spectroscopy (Horiba LabRAM ARAMIS) with a 532 nm wavelength laser. As-received CNTs and TiO_2 (both in a powder form) and the sprayed electrodes were placed on a glass slide and investigated directly under the Raman spectroscopy. A wavelength spectrum of 100-3250 cm^{-1} was used for scanning the samples.

3.3.3 X-ray photoelectron spectroscopy

The surface chemistry of the as-received materials and sprayed film electrodes was analysed by X-ray photoelectron spectroscopy (XPS) in an ion pumped VG Microtech CLAM 4 multi-channel detecting analyser equipped with a Mg K_α source. The samples were placed on XPS sample holders by sticky carbon tabs. The XPS analyser operated at a constant pass energy of 100 eV for wide scans and 20 eV for detailed scans.

3.3.4 Scanning electron microscopy

The surface morphology and interior structure of the electrodes were examined by scanning electron microscopy (SEM, JEOL 840F, cold field emission gun operated at 3 kV; and JEOL 6500F, Schottky field emission gun operated at 5 kV). The samples were mounted onto Al stubs with a silver conducting paint placed along the edge to avoid

charging. For examining the electrode interior structure, ITO coated glass substrates covered with sprayed electrodes were snapped in liquid N_2 to expose the electrode cross-section.

3.3.5 Transmission electron microscopy

To investigate the structure of the materials and sprayed electrodes further, transmission electron microscopy (TEM) images and diffraction patterns were taken using a JEOL 2010 (LaB_6 electron gun operated at 100 kV). The majority of the TEM images were done by the author alone, and the diffraction patterns of multi-layer graphene sheets in Chapter 4 were done by Dr Neil P. Young and the author together. High-angle annular dark-field (HAADF) images were acquired in a scanning transmission electron microscope (STEM, JEOL 3000F, Schottky field emission gun operated at 300 kV) to observe multi-layer graphene sheets in Chapter 4, by Dr Neil P. Young and the author together. A high resolution TEM (HRTEM) image (JEOL 3000F, 300 kV) of TiO_2 nanoparticle coated with a thin layer of ionomer in Chapter 6 was done by Dr Neil P. Young. All of the TEM samples were prepared by placing a holey-carbon film-coated Cu grid (300 mesh) on the sprayed electrodes with one drop of ethanol.

3.4 Electrochemical characterisation

Electrochemical properties were characterised through cyclic voltammetry (CV), galvanostatic charge/discharge, AC impedance and cycling by a Gamry Reference 600 Electrochemical Analyser in both a three-electrode configuration (to obtain detailed behaviour of one electrode) and a two electrode full cell configuration. For the three-electrde configuration, the testing sample was the working electrode, and a Pt wire and Ag/AgCl were used as the counter and reference electrodes respectively. 1 M H_2SO_4 was used as an electrolyte, which was bubbled with N_2 for 20 min prior to testing to remove any impurities. The two-electrode full cells were tested both in a Swagelok cell or in the case of solid-state devices, simply in air on the laboratory bench. Fig. 3.3(a) shows a Swagelok cell and its parts, as well as a typical sample (1 cm in diameter) of a Nafion membrane with two sides covered with electrodes to be placed inside the Swagelok cell for testing. Fig. 3.3(b) shows a stack of three solid-state full cells (4.5 cm x 4 cm) tested in air without the need for any packaging (details in Chapter 5).

3.4.1 Cyclic voltammetry

In a cyclic voltammetry (CV) test, the working electrode potential was ramped linearly versus time to a set potential, and then the ramp was inverted, for a set number of cycles. The current at the working electrode was plotted against the applied voltage to give a cyclic voltammogram trace. A potential window of $\sim$1 V was used for measuring

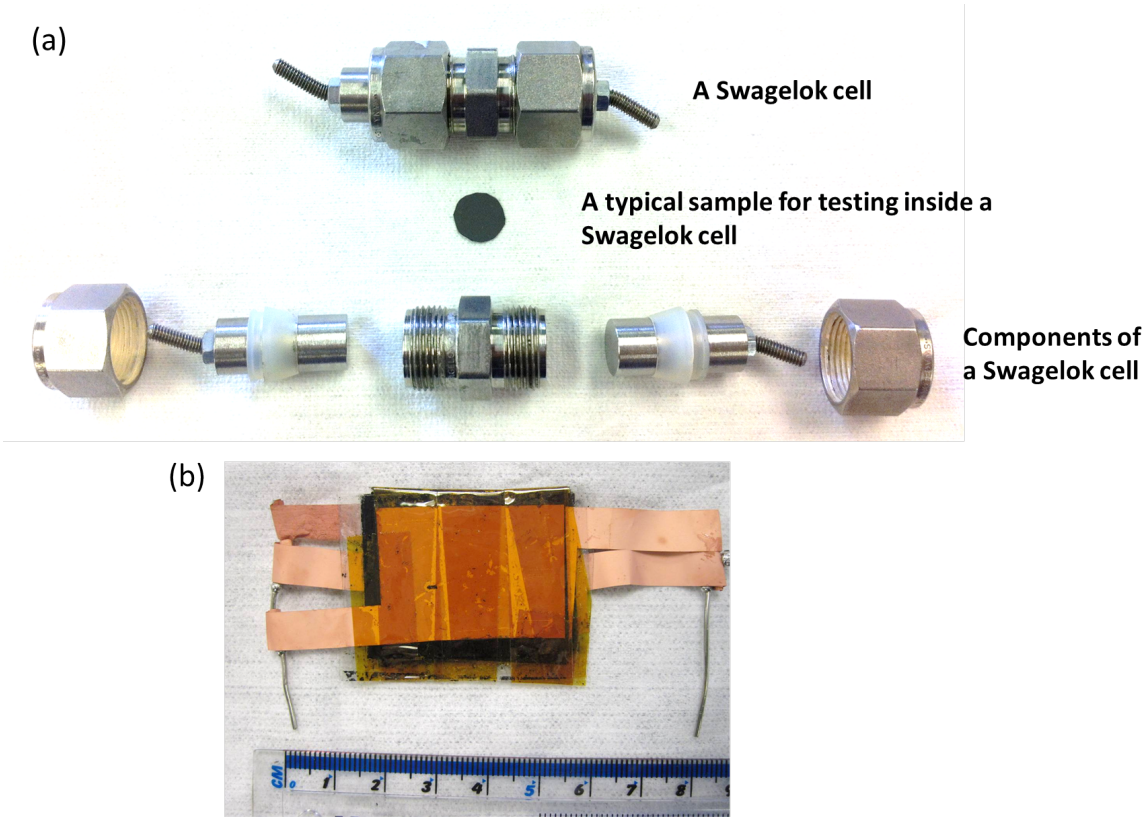


Figure 3.3: (a) A Swagelok cell used for the full cell electrochemical tests; and (b) a stack of three solid-state supercapacitors which was simply exposed to air without any packaging during testing.

the systems with aqueous-based electrolytes due to electrolysis of water and evolution of hydrogen which may occur at a >1 V voltage window, whereas a maximum of 2.7 V was used for the solid-state supercapacitors because no liquids were involved. A range of scan rates from 1 to 500 mV s^{-1} was used. The specific capacitance was estimated by integrating the area under the current-potential curve and then dividing by the sweep rate, the mass of film electrode and the potential window according to [7]:

$$C = \frac{1}{mv(V_a - V_c)} \int_{V_a}^{V_c} I(V)dV \tag{3.1}$$

where C is the specific capacitance (F g^{-1}), m is the mass of one electrode (g), v is the scan rate (V s^{-1}), V_a-V_c represents the potential window (V), and I is either the charging or discharging current (A). The capacitances calculated from the CV charging and discharging currents for the symmetrical carbon-based supercapacitor were similar, since no dominating reactions took place at either anodic or cathodic scan [8] [9].

3.4.2 Galvanostatic charge/discharge

Galvanostatic charge/discharge testing measures the time taken for the sample or a full cell to reach a set potential at a constant current. Current densities of 1 and 2 A g^{-1} were used. The capacitance was estimated from the slope of the discharge curve according to Equation 3.2, where the discharge current I is normally used and t is the

corresponding discharge time (s) from a voltage V [8]. Only the linear parts of the curves were used in the calculation of capacitances.

$$C = \frac{I}{m\frac{dV}{dt}} \tag{3.2}$$

As a full cell can be treated as two capacitors in series, the overall capacitance $C_{overall}$ of one cell was calculated according to:

$$\frac{1}{C_{overall}} = \frac{1}{C_1} + \frac{1}{C_2} \tag{3.3}$$

in which C_1 and C_2 are the capacitances of individual electrodes and are assumed equal in a symmetrical cell. Therefore, the overall capacitance of a full cell is a half of that of one electrode.

The maximum energy E and power density P can be expressed as [8]:

$$E = \frac{1}{2}\frac{CV^2}{m} \tag{3.4}$$

$$P = \frac{V^2}{4R_s m} \tag{3.5}$$

where R_s is the equivalent internal resistance [10].

3.4.3 Electrochemical impedance spectroscopy

Electrochemical impedance spectroscopy (EIS) was performed to study the impedance of a system as a function of frequency by using an AC sinusoidal voltage signal of 5 mV rms and a frequency from 0.01 to 10^6 Hz at room temperature. EIS generates a plot of imaginary resistance against real resistance (Nyquist plot), in which the equivalent series resistance (ESR) was estimated by extrapolation of a best-fit line to the real resistance axis and the charge transfer resistance was estimated from the diameter of the semi-circle of the best-fit line at high frequencies.

3.4.4 Cycling

The flexible solid-state supercapacitors were tested for $\geq$2000 cycles of galvanostatic charge/discharge at a constant current density of 1 A g^{-1} at room temperature to study long-term stability.

Bibliography

[1] G. Tobias, L. D. Shao, C. G. Salzmann, Y. Huh, and M. L. H. Green, "Purification and opening of carbon nanotubes using steam," *Journal of Physical Chemistry B*, vol. 110, no. 45, pp. 22318–22322, 2006.

[2] S. W. Lee, B. S. Kim, S. Chen, Y. Shao-Horn, and P. T. Hammond, "Layer-by-layer assembly of all carbon nanotube ultrathin films for electrochemical applications," *Journal of the American Chemical Society*, vol. 131, no. 2, pp. 671–679, 2009.

[3] X. Zhao, B. T. T. Chu, B. Ballesteros, W. Wang, C. Johnston, J. M. Sykes, and P. S. Grant, "Spray deposition of steam treated and functionalized single-walled and multi-walled carbon nanotube films for supercapacitors," *Nanotechnology*, vol. 20, no. 6, 2009.

[4] B. Mendoza-Sanchez, B. Rasche, V. Nicolosi, and P. S. Grant, "Scaleable ultra-thin and high power density graphene electrochemical capacitor electrodes manufactured by aqueous exfoliation and spray deposition," *Carbon*, vol. 52, pp. 337–346, 2012.

[5] C. Huang, N. Grobert, A. A. R. Watt, C. Johnston, A. Crossley, N. P. Young, and P. S. Grant, "Layer-by-layer spray deposition and unzipping of single-wall carbon nanotube-based thin film electrodes for electrochemical capacitors," *Carbon*, vol. 61, pp. 525–536, 2013.

[6] C. Huang and P. S. Grant, "One-step spray processing of high power all-solid-state supercapacitors," *Scientific Reports*, vol. 3 : 2393, p. DOI: 10.1038/srep02393, 2013.

[7] V. Srinivasan and J. W. Weidner, "Capacitance studies of cobalt oxide films formed via electrochemical precipitation," *Journal of Power Sources*, vol. 108, pp. 15–20, 2002.

[8] P. L. Taberna, P. Simon, and J. F. Fauvarque, "Electrochemical characteristics and impedance spectroscopy studies of carbon-carbon supercapacitors," *Journal of the Electrochemical Society*, vol. 150 (3), pp. A292–A300, 2003.

[9] T. W. Jones, A. P. Lewandowski, and S. W. Donne, "Discharge performance of a primary alkaline CuO cathode material prepared via a novel non-aqueous precipitation method," *Electrochimica Acta*, vol. 56, pp. 4996–5002, 2011.

[10] M. D. Stoller and R. S. Ruoff, "Best practice methods for determining an electrode material's performance for ultracapacitors," *Energy & Environmental Science*, vol. 3, pp. 1294–1301, 2010.

Chapter 4

Layer-by-layer spray deposition and heat treatments of single-wall carbon nanotube-based thin film electrodes for supercapacitors

4.1 Introduction

Single-wall carbon nanotube (SWNT) based electrodes have some attractions because of their enhanced electrical conductivity $> 5\times10^5$ Sm^{-1} [1], excellent electrochemical cycling behaviour (>5000) and mechanical stability in most electrolytes without parasitic additives [2]. In the absence of chemical or physical manipulation, both SWNTs and multi-wall carbon nanotubes (MWNTs) have a tendency to tangle and agglomer-

ate in an uncontrolled manner and many surface modification treatments for carbon nanotubes (CNTs) in a variety of suspensions have been developed that have allowed CNTs to be formed into various electrodes [3]. The resulting interconnected, meso-porous CNT network structures facilitate high H^+, Li^+, K^+ ion mobilities, and the efficient formation of an electric double layer (EDL) in supercapacitors at the carbon surface, resulting in high power densities above 8 kW kg^{-1} in laboratory scale devices with a comparatively low electrolyte/electrode resistance [4]. CNTs also offer myriad opportunities for covalent functionalisation to improve their capacitive behaviour through participation in faradaic reactions (pseudo-capacitance) [5] or to increase chemical compatibility (wetting) with the electrolyte [6].

Chapter 2 has described that the meso-porous structure and surface area of activated carbon-based supercapacitor electrodes can be tailored by variations in particle size and distribution, activation process parameters, proportions of various additives, and the slurry casting and subsequent rolling parameters [7]. However, for more immature CNT-based electrodes, analogous material approaches and processes with similar flexibility are not obvious, and therefore it remains unclear how the CNT meso-porous structure might be "designed" for performance or selected in advance by using a technique that can scale to realistic electrode areas, and what ranges of meso-porous structures might be available. One approach is to use a layer-by-layer (LbL) approach in which, for example and as used here, MWNTs are functionalised with carboxylic COO^- or amine $NH_3{}^+$ groups, and then assembled together sequentially, layer-by-layer, by alternately

dip coating in the oppositely charged MWNT suspensions [8]. The idea is that the MWNTs then form a less open, more compact meso-porous structure due to electrostatic attraction between the layers, that provides an improvement in volumetric or gravimetric performance of the electrode. From a practical standpoint, attaching oppositely charged groups is also helpful to speed up the relatively slow dip coating process. An LbL film made in this way improved mechanical integrity and consistency of thickness compared with pure MWNT films [8]; there was also a capacitance improvement, although the literature was not explicit in rationalising the effects of LbL processing with reference to any demonstrated change in the electrode structure.

In this chapter, SWNT aqueous-based suspensions functionalised with COO^- and NH_3^+ were spray deposited alternately onto a heated substrate from a multi-head, dual feed spray device. The oppositely charged layers were electrostatically attracted and the electrode density was increased compared with a SWNT-COOH only electrode. Subsequent electrochemical behaviour was investigated in a 1 M H_2SO_4 electrolyte and the systematic changes in behaviour rationalised by the likely process taking place during meso-porous structural evolution of the electrodes, supported by surface chemistry analysis by X-ray photoelectron spectroscopy, electrical conductivity measurements and detailed microstructural analysis. Subsequent vacuum and H_2 heat treatments were used to remove the functional groups [8] since amine groups have no helpful faradaic activity in H_2SO_4 and likely undermine the overall capacitance. This post-spray treatment, unexpectedly, resulted in the formation of graphene sheets formed from unzipped

SWNTs and a hybrid SWNT/multi-layer graphene structure with a high capacitance of 151 F g^{-1} at 2 mV s^{-1}.

4.2 Materials and methods

The steam purification and fuctionalisation of SWNTs have been described in Section 3.1. This section will focus on the LbL processing of the electrodes and their subsequent heat treatments.

4.2.1 LbL spray deposition of functionalised SWNTs

Aqueous suspensions of purified SWNTs, carboxylic functionalised SWNTs and amine functionalised SWNTs were separately made at a concentration of 2 mg ml^{-1}. For the SWNT-only suspension, 0.1 wt% sodium dodecylbenzenesulfonate (SDBS, Sigma-Aldrich) was added as a surfactant to prevent agglomeration. The pH values of SWNT-COO^- and SWNT-NH_3^+ suspensions were adjusted to 3 and 2.5 respectively to obtain stable suspensions without surfactant because the charges on the functional groups provided electrostatic stabilisation. The SWNT-based aqueous suspensions were spray deposited onto indium tin oxide (ITO)-coated glass slides and Si wafers maintained at 100 ^oC. For the LbL assembly, two spray heads, one with SWNT-COO^- and the other with SWNT-NH_3^+, were used to spray $\sim$200 nm layers alternately, until a total of 10 layers were deposited. To enhance the adhesion of the SWNT-based films

on the ITO-coated glass slides and Si wafers, a few 10's nm layer of 1 wt% branched poly(ethyleneimine) (PEI-b, Alfa-Aesar) aqueous suspension was pre-sprayed onto the substrates [9]. Some of the SWNT-COOH and LbL electrodes were then heated in vacuum at 150 ^{o}C for 30 mins and in a H_2 atmosphere at 300 ^{o}C for 2 hrs [8].

4.2.2 Characterisation

The weight of the deposited electrodes was measured by a microbalance (Sartorius, Germany) with 0.01 mg accuracy, and thickness measured using a Dektak 6M profilometer (Veeco Instruments Inc, USA). Together with a known carefully controlled area of substrate sprayed, these data allowed the electrode density to be estimated. Typical electrode thicknesses were 2 to 3 μm, and a typical electrode area on the ITO-coated glass slides was 1 cm x 1 cm. Surface chemistry of the functionalised SWNTs at each stage of processing was analysed by X-ray photoelectron spectroscopy (XPS) in an ion pumped VG Microtech CLAM 4 multi-channel detecting analyser equipped with a Mg K_α source, with electrodes deposited on Si wafers. The XPS analyser operated at a constant pass energy of 100 eV for wide scans and 20 eV for detailed scans.

The conductivity of the electrodes was measured by using a standard four-point probe configuration and a Keithley 220 programmable current source meter on the electrodes deposited on both Si wafers and ITO-coated glass slides, with measurements repeated 8 times on each electrode. A three-electrode cell configuration was used for electro-

chemical measurements where cyclic voltammetry (CV) was performed in a 1 M H_2SO_4 electrolyte between -0.25 and 0.80 V at scan rates in the range of 1 to 250 mV s^{-1}.

4.3 Results and discussion

4.3.1 Surface chemistry and density of functionalised SWNT electrodes

Wide scan 0-1100 eV spectra for the as-sprayed SWNT, SWNT-COOH and LbL SWNT-COOH/SWNT-NH_2 electrodes as well as the LbL electrode after heating in vacuum at 150 ^{o}C and H_2 at 300 ^{o}C, all on Si substrates, are shown in Fig. 4.1. Table 4.1 shows a summary of XPS and other data for all the electrodes. All of the samples showed a strong C_{1s} photoemission peak at 284 eV, and the relative intensity of the O_{1s} peak at 532 eV was higher in the SWNT-COOH electrode than the LbL electrodes before and after heat treatment, indicative of a larger proportion of surface O-containing carboxylic functional groups in the SWNT-COOH electrode. The high intensity of O_{1s} peak for the SWNT electrode may be due to large molecule sodium dodecylbenzenesulfonate (SDBS) surfactant within the electrode. The spectrum for the SWNT electrode showed high intensity peaks at 1071 eV assigned to Na_{1s}, 265-332 eV assigned to Na_{Auger}, and low intensity peaks at 63 eV assigned to Na_{2p}, 169 eV assigned to S_{2p}, all indicative of SDBS. The spectrum for the as-sprayed LbL electrode showed a peak at 400 eV assigned

to N_{1s}, confirming the presence of N-containing groups such as amine. The intensity of the N_{1s} peak was reduced to an almost negligible intensity for the LbL electrode after vacuum and H_2 heat treatments. The XPS data estimated that the atomic weight of N on the surface decreased from 3.2 % for the as-sprayed LbL electrode to 0.6 % after vacuum and H_2 heating, suggesting almost complete removal of the N-containing groups after heat treatments. Since the electrodes were deposited on Si substrates, weak Si peaks at 103 and 154 eV were also detected.

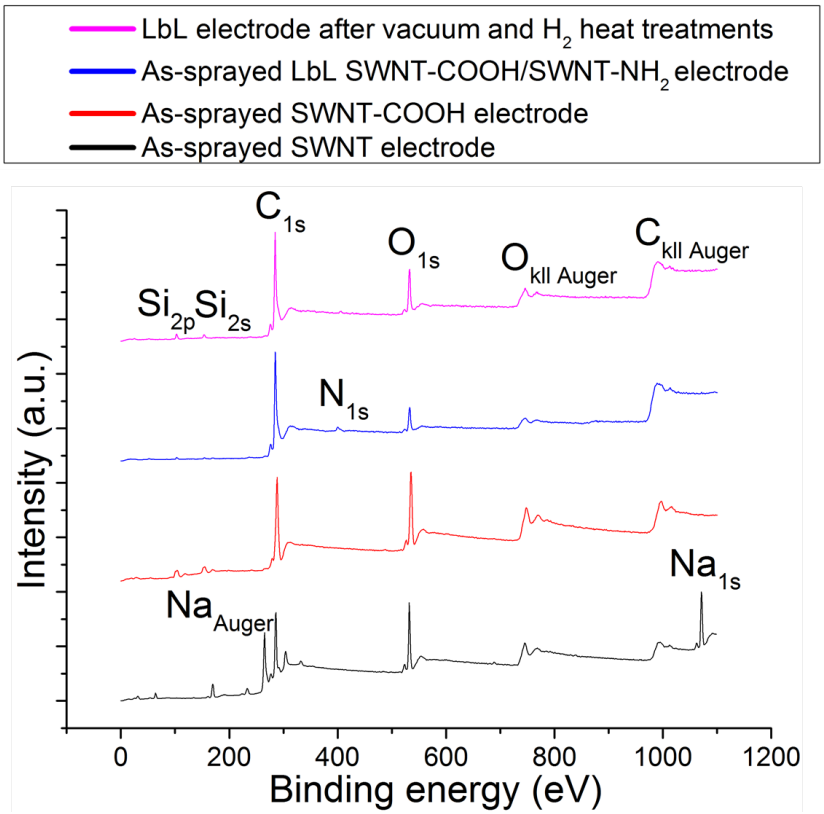


Figure 4.1: X-ray photoelectron spectroscopy (XPS) wide scan spectra of the as-sprayed SWNT electrode with SDBS surfactant; as-sprayed SWNT-COOH electrode; as-sprayed LbL SWNT-COOH/SWNT-NH_2 electrode; and the LbL electrode after heating in vacuum at 150 ^{o}C and H_2 at 300 ^{o}C.

Fig. 4.2(a) shows more detail of the spectrum for C_{1s} from the as-sprayed SWNT-COOH electrode. There was a significant peak from sp^2 hybridised C bonds at 284.5 eV, and the spectrum was deconvoluted into three further Gaussian-Lorentzian peaks at 286.2 eV assigned to C-O, 288.4 eV assigned to O=C-O, and 288.9 eV assigned to O=C-OH [10]. Similarly, Fig. 4.2(b) shows the zoomed in region for the N_{1s} spectrum for the as-sprayed SWNT-COOH electrode, indicating only oxidised nitrogen impurities (NO_x) at 406.2 eV. In contrast, Fig. 4.2(c) shows the similar N_{1s} spectrum for the as-sprayed LbL electrode with a peak at 400.5 eV suggestive of amine groups due to C-NH_2 bonds. Fig. 4.2(d) shows the N_{1s} spectrum for the LbL SWNT-COOH/SWNT-NH_2 electrode after heating in vacuum at 150 ^oC, with a strong N-C=O peak developed at 402.1 eV, indicative of a reaction between SWNT-COOH and SWNT-NH_2 and the formation of amide bonds. Even though XPS only detects the kinetic energy and number of electrons escaping from the top 1 to 10 nm of solid samples [10], the electrode porosity may allow some further penetration and signal generation from regions below the surface. The strong amide signal indicated that there was reasonable mixing between the SWNT-COOH and SWNT-NH_2 layers during spraying, and that any COO^-/NH_3^+ interactions were taking place not only at the interface between one layer and another, but more widely through the electrode as it formed.

Table 4.1 shows a summary of the as-sprayed electrodes, any heat treatments applied, surface groups detected by XPS, thicknesses, densities and conductivities for the SWNT, SWNT-COOH and LbL SWNT-COOH/ SWNT-NH_2 with the same sample size of 1

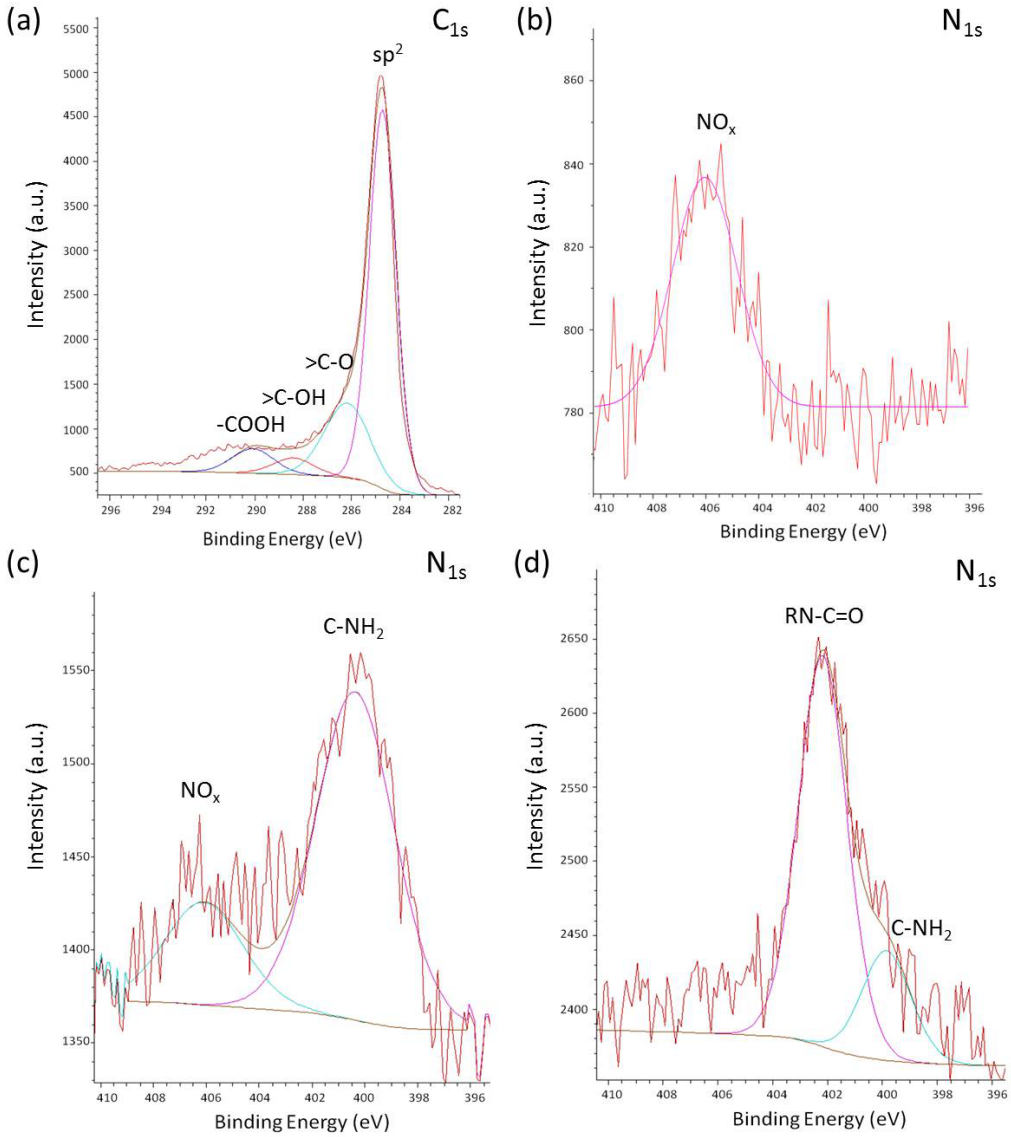


Figure 4.2: X-ray photoelectron spectroscopy detailed scan spectra from the various sprayed SWNT-based electrodes: (a) C_{1s} for SWNT-COOH; (b) N_{1s} for SWNT-COOH; (c) N_{1s} for SWNT-NH_2; and (d) N_{1s} for LbL SWNT-COOH/SWNT-NH_2 after heating in vacuum at 150 ^{o}C for 30 mins.

cm x 1 cm. The same electrode material mass of $\sim$1 mg cm^{-2} was sprayed onto each current collector with a mass deviation of $\sim$3%. The SWNT electrode had an average thickness of 3.2 μm and the lowest as-sprayed density of 0.68 g cm^{-3}, due to the effective repulsion of the large molecule SDBS surfactant. The SWNT-COOH electrode did not

require any additional surfactant since the suspension was stabilised by the carboxylic groups on the SWNT exterior walls, and the electrode thickness and density were almost identical. The LbL electrode had an average thickness of 1.9 μm and the highest density of $\sim$1.1 g cm^{-3}, as intended, which was indicative of large-scale electrostatic interaction between the opposite charged layers, previously suggested by the XPS data. After heating in vacuum at 150 ^{o}C for 30 mins, the LbL electrode decreased in density by $\sim$18 %. The XPS data in Fig. 4.2(d) showed that the relative intensity of N-C=O amide bond increased with respect to the NH_2 amine bond at this stage, suggesting a conversion of amine to N-C=O amide bonds reduced the density. On further treatment in H_2 at 300 ^{o}C for 2 hrs, the electrode thickness increased and the density decreased dramatically as all functional groups were removed (confirmed by XPS in Fig. 4.1), and electrostatic and chemical interactions between the SWNTs relaxed. As shown later, this dramatic change in density also arose from fundamental changes in the electrode nanostructure. The stable, but relatively low density of the SWNT-COOH electrode ($\sim$0.69 g cm^{-3} before and after vacuum and H_2 heating) may be due to their lack of strongly interacting functionalisations, and were thus relatively unaffected by their removal.

Electrode	Heat treatment	Surface groups by XPS				Thickness	Density	Electrical conductivity
		-COOH	$-NH_2$	$-NO_x$	-CONH	(μm)	(mg cm^{-3})	(S cm^{-1})
Purified SWNT	None	None	None	Strong	None	3.2	677	10.5
SWNT-COOH	None	Strong	None	Strong	None	3.1	689	0.7
SWNT-COOH	Vacuum at 150 ^{o}C for 30 min	Weak	None	Weak	None	2.8	691	2.1
SWNT-COOH	Vacuum at 150 ^{o}C for 30 min + H_2 at 300 ^{o}C for 2 hrs	Very weak	None	None	None	2.7	693	10.8
LbL	None	Strong	Strong	Weak	None	1.9	1116	14.5
LbL	Vacuum at 150 ^{o}C for 30 min	Weak	Weak	None	Strong	2.4	920	12.3
LbL	Vacuum at 150 ^{o}C for 30 min + H_2 at 300 ^{o}C for 2 hrs	Very weak	None	None	Weak	4.4	453	10.9

Table 4.1: A summary of the SWNT-based electrodes prepared by spray deposition, their heat treatments, densities and electrical conductivities after the heat treatments (LbL is an abbreviation of layer-by-layer assembly of ten alternating layers of SWNT-COOH and SWNT-NH_2).

4.3.2 Electrical conductivity of SWNT-based electrodes

Table 4.1 also shows the electrical conductivity of the electrodes of SWNT, SWNT-COOH, LbL SWNT-COOH/SWNT-NH_2 and LbL after vacuum and H_2 heating. The SWNT only electrode conductivity was 10.5 S cm^{-1}, decreasing significantly to 0.7 S cm^{-1} after carboxylic functionalisation. Although no surfactant was added in SWNT-COOH, the surface -COOH groups inhibited the in-plane current carrying capability of the SWNTs. The conductivity of the as-sprayed LbL electrode increased to 14.5 S cm^{-1} despite possible negative effects of the -COOH groups on conductivity, because the interaction between the -COOH and -NH_2 groups led to a denser, more compact electrode, where bridging and current transfer between the SWNTs was improved. A similar as-manufactured approximately 280 nm thick LbL electrode made by dip-coating had a conductivity of 2 S cm^{-1} [8]. Since [8] also reported that electrical conductivity increased with increasing thickness, the performance of the sprayed LbL 2.4 μm thick electrode appears encouraging. For further comparison, LbL electrophoretic build-up of graphene sheets and gold nanoparticles to a thickness of $\sim$150 nm had a conductivity of 8.3 S cm^{-1} [11]. Overall, the conductivity of the present spray deposited LbL SWNT-COOH/SWNT-NH_2 electrode is amongst the highest in the literature for equivalent arrangements [12, 11, 13].

The LbL electrode conductivity reduced slightly to 10.9 S cm^{-1} after vacuum and H_2 heating. Since the XPS data in Fig. 4.1 confirmed the removal of functional groups

after vacuum and H_2 heat treatments, this suggests that -COOH and -NH_2 may have made a direct contribution to electron mobility, or that the bridging and interconnection between SWNTs was slightly reduced once electrostatic interaction was absent.

4.3.3 Electrochemical properties of SWNT-based electrodes

Fig. 4.3(a) shows the cyclic voltammogram for a sprayed electrode of steam purified SWNTs with SDBS surfactant in 1 M H_2SO_4. The voltammogram was a slanted parallelogram shape without any significant superimposed peaks, indicative of EDL capacitive behaviour but with a resistive element. The specific capacitance of the purified SWNTs at 2 mV s^{-1} was 29 F g^{-1} where mass refers to the mass of sprayed electrode and 5.9 mF cm^{-2} where area refers to geometric area of the sprayed electrode. For electrodes built from carbon nanotubes, reported specific capacitances are in a wide range from 4-190 F g^{-1} [14], with "pure" EDL capacitance in the lower end of the range, and various functionalised CNTs with pseudo-capacitance at the higher end. Although the purified SWNTs had higher conductivity than SWNT-COOH, the SWNT capacitance may have been reduced by the surfactant within this electrode that blocked some pores and covered the surface of the carbon nanotubes, reducing the active areas contributing to energy storage [15].

The voltammogram for the SWNT-COOH electrode in Fig. 4.3(b) deviated more strongly from EDL capacitive behaviour with a pair of superimposed additional peaks

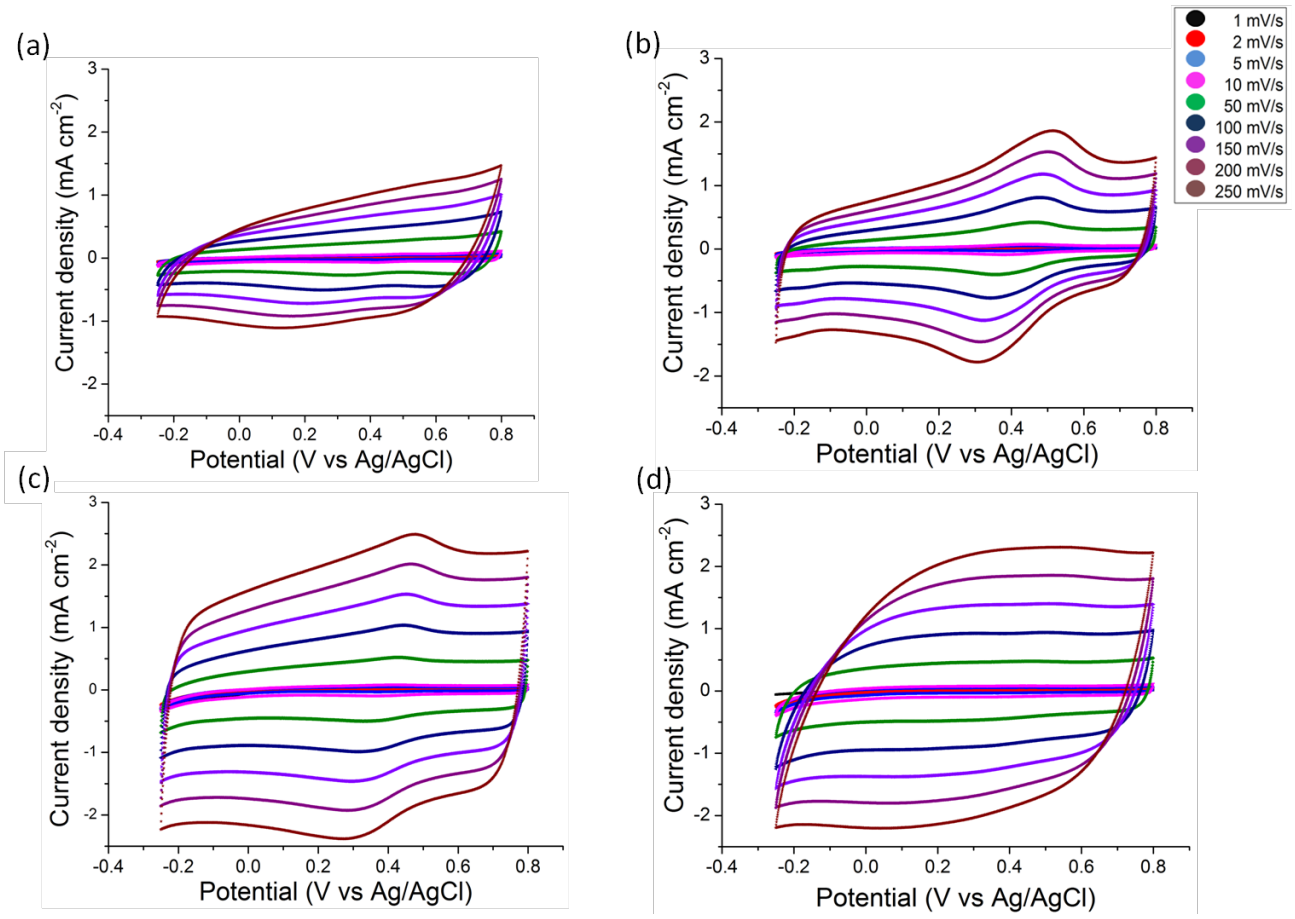


Figure 4.3: Cyclic voltammograms of the SWNT-based electrodes in 1 M H_2SO_4: (a) as-sprayed steam purified SWNT; (b) as-sprayed SWNT-COOH; (c) as-sprayed LbL SWNT-COOH/SWNT-NH_2; and (d) LbL SWNT-COOH/SWNT-NH_2 after vacuum and H_2 heat treatments.

at 0.5 and 0.32 V during charging and discharging respectively, due to the well-known pseudo-capacitive behaviour of -COOH groups in H_2SO_4 [9] [16], which has been quantified elsewhere [17]. The combination of additional pseudo-capacitance and the absence of inert surfactant increased the specific capacitance to 63 F g^{-1} and 13 mF cm^{-2} at 2 mV s^{-1}. It was the ability to incorporate SWNT-COOHs without surfactant that enabled surface redox reactions over a comparatively large surface area, and the resulting fast charge/discharge kinetics and high specific capacitance [15].

The voltammogram of the LbL SWNT-COOH/SWNT-NH_2 electrode in Fig. 4.3(c) exhibited less pronounced pseudo-capacitive peaks and more pronounced EDL capacitance. The potentials associated with the reduced but enduring pseudo-capacitive peaks again corresponded to the -COOH groups. There was no measurable electrochemical activity due to the NH_2 groups, confirmed by testing of SWNT-NH_2 only electrodes in 1 M H_2SO_4 (not shown). The more box-like shape of the voltammogram suggested less resistance, consistent with conductivity measurements in Table 4.1, and the specific capacitance increased further to 94 F g^{-1} and 19 mF cm^{-2} at 2 mV s^{-1}. Note that in this electrode, only half of the nanotubes (the SWNT-COOH type) can be expected to have contributed pseudo-capacitance in H_2SO_4. These capacitances compare favourably with those in MWNT-NH_3^+/MWNT-$COOH^-$ films of 104 F g^{-1} with 20 bilayers ($\sim$7 μm) and 81 F g^{-1} with 100 bilayers ($\sim$17 μm), but in a non-aqueous electrolyte of 1 M $LiPF_6$ in a mixture of ethylene carbonate and dimethyl carbonate [18]. In the present work, the capacitance in an aqueous electrolyte of 1 M H_2SO_4 with a more

limited voltage window, was 94 F g^{-1} for the LbL electrode and 151 F g^{-1} for the LbL electrode after heating. Table 4.1 showed that under otherwise constant manufacturing conditions, the sprayed LbL electrodes were the most dense, and therefore the relatively high volumetric capacitance most likely arose from a more continuous pathway for electron transport, and more of the electrode area per unit volume contributed in charge storage behaviour because more of the available surface was efficiently integrated into the function of the electrode.

Fig. 4.3(d) shows the voltammogram for the LbL electrode after heating in vacuum at 150 H_2 ^oC for 30 mins and then in H_2 at 300 ^oC for 2 hrs. There were no pseudocapacitive redox peaks, again consistent with the XPS data in Fig. 4.1 that showed removal of functional groups. The shape of the CV curve suggested the electrode became slightly more resistive and again was consistent with electrical conductivity measurements in Table 4.1. The specific capacitance of the vacuum and H_2-treated LbL electrode was 151 F g^{-1} and 30 mF cm^{-2} at 2 mV s^{-1}. Table 4.1 showed that the thickness of this electrode increased by 2.3 times after heating, with a larger electrode volume indicating a more porous structure, and a higher gravimetric but lower volumetric capacitance was obtained.

Fig. 4.4 shows a summary of the capacitance for purified SWNT, SWNT-COOH and LbL SWNT-COOH/SWNT-NH_2 electrodes before and after vacuum and H_2 heat treatments, over a wide range of scan rates. At all scan rates the gravimetric and aerial

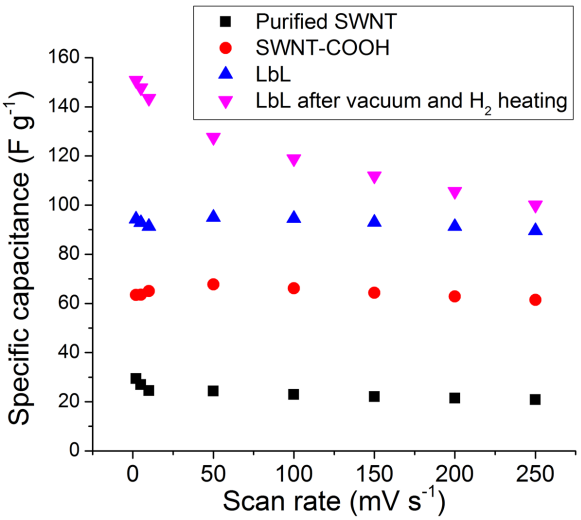


Figure 4.4: A summary of specific capacitance of the SWNT-based electrodes in 1 M H_2SO_4 over a wide range of scan rates.

capacitance followed the trend SWNT < SWNT-COOH < LbL SWNT-COOH/SWNT-NH_2 < LbL SWNT-COOH/SWNT-NH_2 + vacuum and H_2 treatments. In general, the capacitance increased with decreasing scan rate as electrolyte ions had more time to penetrate through the pores within the electrode structure [9] [19]. The more obvious increase in capacitance at lower scan rates for the LbL electrode after heating may be due to the additional contributions to charge storage provided in the hybrid structure of this electrode, as discussed in detail in the next section, which was most effective when ions had ample time to move through the hybrid structure.

4.3.4 Microstructure of SWNT-based electrodes

Fig. 4.5(a) shows a scanning electron micrograph (SEM) in plan view of a SWNT only electrode. The SWNTs formed a randomly interconnected network with interpenetrating meso-pores (diameter 2-50 nm). The SDBS surfactant was required to keep nanotubes well-dispersed, and SDBS residue at SWNT junctions was evident, undermining electrical conductivity and charge discharge kinetics, as shown in Table 4.1 and Fig. 4.3(a) respectively. Fig. 4.5(b) shows a similar plan view of the SWNT-COOH electrode, suggesting that the effective diameter of the SWNT-COOH had increased from <8 nm to ∼25 nm, with SWNT walls coated with -COOH containing groups. As-sprayed LbL electrodes appeared qualitatively similar in plan view, while Fig. 4.5(c) shows the LbL SWNT-COOH/SWNT-NH_2 electrode after heating in vacuum. The SWNT networks were decorated with very fine particulate and fibrous nanostructures, which may be related to the formation of amide groups, according to the XPS data in Fig. 4.2(d), and also reported in [8]. Fig. 4.5(d) shows an image of a cross-section of an LbL electrode and substrate snapped in liquid nitrogen, indicating that many of the SWNTs were oriented perpendicular to the substrate surface, and with an apparently strong physical contact to the underlying current collector, helping to lower interfacial resistance. Fig. 4.5(e) shows an SEM image in plan view of the LbL SWNT-COOH/SWNT-NH_2 electrode after heating in vacuum at 150 ^{o}C for 30 mins and in H_2 at 300 ^{o}C for 2 hrs, showing for the first time the presence of C-rich "nanoplates" in the SWNT-based network. For comparison, only agglomerates of carbonaceous material

but no carbon nanoplates of this type were observed in the SWNT-COOH electrode after the same process conditions.

In order to probe microstructural changes further, the LbL electrodes after vacuum and H_2 heat treatments were investigated by transmission electron microscopy (TEM). Fig. 4.6(a) is a TEM image of a C-rich nanoplate, showing that the nanoplate consisted of a few thin C-rich sheets stacked together in different orientations. Fig. 4.6(b) is a magnified TEM image of the edge of the nanoplate in Fig. 4.6(a), suggestive of few-layer graphene.

Fig. 4.7(a) shows a diffraction pattern taken from the edge of a nanoplate in Fig. 4.6(a), showing high crystallinity (diffraction spots) and clear sixfold symmetry, typical for graphene [20]. A plot of diffraction intensity along the superimposed line in Fig. 4.7(a) passing through (1-210)-(0-110)-(-1010)-(-2110) diffraction spots is shown in Fig. 4.7(b), indicating that the intensity of outer (1-210) and (-2110) peaks was stronger than those of the inner (0-110) and (-1010) peaks. According to [21], this confirms multi-layer graphene (for multilayers with Bernal (AB) stacking, computational studies have also shown that the intensity ratio $I_{\{1100\}}/I_{\{2110\}} < 1$, as found here, demonstrating that AB stacking is predominant, whereas for monolayers, $I_{\{1100\}}/I_{\{2110\}} > 1$ [22]).

Fig. 4.8(a) shows a high-angle annular dark field (HAADF) image acquired in the scan-

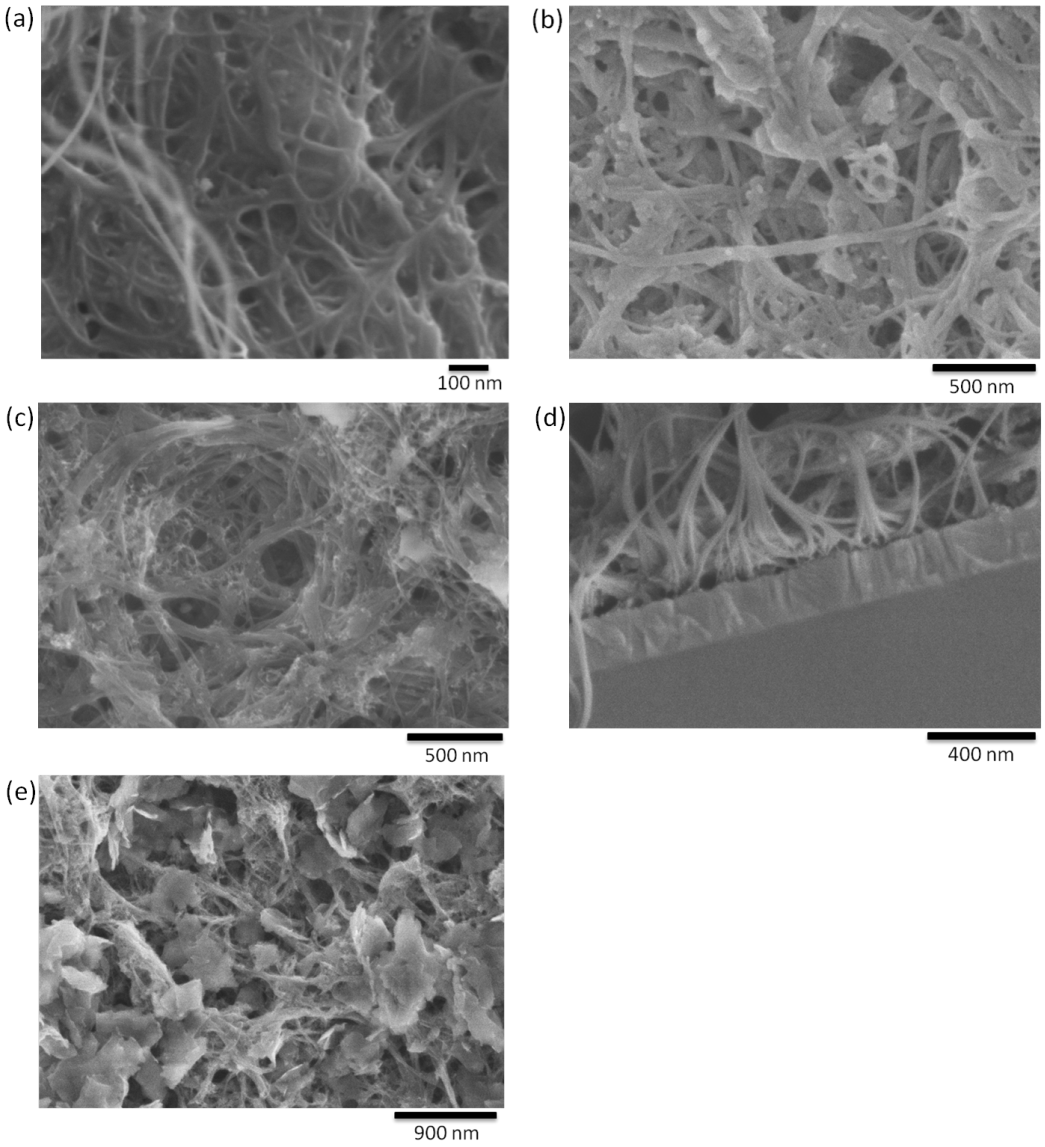


Figure 4.5: Scanning electron micrographs of the SWNT-based electrodes: (a) plan view of the as-sprayed SWNT network; (b) plan view of the as-sprayed SWNT-COOH network; (c) plan view of the LbL SWNT-COOH/SWNT-NH_2 electrode after heating in vacuum at 150 ^{o}C for 30 min; (d) cross-section view of the interface between the as-sprayed LbL SWNT-COOH/SWNT-NH_2 electrode and the substrate; and (e) plan view of the LbL electrode after heating in vacuum at 150 ^{o}C for 30 mins and in H_2 at 300 ^{o}C for 2 hrs.

ning transmission electron microscope (STEM), often used for the study of graphene [23]. HAADF imaging is a useful tool for the characterisation of multilayer graphene

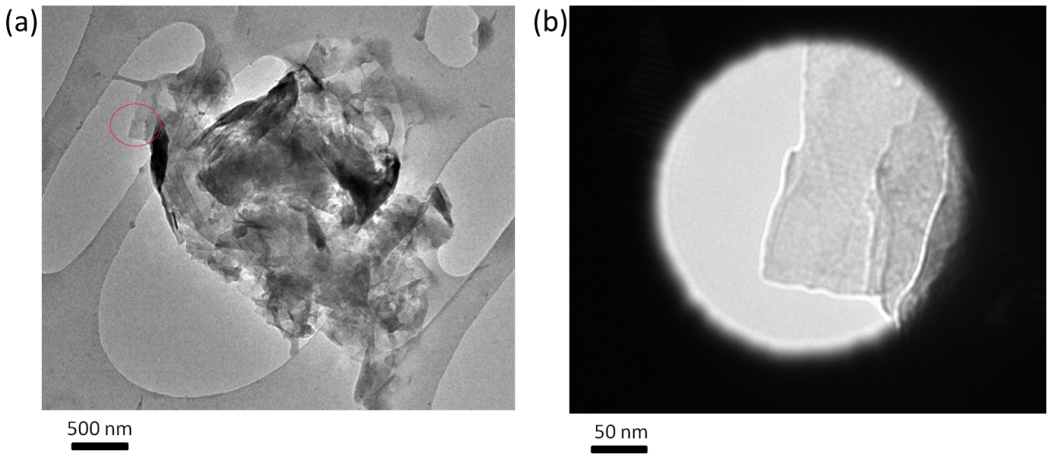


Figure 4.6: TEM images: (a) nanoplate from the LbL electrode after vacuum and H_2 heating; (b) the edge of the nanoplate, where a selected area aperture has been inserted, diffraction pattern was taken.

sheets since the intensity of the high-angle scattered electrons varies monotonically with specimen thickness, even down to the atomic level [24]. The HAADF image intensity of collected high-angle scattered electrons versus electron probe position across the sample can be used to study the variation in number of graphene layers present within an area [23]. Fig. 4.8(a) shows a HAADF image from the LbL electrode after both vacuum and H_2 heating, with a superimposed region of interest, from which the image intensity was measured from A to B, as shown in Fig. 4.8(b). Although inevitably noisy due to the low detected signal in this mode of operation, the intensity varied with distance from A to B in discrete steps with intensities of $\sim 8 \times 10^5$, $\sim 6.8 \times 10^5$ and $\sim 5.5 \times 10^5$ (arbitrary units). Due to the approximately constant increment between these average values we may infer the specimen to locally consist of tri-, bi- and monolayer graphene.

Since graphene sheets were only seen in the LbL electrodes, it is postulated that the

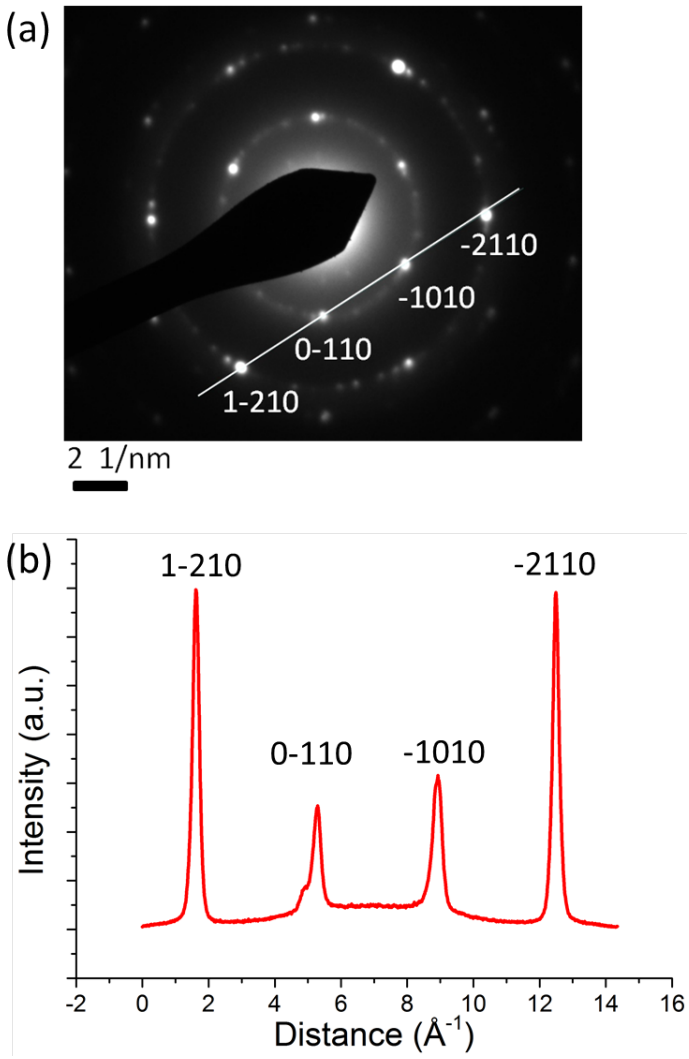


Figure 4.7: (a) Electron diffraction pattern of multi-layer graphene with the peaks labelled by Miller-Bravais indices; (b) diffracted intensity taken along the 1-210 to -2110 axis for the pattern shown in (a).

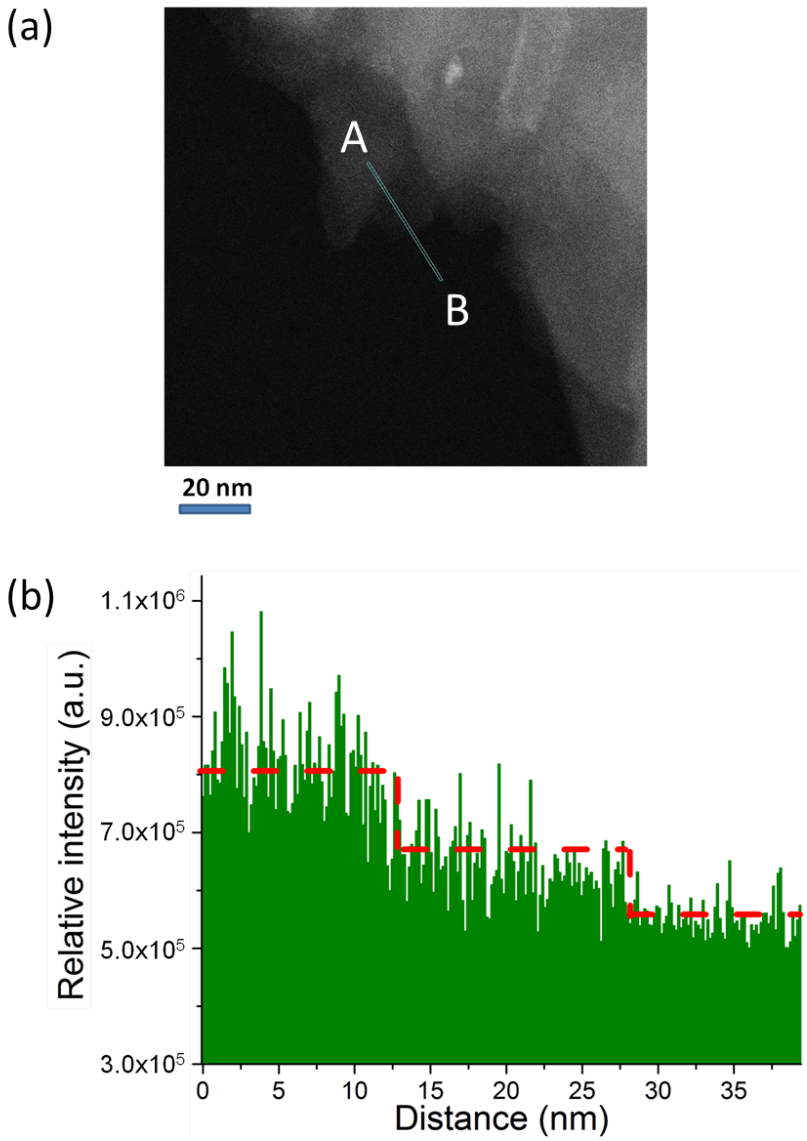


Figure 4.8: (a) High-angle annular dark-field (HAADF) image of the LbL electrode after vacuum and H_2 heating, where a region of interest was drawn to measure intensities over an area (the width of the rectangle was 10 pixels); and (b) an example of intensity histograms obtained from A to B, 20 intensity profiles were obtained and the average calculated.

several chemical synthesis steps and chemical interactions between -COOH and -NH_2 groups made the SWNTs particularly susceptible to "unzipping" in a H_2 environment at 300 ^{o}C. The resulting graphene flakes then stacked together to form the observed multi-layer graphene, and eventually thicker more agglomerated nanoplates.

The unzipping of MWNTs along their axes to unroll to graphene sheets was reported in 2009 [25] [26], and one of the now relatively well-known methods of MWNT unzipping involves treating MWNTs with concentrated sulphuric acid (12 hrs) followed by treatment with 500wt% potassium permanganate (an oxidising agent) for 1 hr at room temperature, and 1 hr at 55-70 ^{o}C [25] [26]. The same unzipping process was achieved in SWNTs, but their subsequent disentanglement was more difficult [25]. Similarly to the results here, after chemical treatment, only a relatively low temperature was needed to unzip the SWNT tubes, suggesting that the nucleation of defects in the SWNT walls was the rate-determining step. Both unzipped SWNTs and MWNTs (also called nanoribbons) have been suggested to be relatively poor conductors, because the resulting edge structures hold O-containing groups that disrupt charge flow [25] [27]. However, the oxidised edges can be reduced using H_2 at 350 ^{o}C for 6 hrs [25] [26]. Computer simulations have also shown the viability of breaking C-C bonds in SWNT walls through the formation of C-H bonds in a H_2 environment, leading to unzipping of SWNTs [28].

In the current work, the LbL SWNTs were subject to several stages of comparatively aggressive treatment: steam purificaton, treatment with concentrated acids (HCl 6 hrs

and then HNO_3 10 hrs), with some treatments also undergoing amine functionalisation with $SOCl_2$ at 70 ^oC for 12 hrs and then with $NH_2(CH_2)_2NH_2$ at 70 ^oC for 24 hrs, as well as ultrasonication to help prepare the suspensions for spraying. The -NH_2 and -COOH containing SWNTs then underwent chemical reaction, vacuum heat treatment at 150 ^oC and H_2 treatment at 300 ^oC. In general, the SWNTs were robust under these process conditions, but it was either the NH_2 functionalisation or the chemical reaction between -COOH and -NH_2 that was the decisive step in introducing mobile defects that then led to unzipping in the presence of H_2.

The capacitance of the LbL electrode after vacuum and H_2 heating was 151 F g^{-1} at 2 mV s^{-1}, with the "hybrid" structure of SWNT/multi-layer graphene increasing specific capacitance significantly compared with the "pure" SWNT network. Because the double-layer capacitance for the edge orientation is an order of magnitude higher than that of the basal layer [14] [29], and high capacitances were obtained here, it may be speculated that the multi-layer graphene sheets were intertwined in the SWNT scaffold in such a way that they helped to maintain the exposure of edge planes to the electrolyte [30]. A schematic representation of the LbL electrode structure both as-sprayed and after vacuum and H_2 treatments is shown in Fig. 4.9. Detailed electrochemical impedance spectroscopy may be a possibility of further investigating the change in resistance and hybrophobicity of the electrodes [31].

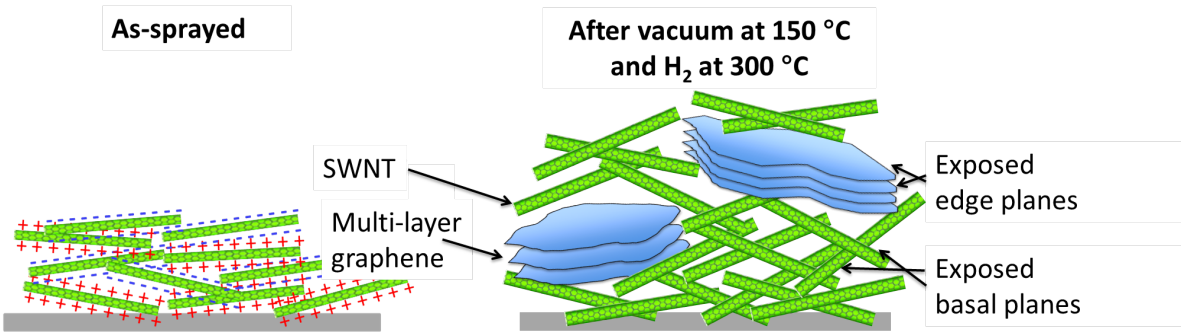


Figure 4.9: Schematic of the as-sprayed LbL electrode, and the hybrid structure of SWNT/multi-layer graphene sheets after post-spray treatments.

4.4 Conclusions

LbL spray deposition has been used to fabricate SWNT-COOH/SWNT-NH_2 electrodes. Density measurements showed a 65% increase for the LbL electrode over other SWNT electrodes. The electrical conductivity of the LbL SWNT-COOH/SWNT-NH_2 electrode was 14.5 S cm^{-1}, and amongst the highest for the equivalent CNT-based electrodes. The LbL SWNT-COOH/SWNT-NH_2 electrodes exhibited a pronounced EDL capacitance of 94 F g^{-1}, compared with 29 F g^{-1} for pure SWNT electrodes and 63 F g^{-1} for SWNT-COOH electrodes at 2 mV s^{-1}, which was due to their high conductivity and compact structure, facilitating faster and more efficient charging/discharging kinetics and more active area per unit volume in a 1 M H_2SO_4 electrolyte.

Heating in vacuum at 150 ^oC for 30 mins stimulated interaction between carboxylic and amine groups to form amide bonds within the LbL electrodes; subsequent heating

in a H_2 atmosphere at 300 ^oC for 2 hrs removed the functional groups and unzipped some SWNTs to form multi-layer graphene sheets. These heat treatments increased the LbL specific capacitance to 151 F g^{-1} at 2 mV s^{-1}. The hybrid, 3D scaffold structure formed by 1D SWNTs and 2D multi-layer graphene sheets offered a combination of basal plane (exposed by the SWNTs) and edge plane (exposed by the multi-layer graphene sheets) carbon, and enhanced the overall capacitance. The LbL electrode after H_2 heat treatment presented essentially pure EDL charge storage with no pseudocapacitive contribution, and is amongst the highest reported for EDL capacitances of SWNT-based electrodes.

Bibliography

[1] P. J. Hall, M. Mirzaeian, S. I. Fletcher, F. B. Sillars, A. J. R. Rennie, G. O. Shitta-Bey, G. Wilson, A. Cruden, and R. Carter, "Energy storage in electrochemical capacitors: designing functional materials to improve performance," *Energy & Environmental Science*, vol. 3, no. 9, pp. 1238–1251, 2010.

[2] Y. Zhang, H. Feng, X. B. Wu, L. Z. Wang, A. Q. Zhang, T. C. Xia, H. C. Dong, X. F. Li, and L. S. Zhang, "Progress of electrochemical capacitor electrode materials: A review," *International Journal of Hydrogen Energy*, vol. 34, no. 11, pp. 4889–4899, 2009.

[3] G. Lota, K. Fic, and E. Frackowiak, "Carbon nanotubes and their composites in electrochemical applications," *Energy Environmental Science*, vol. 4, pp. 1592–1605, 2011.

[4] X. Zhao, B. M. Sanchez, P. J. Dobson, and P. S. Grant, "The role of nanomaterials in redox-based supercapacitors for next generation energy storage devices," *Nanoscale*, vol. 3, no. 3, pp. 839–855, 2011.

[5] B. E. Conway, *Electrochemical Supercapacitors, Scientific Fundamentals and Technological Applications*. Kluwer Academic / Plenum Publishers, 1999.

[6] V. V. N. Obreja, "On the performance of supercapacitors with electrodes based on carbon nanotubes and carbon activated material - a review," *Physica E-Low-Dimensional Systems & Nanostructures*, vol. 40, no. 7, pp. 2596–2605, 2008.

[7] P. Simon and Y. Gogotsi, "Materials for electrochemical capacitors," *Nature Materials*, vol. 7, no. 11, pp. 845–854, 2008.

[8] S. W. Lee, B. S. Kim, S. Chen, Y. Shao-Horn, and P. T. Hammond, "Layer-by-layer assembly of all carbon nanotube ultrathin films for electrochemical applications," *Journal of the American Chemical Society*, vol. 131, no. 2, pp. 671–679, 2009.

[9] X. Zhao, B. T. T. Chu, B. Ballesteros, W. Wang, C. Johnston, J. M. Sykes, and P. S. Grant, "Spray deposition of steam treated and functionalized single-walled and multi-walled carbon nanotube films for supercapacitors," *Nanotechnology*, vol. 20, no. 6, 2009.

[10] D. Briggs and J. T. Grant, eds., *Surface analysis by Auger and x-ray photoelectron spectroscopy*. IM Publications, 2003.

[11] Z. Niu, J. Du, X. Cao, Y. Sun, W. Zhou, H. H. Hng, J. Ma, X. Chen, and S. Xie, "Electrophoretic build-up of alternatively multilayered films and micropatterns based on graphene sheets and nanoparticles and their applications in flexible supercapacitors," *Small*, vol. 8 (20), pp. 3201–3208, 2012.

[12] Y. Wang, Z. Shi, Y. Huang, Y. Ma, C. Wang, M. Chen, and Y. Chen, "Supercapacitor devices based on graphene materials," *The Journal of Physical Chemistry C*, vol. 113, pp. 13103–13107, 2009.

[13] Y. Zhu, S. Murali, M. D. Stoller, K. J. Ganesh, W. Cai, P. J. Ferreira, A. Pirkle, R. M. Wallace, K. A. Cychosz, M. Thommes, D. Su, E. A. Stach, and R. S. Ruoff, "Carbon-based supercapacitors produced by activation of graphene," *Science*, vol. 332 (6037), pp. 1537–1541, 2011.

[14] F. Beguin and E. Frackowiak, eds., *Carbons for electrochemical energy storage and conversion systems*. CRC Press, 2010.

[15] S. W. Lee, N. Yabuuchi, B. M. Gallant, S. Chen, B. S. Kim, P. T. Hammond, and Y. Shao-Horn, "High-power lithium batteries from functionalized carbon-nanotube electrodes," *Nature Nanotechnology*, vol. 5, no. 7, pp. 531–537, 2010. Times Cited: 3.

[16] H. Pan, C. K. Poh, Y. Feng, and J. Lin, "Supercapacitor electrodes from tubes-in-tube carbon nanostructures," *Chemical Materials*, vol. 19, pp. 6120–6125, 2007.

[17] J. Wang, J. Polleux, J. Lim, and B. Dunn, "Pseudocapacitive contributions to electrochemical energy storage in TiO_2 (anatase) nanoparticles," *Journal of Physical Chemistry C*, vol. 111, pp. 14925–14931, 2007.

[18] S. Y. Kim, J. Hong, R. Kavian, S. W. Lee, M. N. Hyder, Y. Shao Horn, and P. T. Hammond, "Rapid fabrication of thick spray-layer-by-layer carbon nanotube

electrodes for high power and energy devices," *Energy and Environmental Science*, vol. 6, pp. 888–897, 2013.

[19] S. R. C. Vivekchand, C. S. R. Rout, K. S. Subrahmanyam, A. Govindaraj, and C. S. R. Rao, "Graphene-based electrochemical supercapacitors," *Journal of the Chemical Society*, vol. 120, pp. 9–13, 2008.

[20] J. C. Meyer, A. K. Geim, M. I. Katsnelson, K. S. Novoselov, T. J. Booth, and S. Roth, "The structure of suspended graphene sheets," *Nature*, vol. 446, no. 7131, pp. 60–63, 2007.

[21] Y. Hernandez, V. Nicolosi, M. Lotya, F. M. Blighe, Z. Y. Sun, S. De, I. T. McGovern, B. Holland, M. Byrne, Y. K. Gun'ko, J. J. Boland, P. Niraj, G. Duesberg, S. Krishnamurthy, R. Goodhue, J. Hutchison, V. Scardaci, A. C. Ferrari, and J. N. Coleman, "High-yield production of graphene by liquid-phase exfoliation of graphite," *Nature Nanotechnology*, vol. 3, no. 9, pp. 563–568, 2008.

[22] S. Horiuchi, T. Gotou, M. Fuijwara, R. Sotoaka, M. Hirata, K. Kimoto, T. Asaka, T. Yokosawa, Y. Matsui, K. Watanabe, and M. Sekita, "Carbon nanofilm with a new structure and property," *Japanese Journal of Applied Physics Part 2-Letters*, vol. 42, no. 9AB, pp. L1073–L1076, 2003.

[23] M. H. Gass, U. Bangert, A. L. Bleloch, P. Wang, R. R. Nair, and A. K. Geim, "Free-standing graphene at atomic resolution," *Nature nanotechnology*, vol. 3, pp. 676–681, 2008.

[24] Z. Li, N. Young, M. Di Vece, S. Palomba, R. Palmer, A. L. Bleloch, B. Curley, R. Johnston, J. Jiang, and J. Yuan, "Three-dimensional atomic-scale structure of size-selected gold nanoclusters," *Nature*, vol. 451, pp. 46–48, 2008.

[25] D. V. Kosynkin, A. L. Higginbotham, A. Sinitskii, J. R. Lomeda, A. Dimiev, B. K. Price, and J. M. Tour, "Longitudinal unzipping of carbon nanotubes to form graphene nanoribbons," *Nature*, vol. 458, pp. 872–876, 2009.

[26] L. L. Zhang and X. S. Zhao, "Carbon-based materials as supercapacitor electrodes," *Chemical Society Reviews*, vol. 38, pp. 2520–2531, 2009.

[27] M. Terrones, "Nanotubes unzipped," *Nature*, vol. 458, pp. 845–846, 2009.

[28] G. Lu, "Hydrogen-induced unzipping of single-walled carbon nanotubes," *Physcial Review B*, vol. 68, pp. 205416–205421, 2003.

[29] A. Pandolfo, "Carbon properties and their role in supercapacitors," *Journal of Power Sources*, vol. 157, pp. 11–27, 2006.

[30] K. M. Metz, P. E. Colavita, K.-Y. Tse, and R. J. Hamers, "Nanotextured gold coatings on carbon nanofiber scaffolds as ultrahigh surface-area electrodes," *Journal of Power Sources*, vol. 198, pp. 393–401, 2012.

[31] X. Li, J. Rong, and B. Wei, "Electrochemical behavior of single-walled carbon nanotube supercapacitors under compressive stress," *ACS Nano*, vol. 4, pp. 6039–6049, 2010.

Chapter 5

Spray processing of multi-wall carbon nanotube-based solid-state supercapacitors

5.1 Introduction

Chapter 4 described that selecting a suitable spray approach relating to specific materials can give a degree of control over the fabricated electrode microstructure and the corresponding performance. This chapter describes the fabrication and characterisation of multi-wall carbon nanotube (MWNT)-based solid-state supercapacitor full cells by the spray processing technique.

As shown in Chapter 2, the configuration of a conventional supercapacitor is an ion-

permeable, electrically insulating separator sandwiched between two very high surface area electrodes (usually based on activated carbon) flooded with a liquid electrolyte and sealed in a package that is required to retain the electrolyte (preventing leakage and possible combustion) and to provide mechanical integrity. Although liquid electrolytes generally provide a high ion (usually Li^+) mobility, the rigid packaging severely restricts the development of thin and flexible energy storage devices, and the leakage of harmful electrolytes is one of the main concerns for portable and wearable electronics. There are therefore continuing efforts to replace these liquid electrolytes with for example, safer solid-state electrolytes especially for flexible or conformal battery and supercapacitor designs [1].

Chapter 2 reviewed the component materials for the current solid-state supercapacitors and their performances. The majority use a gel electrolyte of polyvinyl alcohol (PVA) mixed with a strong acid such as H_2SO_4 and involve hot pressing of the electrodes onto the electrolyte gel to promote infiltration and to form a simple thin supercapacitor cell. However, this approach to manufacture is hard to regulate and difficult to avoid electrical shorts across the gel. Although some encouraging capacitances have been achieved for the solid-state supercapacitors with the PVA-H_2SO_4 gel electrolyte, the power densities were usually low due to the common problem of slow ion mobilities within the solid-state cells e.g 332 F g^{-1} at 1 A g^{-1} was reported for a solid-state supercapacitor with polyaniline (PANI)/carbon nanotube (CNT) electrodes but at a low power density of 2.1 kW kg^{-1} [2].

In this chapter, a thin (230 μm) solid-state supercapacitor was fabricated by spraying aqueous suspensions of MWNTs in 0.5 M H_2SO_4 directly onto both sides of a Nafion proton conducting membrane, which was heated at 100 °C throughout deposition to evaporate water as the meso-porous MWNT-based electrodes formed. The spray processing procedure did not require any hot pressing and had a good quality control over fabrication with an almost 0% short circuits failure rate. Fig. 5.1(a) shows a flexible membrane covered with the sprayed MWNT-based electrode on both sides and Fig. 5.1(b) is a schematic diagram of the fabricated solid-state supercapacitor full cell including Cu foil current collectors which were added onto either electrode by gentle manual pressing. Then to increase H^+ mobility, Nafion polymer short chain ionomer was added into the aqueous suspensions during spraying to create a hybrid porous electrode, comprising MWNTs coated with ionomer [3, 4, 5]. Fig. 5.1(c) shows how three 4.5 cm x 4 cm x 230 μm cells were stacked and connected in series to operate at 3 V and 1 and 2 A g^{-1} and produced a power density of 8.9 kW kg^{-1} at 1 A g^{-1} and 9.4 kW kg^{-1} at 2 A g^{-1}.

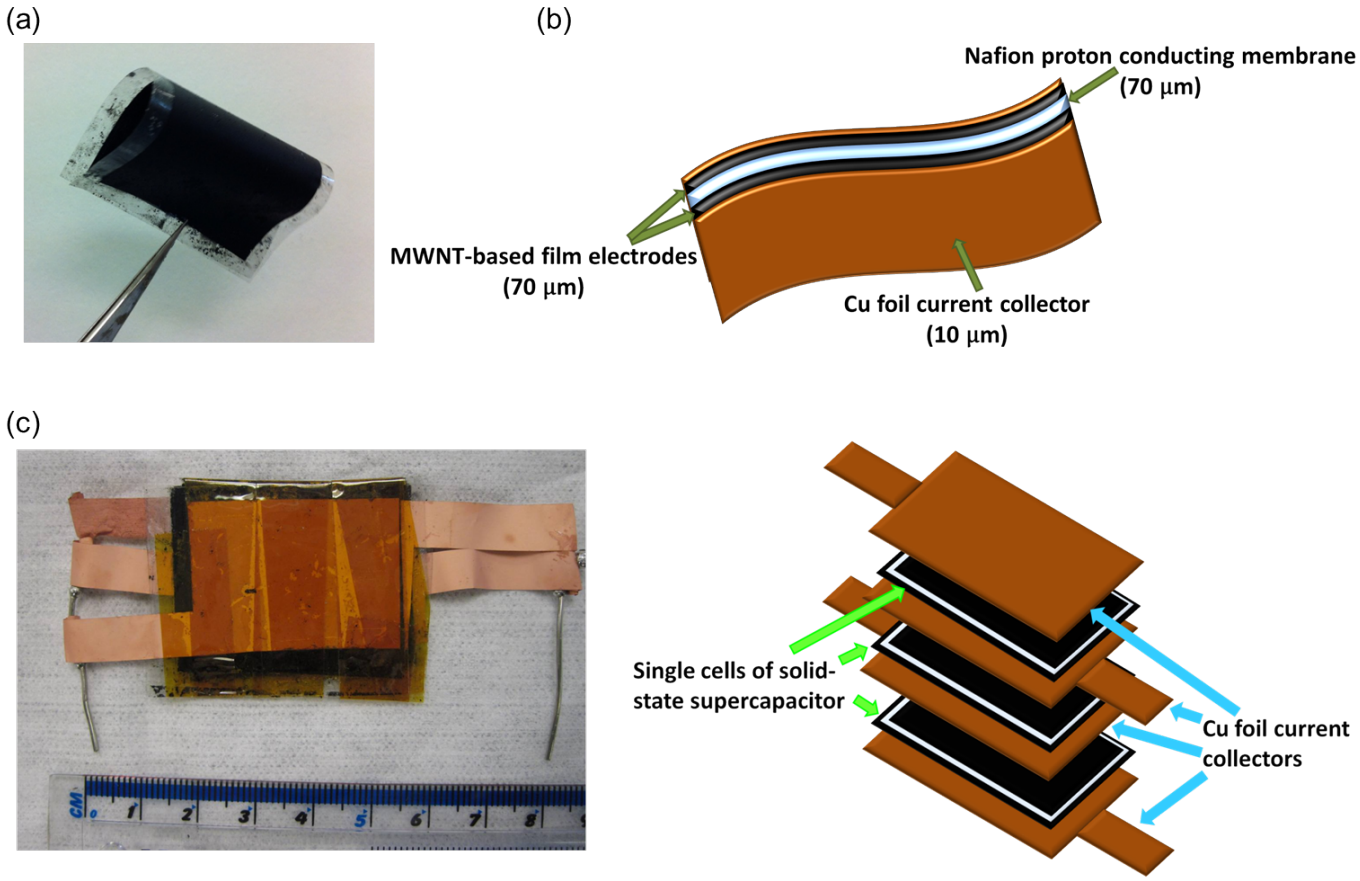


Figure 5.1: (a) A flexible Nafion membrane covered with spray deposited MWNT-based electrodes on both sides; (b) a schematic diagram of the fabricated solid-state supercapacitor full cell including Cu foil current collectors; and (c) a fabricated simple "stack" of three solid-state supercapacitor cells and the corresponding schematic diagram.

5.2 Materials and methods

5.2.1 Fabrication of solid-state supercapacitors by spray deposition

The main spray deposition configuration has already been described in Chapter 3, and this section will show the specific fabrication procedure of symmetrical solid-state supercapacitors with MWNT-only and MWNT/ionomer hybrid electrodes.

Membranes (Nafion, 70 μm thickness, Du Pont) were pre-treated by immersing in 1 M H_2SO_4 at 60 °C for 30 min. Nafion®, produced by Du Pont, is a functionalised polymer bearing negatively charged perfluorosulfonate (-SO_2F-) groups in the main structure, promoting proton hopping through -SO_3-H^+- groups [6] [7]. Two MWNT-based suspensions were prepared: firstly, as supplied MWNTs (Bayer MaterialScience) dispersed in 0.5 M H_2SO_4 aqueous solution with 0.1 wt% sodium dodecylbenzenesulfonate (SDBS, Sigma-Aldrich) surfactant; and secondly, MWNTs with 50 wt% Nafion ionomer (Sigma-Aldrich) again dispersed in 0.5 M H_2SO_4 aqueous solution. The ionomer readily provided suspension stability without the need for any additional surfactant [8]. Both of the suspensions became homogeneous after ultrasonicating (600 W, 20 kHz) for 15 mins. The suspensions were then sprayed directly onto both sides of the Nafion proton conducting membrane, which was heated at 100 °C throughout deposition. The membrane with one side covered with the sprayed MWNT-based thin film electrode was

then flipped and sprayed on the other side using the identical procedure. The thickness of each electrode was controlled by the spraying time to be $\sim$ 70 μm. Cu foil current collectors of $\sim$10 μm in thickness were then added on the two sides by gentle manual pressing to create a symmetrical supercapacitor cell. Two and three identical solid-state supercapacitors were connected in series through Cu foils to make a stack.

5.2.2 Characterisation

Cyclic voltammetry (CV) was performed over a range of scan rates from 1 to 300 mV s^{-1}, galvanostatic charge/discharge was measured at 1-3 V with current densities of 1-2 A g^{-1}, and electrochemical impedance spectroscopy (EIS) was performed from 0.05 to 10^6 Hz using an AC voltage of 5 mV rms. In order to compare the performance of the solid-state supercapacitors and the equivalent electrode performance in a conventional liquid 1 M H_2SO_4 electrolyte, electrochemical characterisation of a single sprayed electrode was also conducted using a three-electrode configuration for the MWNT-based film on a stainless steel substrate (2 cm x 1 cm) as the working electrode, and with Ag/AgCl and Pt wire as the reference and counter electrodes respectively.

5.3 Results and discussion

5.3.1 MWNT-only electrode in an aqueous electrolyte

Fig. 5.2(a) shows the cyclic voltammograms of an as-sprayed MWNT + 0.1 wt% SDBS surfactant electrode which was fabricated by spraying MWNTs in a 0.5 M dilute version of H_2SO_4 electrolyte, and then tested in aqueous 1 M H_2SO_4. The voltammograms had a parallelogram shape, indicating the MWNT electrode exhibited electric double layer (EDL) behaviour due to ion surface adsorption, also agreeing with the corresponding galvanostatic charge/discharge "sawtooth" curves in Fig. 5.2(b). The specific capacitance was estimated as 130 F g^{-1} (37 mF cm^{-2}) at 2 mV s^{-1} and 86 F g^{-1} (24 mF cm^{-2}) at 150 mV s^{-1} from the cyclic voltammograms, and 92 F g^{-1} (26 mF cm^{-2}) at 1 A g^{-1} from the discharge curve, giving an energy density of 12 Wh kg^{-1} and a maximum power density of 3.4 kW kg^{-1}. The EDL capacitance of non-functionalised CNTs with no pseudo-capacitance generally lies in the range 15-120 F g^{-1} [9], and so the capacitance achieved after spraying in 0.5 M H_2SO_4 was at the top end of those reported for non-functionalised MWNTs.

Figs. 5.2(c) and (d) show the EIS Nyquist plots for the MWNT-only electrodes fabricated by spraying in DI water and in 0.5 M H_2SO_4, and the arrow direction in all Nyquist plots in this chapter indicates an increasing frequency trend. Figs. 5.2 (c) and (d) show that at high frequency, the intersection of the best-fit curve to the data with the real axis (indicative of the equivalent series resistance (ESR) of the electrolyte, in-

ternal electrode and current collector [10]) was 5 Ω for spraying in DI water and 1 Ω for spraying in 0.5 M H_2SO_4, and the charge transfer resistance (the semi-circle diameter) was ∼35 Ω for the DI water but only 7 Ω for 0.5 M H_2SO_4. The high capacitance and low resistance may be contributed by spraying and forming the MWNT electrodes incrementally in the presence of a 0.5 M dilute version of the H_2SO_4 electrolyte, which ensured the H^+ ions fed into all parts of the interior of the electrode to promote electrolyte wetting and ion adsorption, and - as shown later - was an insight not previously remarked in the group that may be even more important for solid-state supercapacitors where H^+ mobility in the interior of electrode can expected to be limited.

5.3.2 Solid-state supercapacitor with MWNT-only electrodes

In order to establish baseline behaviour against which the subsequent effect of ionomer additions could be assessed, a solid-state supercapacitor with MWNT-only electrodes was firstly studied.

Fig. 5.3(a) shows the cyclic voltammograms of a double-side sprayed full cell solid-state supercapacitor with the membrane sandwiched between the two MWNT + 0.1 wt% SDBS electrodes, showing highly resistive character with restricted ion mobility during charging and discharging, and is illustrative of typical problems for solid-state supercapacitors [9]. Fig. 5.3(b) is the same cyclic voltammograms normalised by the square root of scan rate, which can be used to better enable the resolution of low scan

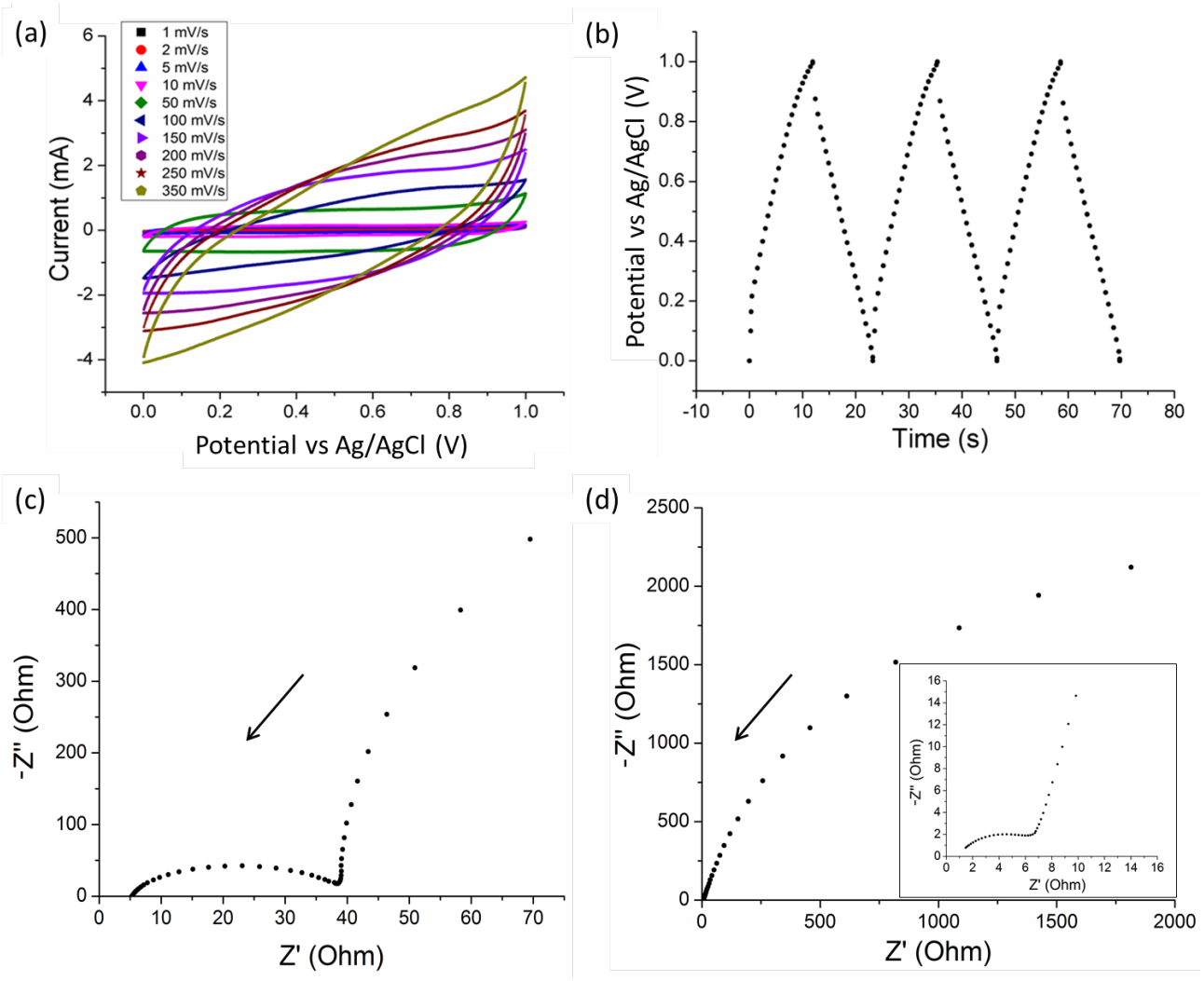


Figure 5.2: (a) Cyclic voltammograms for a MWNT-only electrode fabricated by spraying in 0.5 M H_2SO_4; (b) the corresponding DC galvanostatic charge/discharge curves at 1 A g^{-1}; (c) Nyquist plot for the MWNT-only electrode fabricated by spraying in DI water; and (d) Nyquist plot for the MWNT-only electrode fabricated by spraying in 0.5 M H_2SO_4, all tested in 1 M H_2SO_4 in a three-electrode configuration.

rate behaviour when a wide range of scan rates is studied, and shows that the current increased asymmetrically about zero current at very slow scan rates of 1 and 2 mV s^{-1}, probably due to electron percolation through the Nafion membrane due to a small fraction of MWNTs that were drawn into the membrane porous structure. Since there

was no comparable ion mobility in the reverse direction of the electrons, the voltammograms became asymmetrical.

The voltammogram shapes indicated little EDL or pseudo-capacitive behaviour giving a specific capacitance of 57 F g^{-1} (16 mF cm^{-2}) per electrode at 2 mV s^{-1} and 44 F g^{-1} (12 mF cm^{-2}) at 150 mV s^{-1}, compared with 130 F g^{-1} at 2 mV s^{-1} and 86 F g^{-1} at 150 mV s^{-1} for the same electrode showing EDL behaviour in aqueous 1 M H_2SO_4 in Section 5.3.1.

In order to check for any reaction with the Cu current collector, both carbon coated and uncoated Cu current collectors were studied under identical conditions and no difference or resolvable reactions were measured. The energy density of the solid-state supercapacitor was 6.1 Wh kg^{-1}, and the maximum power density was 1.1 kW kg^{-1}, in the lower range of 0.01-10 kW kg^{-1} for commercial supercapacitor power densities with liquid electrolytes [11] [12].

Fig. 5.3(c) shows the corresponding DC galvanostatic charge/discharge curves at a potential range of 1 V at 1 A g^{-1} with a similar specific capacitance estimated from the discharge curves of 47 F g^{-1} (13 mF cm^{-2}). The IR drop associated with internal resistance of the supercapacitor at the beginning of each charge and discharge cycle was $\sim$0.14 V, compared with $\sim$0.11 V for the equivalent aqueous electrolyte in Fig. 5.2(b).

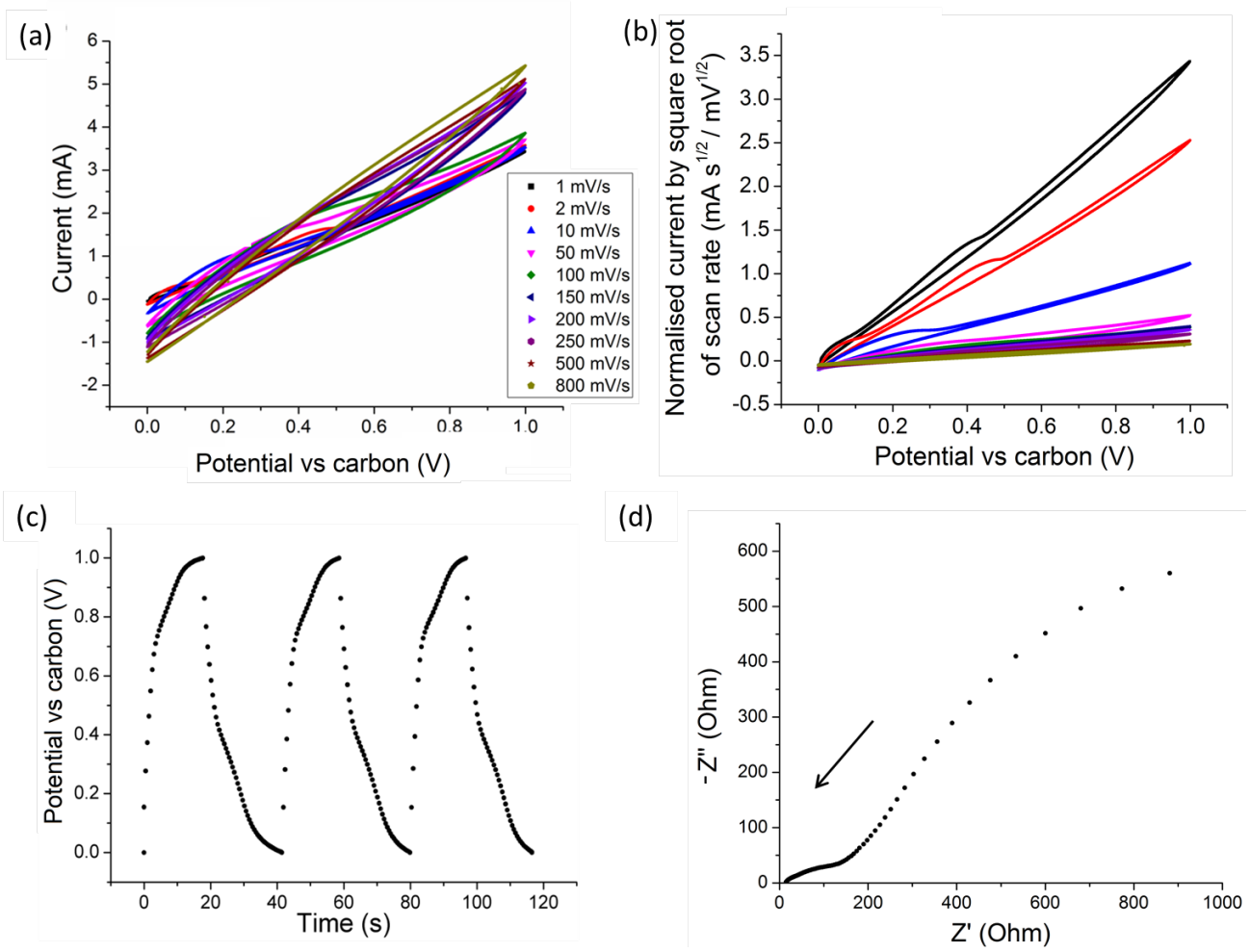


Figure 5.3: (a) Cyclic voltammograms of a full cell membrane-based solid-state supercapacitor with MWNT-only electrodes; (b) the same cyclic voltammograms normalised by the square root of the scan rate; (c) DC galvanostatic charge/discharge curves of the same solid-state supercapacitor at 1 A g^{-1}; and (d) the complementary Nyquist impedance plot.

Fig. 5.3(d) is the corresponding Nyquist plot showing that the ESR was estimated at ∼19 Ω and much higher than 1 Ω for the equivalent liquid-based electrolyte in Fig. 5.2(d) and 0.75 Ω for MWNTs electrophoretically deposited onto Ni foils in a 6 M KOH electrolyte [13].

In summary, spray processing conveniently produced thin (∼70 μm thick for each electrode) and compact solid-state supercapacitors but performance was undermined by a limited EDL response because of a combination of high resistance and limited ionic mobility when compared with the aqueous electrolyte equivalents.

5.3.3 Solid-state supercapacitor with MWNT/ionomer electrodes

Fig. 5.4(a) shows a scanning electron micrograph of the as-sprayed MWNT/ionomer electrode, showing an interconnected meso-porous MWNT scaffold with some ionomer coating. Fig. 5.4(b) is a transmission electron micrograph of the dried MWNTs co-sprayed with the ionomer showing more clearly how the ionomer coated the majority of the length of the MWNTs, with a thickness approximately comparable with the MWNT diameter of ∼6 nm.

Fig. 5.5(a) is the cyclic voltammograms of a full cell solid-state supercapacitor with MWNT/ionomer hybrid electrodes, showing that the voltammograms were more box-like than the MWNT + 0.1 wt% SDBS based electrodes in Fig. 5.3(a), with current now increasing much more readily on the potential sweep reversal at all sweep rates and the overall behaviour was of an EDL capacitor. Fig. 5.5(b) shows the corresponding normalised voltammograms, where the current response was now more symmetrical. The

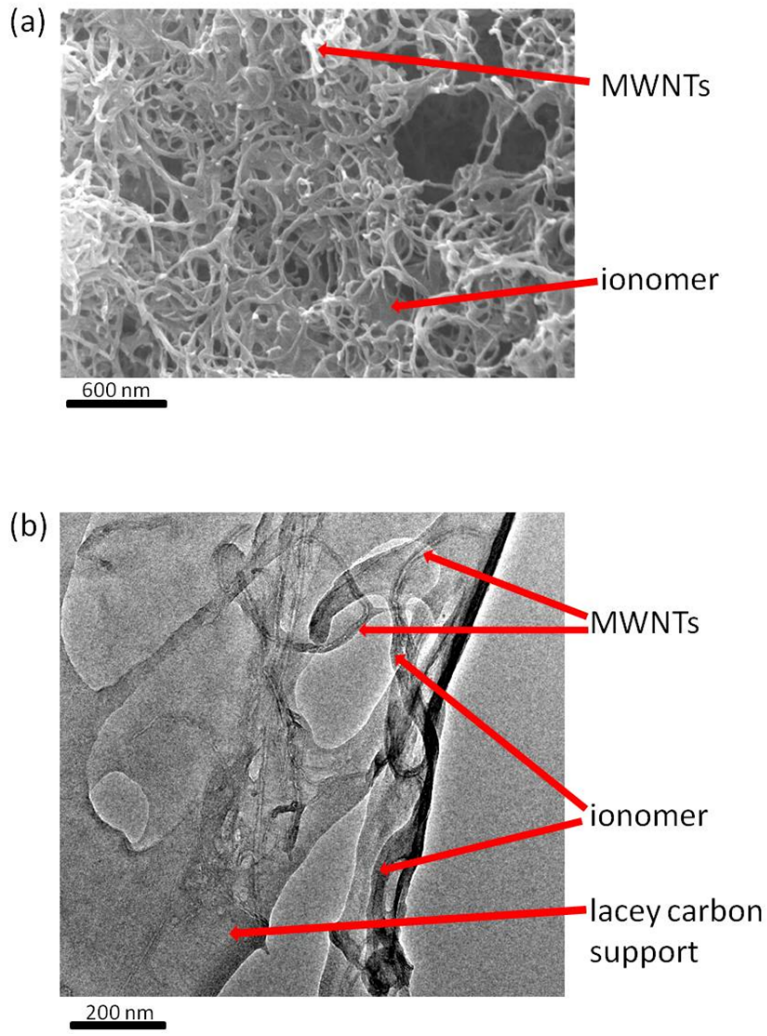


Figure 5.4: (a) Scanning electron micrograph of the spray deposited MWNT/ionomer hybrid electrode; and (b) transmission electron micrograph of the MWNTs with an ionomer coating.

ionomer coating over most of the MWNTs reduced any electron percolation through the membrane to a negligible effect, even at very slow scan rates. The ionomer also assisted H^+ mobility in the reverse direction of the electron movement to create more symmetrical voltammograms. However, there was now a pair of broad peaks superimposed on the normalised voltammograms at slow scan rates. Fig. 5.5(c) shows a plot of the height of these peaks as a function of the square root of scan rate up to 50 mV s^{-1} - beyond this,

the peak height became negligibly small compared with the EDL response. The data fitted closely to a linear relationship showing that the reaction was reversible at these comparatively slow scan rates and diffusion controlled [14] [15]. It is suggested that this reaction arises from interaction of the mobile H^+ ions (originating from the H_2SO_4 in the sprayed suspension and retaining in the ionomer) and the negatively charged F^- species present in the ionomer [16]. However, it should be emphasised that this redox-like activity was only significant at the slowest scan rates and the capacitance remained remarkably high at scan rates above 50 mV s^{-1}, where pseudo-capacitive effects were less influential and charge storage was dominated by the EDL behaviour at the interface between the H^+ conducting ionomer and the electron conducting MWNTs. The specific capacitance of a single cell with hybrid MWNT/ionomer electrodes estimated from the cyclic voltammograms was 145 F g^{-1} (41 mF cm^{-2}) per electrode at 2 mV s^{-1} and 91 F g^{-1} (26 mF cm^{-2}) at 150 mV s^{-1}, more than double the MWNT-only solid-state supercapacitor and now matching a MWNT electrode in a similar aqueous electrolyte.

Fig. 5.5(d) shows the corresponding DC galvanostatic charge/discharge curves at 1 A g^{-1} with an estimated capacitance of 92 F g^{-1} (26 mF cm^{-2}) and an IR drop of $\sim$0.12 V. As previously described for the cyclic voltammograms, the non-linearity in the charge/discharge curves was related to the redox activity in the electrodes at low current densities. Fig. 5.5(e) shows the corresponding Nyquist plot with an ESR now reduced from 19 Ω for the MWNT-only solid-state supercapacitor to 5.5 Ω, and with a

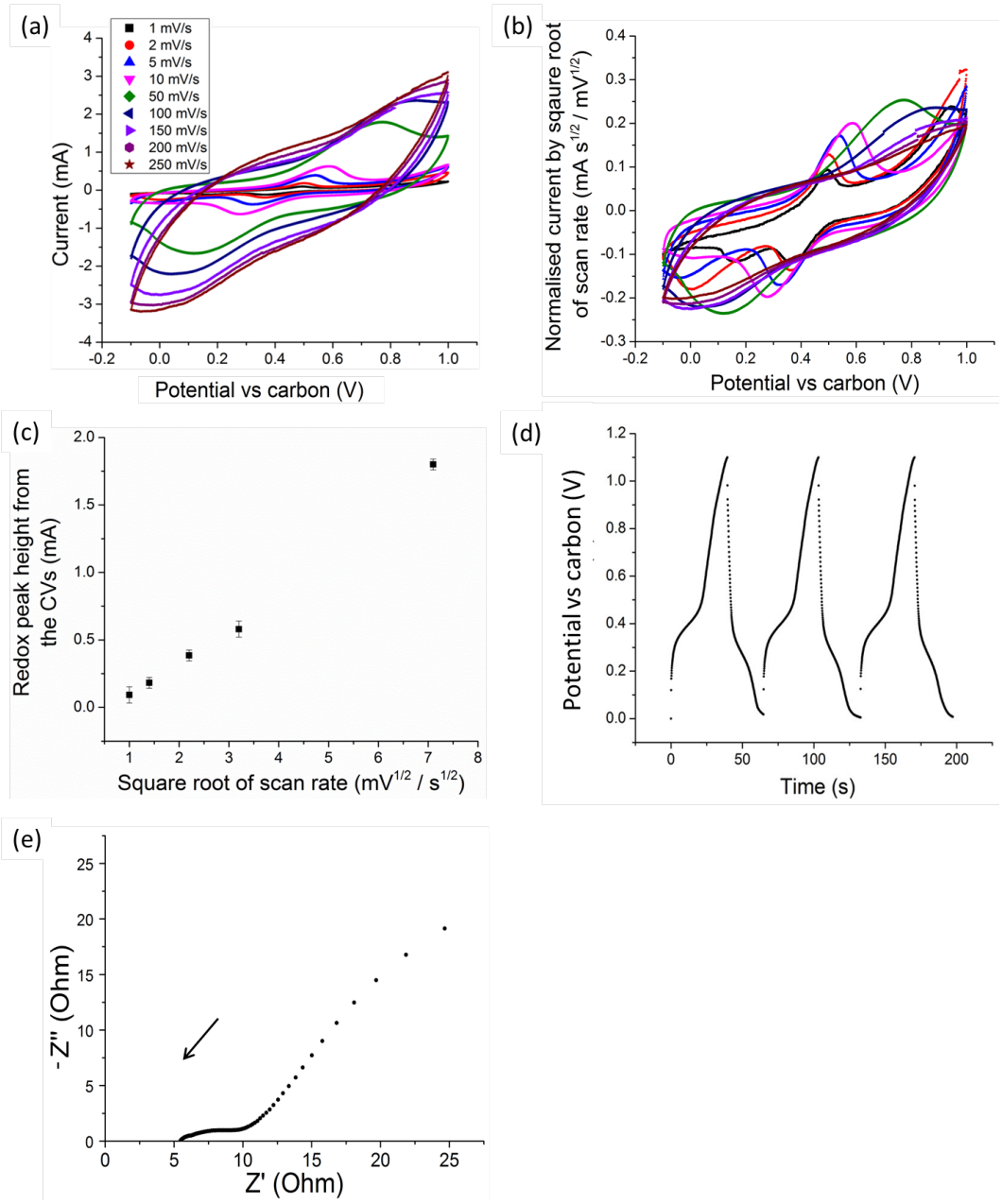


Figure 5.5: (a) Cyclic voltammograms of a full cell membrane-based solid-state supercapacitor with MWNT/ionomer electrodes; (b) the same voltammograms normalised by the square root of the scan rate; (c) a plot of redox peak height from the voltammograms in (a) against square root of scan rate; (d) DC galvanostatic charge/discharge curves of the same solid-state supercapacitor at 1 A g^{-1}; and (e) the complementary Nyquist impedance plot.

charge transfer resistance reduced from ∼180 Ω to ∼7 Ω.

Equivalent circuit models for the Nyquist impedance plots can be used to understand the resistive and capacitive elements of the solid-state supercapacitors [17]. Fig. 5.6(a) shows the equivalent circuit that the Nyquist plots of solid-state supercapacitors in Figs. 5.3(d) and 5.5(e) were fitted to [18] [19], where R_s represents the ESR, *CPE* is the constant phase elements which represent double-layer capacitance of porous electrodes [20], R_{CT} is the charge transfer resistance and W_d is the finite-length Warburg diffusion element which can be derived by solving Fick's laws with suitable initial and boundary conditions [20]. Fig. 5.6(b) shows that the fitted data approximately agreed with the experimental data for the solid-state supercapacitor with MWNT/ionomer hybrid electrodes.

The semi-circle in the Nyquist plot corresponded to the parallel combination of the constant phase elements *CPE* and charge transfer resistance R_{CT} in the equivalent circuit model. The R_{CT} was in series with a Warburg diffusion element W_d, which was responsible for the inclined tail in the Nyquist plot and was attributed to the ion diffusion inside the electrode and at the electrode/electrolyte interface [21] [22]. The *CPE* is used frequently in thin film electrodes to take into account the roughness and porosity of the electrodes as diffusion into the electrode material is the limiting process [23] [24]. The *CPE* is characterised by two parameters: admittance Y (reciprocal of impedance $\frac{1}{Z}$) and an exponent α (-1 $\leq \alpha \leq$ 1), both of which were calculated from

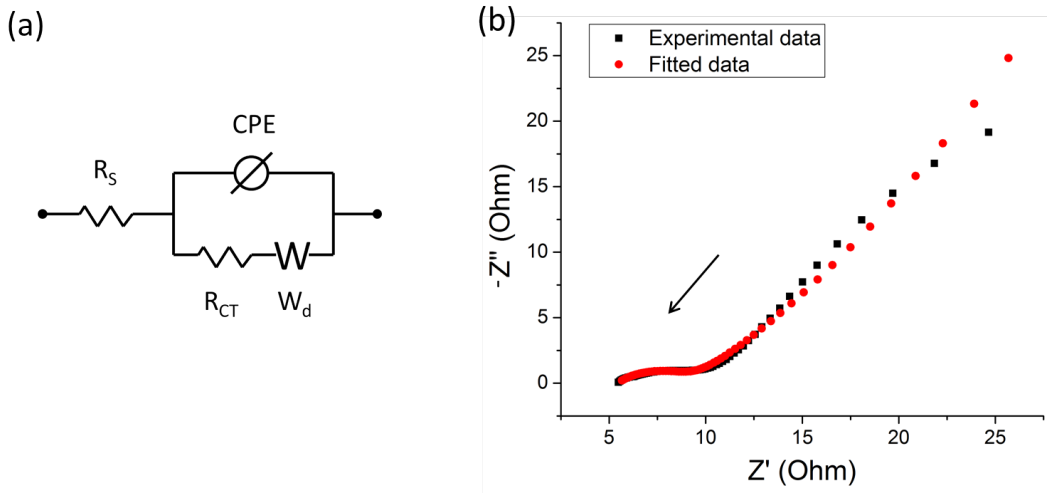


Figure 5.6: (a) Equivalent circuit model that the Nyquist plots of solid-state supercapacitors were fitted to; and (b) Nyquist impedance plot for the solid-state supercapacitor with MWNT/ionomer hybrid electrodes and the fitted data according to the equivalent circuit model in (a).

the equivalent circuit model. The admittance Y is related to the exponent α by:

$$Y = Q(i\omega)^{\alpha} \tag{5.1}$$

where Q is a coefficient, i is the imaginary unit and ω is the angular frequency ($\omega = 2\pi f$, where f is frequency) [25]. If $\alpha = 1$, the system represents an ideal capacitor [24]. Therefore, the closer α to 1, the more capacitive the behaviour is. It is possible to estimate the double layer capacitance from the admittance Y, however, the assumption is that the electrode is ideally polarisable, which is too simplifying and leads to errors [25]. Because of this error, this section instead focuses on the comparison of parameters between the two types of solid-state supercapacitors rather than estimating the double layer capacitance from the CPE model.

	$\mathbf{R}_S$ (Ω)	$\mathbf{Y}$ ($\mathbf{Ss}^n$)	α **(no units)**	$\mathbf{R}_{CT}$ (Ω)	$\mathbf{W}_d$ ($\mathbf{Ss}^{1/2}$)
MWNT-only electrodes	11.0	0.529 x 10^{-3}	0.4	144.3	3.3 x 10^{-3}
MWNT/ionomer hybrid electrodes	5.5	0.425 x 10^{-3}	0.6	3.4	2.8 x 10^{-2}

Table 5.1: Components of the equivalent circuit fitted for the impedance spectra for the solid-state supercapacitors with MWNT/ionomer hybrid electrodes and MWNT-only electrodes.

Table 5.1 shows the calculated values of R_s, R_{CT}, Y, α and W_d for both MWNT/ionomer hybrid and MWNT-only solid-state supercapacitors. Table 5.1 shows that the R_S values of 11.0 and 5.5 Ω calculated from the model were similar to the ESR obtained from the Nyquist plots in Figs. 5.3(d) and 5.5(e). The R_{CT} values of 144.5 and 3.4 Ω calculated from the model were also similar to the experimental data and may represent more accurately the charge transfer resistance within the electrodes in Figs. 5.3(d) and 5.5(e), rather than reading the semi-circle diameter from the Nyquist plots by eye. An $\alpha = 0.6$ was estimated by fitting to the model for the MWNT/ionomer hybrid supercapacitor, while $\alpha = 0.4$ for the MWNT-only version, demonstrating that the hybrid solid-state supercapacitor behaved more "ideally" than the MWNT-only, due to the enhanced charge transfer at the electrode/electrolyte interface on addition of the ionomer. The finite-length Warburg diffusion element W_d for the MWNT/ionomer electrodes was approximately 10 times that of the MWNT-only electrodes, showing faster ion movement in the formation of EDL in the hybrid electrodes [19].

An alternative approach is to assume the overall capacitive behaviour can be described by [26]:

$$C(\omega) = C'(\omega) - jC''(\omega) \tag{5.2}$$

where *C'* and *C"* are the real and imaginary parts of the capacitance C, which depends on frequency f: $\omega = 2\pi f$. Both *C'* and *C"* can be obtained from EIS by applying a small fluctuating voltage of ±5 mV, where *C"* relates to the energy dissipation in the system [26] [27].

From Equation 5.2:

$$C'(\omega) = \frac{-Z''(\omega)}{\omega|Z(\omega)|^2} \tag{5.3}$$

$$C''(\omega) = \frac{Z'(\omega)}{\omega|Z(\omega)|^2} \tag{5.4}$$

where *Z'* and *Z"* are the real and imaginary parts of the impedance and were obtained from the EIS measurements. In order to assess the effect of the ionomer addition on H^+ mobility, the relaxation time, also called the RC time constant τ_0, with and without ionomer was estimated. τ_0 can be obtained by plotting the variation of *C"* as a function of frequency, and determining the frequency f_0 at which *C"* was a maximum [26]. τ_0 is then obtained from $\tau_0 = 1/f_0$. τ_0 also indicates the median charge storage

efficiency [28] that relates to the time needed to charge an EDL capacitor to 63.2% of its final capacitance. Consequently, τ_0 is related to the ionic mobility within the system [26] [19] [29]. The MWNT-only and MWNT/ionomer cells gave $\tau_0 = 1.3$ s and $\tau_0 = 0.5$ s respectively, while $\tau_0 = 0.03$ s for the MWNT-only electrode in an aqueous H_2SO_4 electrolyte system. Portet *et al.* [27] reported $\tau_0 = 0.7$ s and 0.1 s for MWNT and carbon black electrodes respectively, in a liquid electrolyte of 1.5 M NEt_4BF_4 in acetonitrile. Therefore again the solid-state hybrid electrodes show remarkable ion mobility, approaching that of organic liquid electrolytes.

The energy density of one MWNT/ionomer electrode in a solid-state supercapacitor was 12.9 Wh kg^{-1} and the maximum power density was 3.3 kW kg^{-1}. Futaba *et al.* [30] reported an energy density of 13 Wh kg^{-1} for vertically aligned SWNT film electrode in liquid 1 M Et_4NBF_4/propylene carbonate organic electrolyte over a 2.5 V voltage window. Liu *et al.* [31] reported a maximum energy density of 0.5 Wh kg^{-1} and a maximum power density of 0.3 kW kg^{-1} for CNT-PANI nanocomposite electrodes with a PVA-H_3PO_4 gel electrolyte, and where the energy density was improved to 17 Wh kg^{-1} when TiO_2 nanoparticles were incorporated to introduce pseudo-capacitance [32]. Meng *et al.* [2] reported an energy density of 7.1 Wh kg^{-1} and a power density of 2.1 kW kg^{-1} for CNT-PANI nanocomposite electrode with a PVA-H_2SO_4 gel electrolyte, within a 0.8 V voltage window. Therefore, at the time of writing, the energy and power densities achieved here are competitive for solid-state supercapacitors that make use of EDL capacitance only, and are surprisingly competitive with liquid electrolyte-based

Electrode	**Testing environment**	**Capacitance (F g^{-1})**	**Energy density (Wh kg^{-1})**	**Power density (kW kg^{-1})**
MWNT	1 M H_2SO_4, half cell	86	12	3.4
MWNT	Solid-state configuration, full cell	44	6.1	1.1
MWNT/ionomer hybrid	Solid-state configuration, full cell	91	12.9	3.3

Table 5.2: A summary of the performances of MWNT-based electrodes in 1 M H_2SO_4 and in a solid-state symmetrical membrane-based cell configuration. All values were calculated per electrode.

equivalents. Table 5.2 summarises the specific capacitances, energy and power densities of the MWNT-based electrodes in both 1 M H_2SO_4 liquid electrolyte and in the full cell solid-state configuration, with all figures normalised to the performance of one electrode.

As mentioned in Chapter 2, aqueous electrolytes have limited voltage windows (typically ~1 V) if electrolysis of the water component is to be avoided [33]. Room temperature ionic liquids (RTILs) are complex liquid salts that are being intensively researched to provide a wider electrochemical stability (voltage) window without the need for air sensitive organic solvents [34]. However, solid-state supercapacitors also offer possibilities for a higher operating voltage window without resorting to organic liquids or RTILs since no solvents are required. As the energy and power densities depend on the operating voltage squared [26], even small increases in voltage are advantageous, providing increases in resistance are avoided. Fig. 5.7(a) shows DC galvanostatic charge/discharge curves for a solid-state supercapacitor with MWNT/ionomer electrode charged to 2 V, with little change in charging and discharging shape over time. Fig. 5.7(b) shows the energy and power densities achieved by the solid-state hybrid electrode supercapacitor,

charged across voltage windows in the range of 2 to 2.7 V at 1 A g^{-1}. For voltage windows larger than 3 V, polymer breakdown may occur.

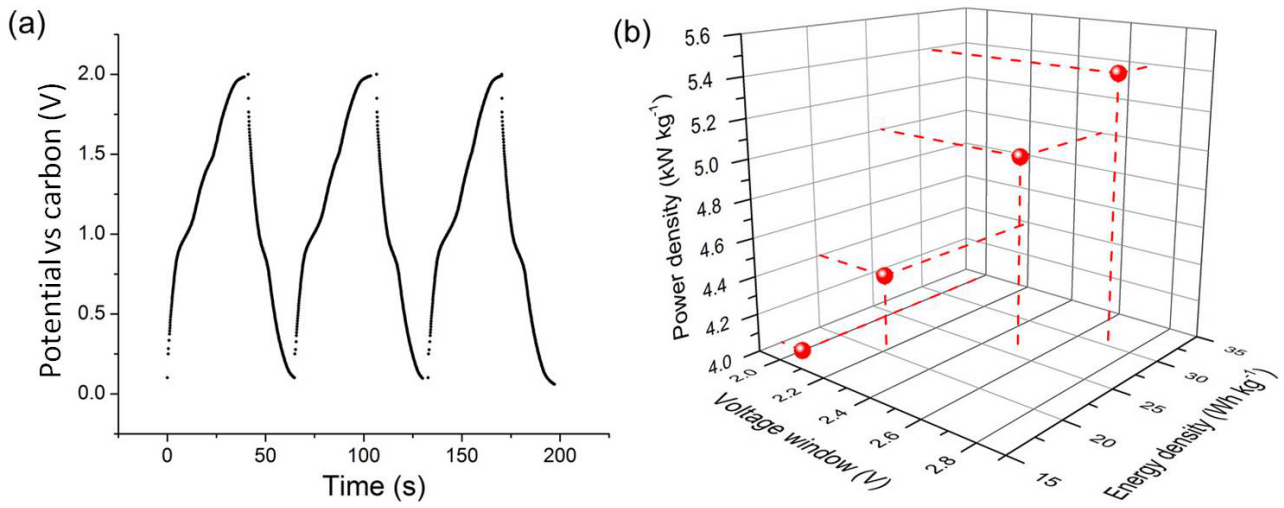


Figure 5.7: (a) DC galvanostatic charge/discharge curves charged to 2 V at 1 A g^{-1} for a full cell solid-state supercapacitor with MWNT/ionomer electrodes; and (b) specific energy and power densities against an increasing voltage window from 2 to 2.7 V.

Drawing on the microscopy and EIS studies, Fig. 5.8 shows a schematic diagram of the assumed solid-state supercapacitor structure with MWNT/ionomer hybrid electrodes, and suggests the manner in which the ionomer helped to improve dramatically the solid-state performance. With reference to Fig. 5.8, the enabling roles of the ionomer in improving capacitance and rate behaviour are:

1. H^+ ions from the H_2SO_4 solution used in spraying were retained and mobile within the ionomer coating on the MWNTs even under dry or low humidity conditions [35], while electrons readily moved along the MWNTs to the current collectors,

and around the external circuit. The ionomer coverage on the MWNTs was not uniform, as shown in Fig. 5.4(b), and there were sufficient MWNT-MWNT junctions for electron flow through the electrode. Any residual SO_4^{2-} ions were likely immobilised as the electrode was dried as part of the fabrication since neither the ionomer, the Nafion membrane or MWNTs provided a mechanism for SO_4^{2-} mobility [6].

2. Excellent wetting and physical contact between the coated MWNTs and the solid membrane is facilitated by the ionomer because the ionomer is chemically matched to the Nafion membrane and reduced the ion transfer resistance of H^+ [4, 19, 36]. The interaction between ionomer coated MWNTs and membrane was sufficiently strong that it could withstand moderate flexing and folding with no deterioration in performance.

5.3.4 Solid-state supercapacitor devices made of cell stacks

Connecting solid-state supercapacitors in series by stacking the cells together through current collectors allows a higher working voltage and increases specific power and energy densities. In most previous studies, the dimensions of the fabricated solid-state supercapacitor stacks were relatively small (e.g 5 mm x 5 mm in [32]), and scaling up towards the device scale posed difficulties in fabricating homogenous nanostructured electrodes over comparatively large areas, preventing short circuits over larger areas, etc. Staiti *et al.* [3] fabricated a 16 cm^2 five-cell stack. Here, 4.5 cm x 4 cm cells were

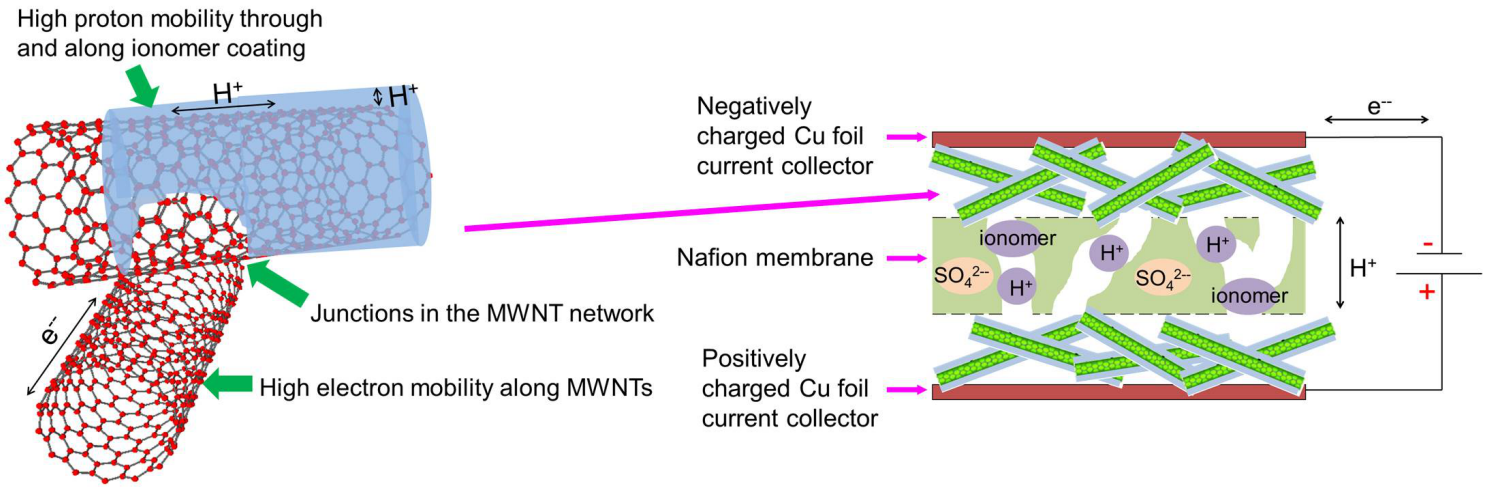


Figure 5.8: A schematic diagram of a full cell solid-state supercapacitor with a detailed structure of the MWNT/ionomer hybrid electrodes.

readily stacked at a scale consistent with a medium format mobile device.

Fig. 5.9(a) shows the cyclic voltammograms of two hybrid MWNT/ionomer solid-state supercapacitors connected in series. Although with some notable resistance, the voltammograms were parallelogram in shape even at a fast scan rate of 300 mV s^{-1}. The applied voltage should ideally be shared equally by each cell in the stack where resistances and capacitances are balanced [33], so stacks have advantages over single cells where fast scan rates and charging/discharging kinetics are required.

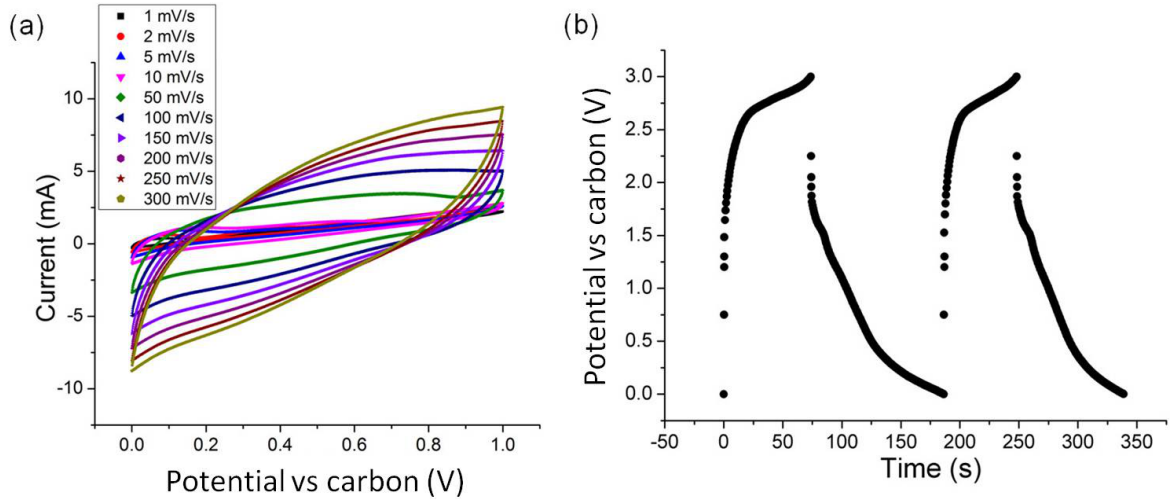


Figure 5.9: (a) Cyclic voltammograms of a stack of two solid-state supercapacitors connected through Cu foils at a variety of scan rates; and (b) DC galvanostatic charge/discharge curves of a stack of three solid-state supercapacitors charged to 3 V at a current density of 2 A g^{-1}.

Assuming each cell in the stack contributed the same capacitance, the capacitance of the stack can be estimated from [33]:

$$C_{stack} = \frac{C_{single}}{n} \tag{5.5}$$

where C_{stack} is the overall capacitance of the stack, C_{single} is the capacitance of each individual cell and n is the number of cells in the stack. Therefore, in a stack of 2 symmetrical cells, the overall capacitance of the stack is a half of that of a single cell [37]. The capacitance of the two-cell stack calculated from Fig. 5.9(a) at 150 mV s^{-1} was 0.2 F with an energy density of 23 Wh kg^{-1} and power density of 4.2 kW kg^{-1}. Comparison of the performance of this few-cell stack with the literature is difficult due to a lack of similar data, but the results are comparable with one of the highest reported capacitances of 0.21 F for a two-cell symmetrical supercapacitor stack, which used pseudo-capacitive MnO_x/acid treated CNTs electrodes and a 2 M KCl aqueous electrolyte [37].

Three cells were stacked in series and charged to 3 V at current densities of 1 and 2 A g^{-1} and Fig. 5.9(b) shows the galvanostatic charge/discharge curves for the three-cell stack. Because of the overall higher operating voltage, the IR drop increased to 0.75 V and marked resistance occurred after the voltage reached 2.7 V during charging, suggesting that loads may not be shared equally between the three cells. Nonetheless, the power density of the device was 8.9 kW kg^{-1} at 1 A g^{-1} and 9.4 kW kg^{-1} at 2 A g^{-1}, comparable with commercial supercapacitors operating at a similar voltage but with liquid organic electrolytes [11] [12]. The power density of the three-cell stack was

maintained at almost 100% after 200 cycles and at 88% after 2000 cycles.

5.4 Conclusions

In summary, solid-state supercapacitor cells have been fabricated by spraying a suspension of MWNTs and ionomer in a H^+ containing solution directly onto both sides of a Nafion membrane, which then acted as an electrically insulating but proton conducting separator. The resulting cell including Cu current collectors was 230 μm thick. The solid-state supercapacitors and their stack offered the advantages of easy packaging, and no leakage of electrolyte even under flexing. They were essentially chemically inert and required no special handling in a glove box or dry room.

The specific capacitance of a fully dried solid-state supercapacitor with MWNT/ionomer hybrid electrodes was 91 F g^{-1} per electrode at 150 mV s^{-1}, compared with 86 F g^{-1} for MWNTs in aqueous 1 M H_2SO_4. The energy density of one electrode charged to 1 V at 1 A g^{-1} was 12.9 Wh kg^{-1} and the power density was 3.3 kW kg^{-1}, which are the highest reported in a solid-state supercapacitor configuration with EDL-only capacitance. The comparatively fast kinetics and high capacitance arose because of an inter-penetrating meso-porous structure in which the MWNT scaffold offered a stable lattice for fast electronic conduction and long cycling; while the ionomer coating on the MWNTs provided complementary proton conduction and promoted chemical compatibility with the membrane-type separator.

A three solid-state-cell stack was charged to 3 V and provided a power density of 8.9 kW kg^{-1} at 1 A g^{-1} and 9.4 kW kg^{-1} at 2 A g^{-1}, comparable with commercial supercapacitors based on activated carbon and liquid inflammable organic electrolytes operating at a similar voltage. The power density of this three-cell stack was maintained at almost 100% after 200 cycles and at 88% after 2000 cycles.

Bibliography

[1] K. Naoi and M. Morita, "Advanced polymers as active materials and electrolytes for electrochemical capacitors and hybrid capacitor systmes," *The Electrochemical Society Interface*, pp. 44–48, Spring 2008.

[2] C. Meng, C. Liu, L. Chen, C. Hu, and S. Fan, "Highly flexible and all-solid-state paperlike polymer supercapacitors," *Nano Letters*, vol. 10, pp. 4025–4031, 2010.

[3] P. Staiti and F. Lufrano, "Design, fabrication, and evaluation of a 1.5 F and 5 V prototype of solid-state electrochemical supercapacitor," *Journal of the Electrochemical Society*, vol. 152 (3), pp. A617–A621, 2005.

[4] F. Lufrano and P. Staiti, "Performance improvement of nafion based solid-state electrochemical supercapacitor," *Electrochimica Acta*, vol. 49, pp. 2683–2689, 2004.

[5] F. Lufrano, P. Staiti, and M. Minutoli, "Evaluation of nafion based double layer capacitors by electrochemical impedance spectroscopy," *Journal of Power Sources*, vol. 124, pp. 314–320, 2003.

[6] M. Doyle, M. E. Lewittes, M. G. Roelofs, S. A. Perusich, and R. E. Lowrey, "Relationship between ionic conductivity of perfluorinated ionomeric membranes and nonaqueous solvent properties," *Journal of Membrane Science*, vol. 184, pp. 257–273, 2001.

[7] K.-D. Kreuer, "Proton conductivity: materials and applications," *Chemical Materials*, vol. 8, pp. 610–641, 1996.

[8] J. Zhang, L. Gao, J. Sun, Y. Liu, Y. Wang, J. Wang, H. Kajiura, Y. Li, and K. Noda, "Dispersion of single-walled carbon nanotubes by nafion in water/ethanol for preparing transparent conducting films," *Journal of Physical Chemistry C*, vol. 112, pp. 16370–16376, 2008.

[9] E. Frackowiak, K. Jurewicz, S. Delpeux, and F. Beguin, "Nanotubular materials for supercapacitors," *Journal of Power Sources*, vol. 97-8, pp. 822–825, 2001.

[10] Y. Wang, Z. Shi, Y. Huang, Y. Ma, C. Wang, M. Chen, and Y. Chen, "Supercapacitor devices based on graphene materials," *The Journal of Physical Chemistry C*, vol. 113, pp. 13103–13107, 2009.

[11] K. H. An, W. S. Kim, Y. S. Park, J.-M. Moon, D. J. Bae, S. C. Lim, Y. S. Lee, and Y. H. Lee, "Electrochemical properties of high-power supercapacitors using single-walled carbon nanotube electrodes," *Advanced Functional Materials*, vol. 11 (5), pp. 387–392, 2001.

[12] B. E. Conway, *Electrochemical Supercapacitors, Scientific Fundamentals and Technological Applications*. Kluwer Academic / Plenum Publishers, 1999.

[13] C. Du and P. Ning, "High power density supercapacitor electrodes of carbon nanotube films by electrophoretic deposition," *Nanotechnology*, vol. 17, pp. 5314–5318, 2006.

[14] F. Beguin and E. Frackowiak, eds., *Carbons for electrochemical energy storage and conversion systems*. CRC Press, 2010.

[15] W. G. Pell and B. E. Conway, "Analysis of power limitations at porous supercapacitor electrodes under cyclic voltammetry modulation and dc charge," *Journal of Power Sources*, vol. 96, pp. 57–67, 2001.

[16] J. A. Kerres, "Development of ionomer membranes for fuel cells," *Journal of Membrane Science*, vol. 185, pp. 3–27, 2001.

[17] B. Fang and L. Binder, "A novel carbon electrode material for highly improved EDLC performance," *Journal of Physical Chemistry B*, vol. 110, pp. 7877–7882, 2006.

[18] M. Stromme Mattsson, G. A. Niklasson, and C. G. Granqvist, "Li diffusion in Ti oxyfluoride films: thermal activation energy and jump length derived from impedance spectroscopy," *Journal of Applied Physics*, vol. 80, pp. 2169–2174, 1996.

[19] B. G. Choi, J. Hong, W. H. Hong, P. T. Hammond, and H. Park, "Facilitated ion transport in all-solid-state flexible supercapacitors," *ACS Nano*, vol. 5, pp. 7205–7213, 2011.

[20] C. Ho, I. D. Raistrick, and R. A. Huggins, "Application of a-c techniques to the study of lithium diffusion in tungsten trioxide thin films," *Journal of the Electrochemical Society*, vol. 127 (2), pp. 343–350, 1980.

[21] H. Li, J. Wang, Q. Chu, Z. Wang, F. Zhang, and S. Wang, "Theoretical and experimental specific capacitance of polyaniline in sulfuric acid," *Journal of Power Sources*, vol. 190, pp. 578–586, 2009.

[22] M.-W. Xu, D.-D. Zhao, and S.-J. Bao, "Mesoporous amorphous MnO_2 as electrode material for supercapacitor," *Journal of Solid State Electrochemistry*, vol. 11, pp. 1101–1107, 2007.

[23] R. Cabanel, G. Barral, J. P. Diard, B. Le Gorrec, and C. Montella, "Determination of the diffusion coefficient of an inserted species by impedance spectroscopy: application to the H/Hx Nb_2O_5 system," *Journal of Applied Electrochemistry*, vol. 23, pp. 93–97, 1993.

[24] J. Bisquert, G. Garcia-Belmonte, P. Bueno, E. Longo, and L. O. S. Bulhoes, "Impedance of constant phase element (cpe)-blocked diffusion in film electrodes," *Journal of Electroanalytical Chemistry*, vol. 452, pp. 229–234, 1998.

[25] P. Zoltowski, "On the electrical capacitance of interfaces exhibiting constant phase element behaviour," *Journal of Electroanalytical Chemistry*, vol. 443, pp. 149–154, 1998.

[26] P. L. Taberna, P. Simon, and J. F. Fauvarque, "Electrochemical characteristics and impedance spectroscopy studies of carbon-carbon supercapacitors," *Journal of the Electrochemical Society*, vol. 150 (3), pp. A292–A300, 2003.

[27] C. Portet, G. Yushin, and Y. Gogotsi, "Electrochemical performance of carbon onions, nanodiamonds, carbon black and multiwalled nanotubes in electrical double layer capacitors," *Carbon*, vol. 45, pp. 2511–2518, 2007.

[28] F. Beguin and E. Frackowiak, eds., *Supercapacitors - Materials, Systems, and Applications*. Wiley-VCH, 2013.

[29] K. S. Cole and R. H. Cole, "Dispersion and absorption in dielectrics I. alternating current characteristics," *The Journal of Chemical Physics*, vol. 9, pp. 341–351, 1941.

[30] D. N. Futaba, K. Hata, T. Yamada, T. Hiraoka, Y. Hayamizu, Y. Kakudate, O. Tanaike, H. Hatori, M. Yumura, and S. Iijima, "Shape-engineerable and highly densely packed single-walled carbon nanotubes and their application as supercapacitor electrodes," *Nature Materials*, vol. 5, no. 12, pp. 987–994, 2006.

[31] Q. Liu, M. H. Nayfeh, and S.-T. Yau, "Brushed-on flexible supercapacitor sheets using a nanocomposite of polyaniline and carbon nanotubes," *Journal of Power Sources*, vol. 195, pp. 7480–7483, 2010.

[32] Q. Liu, O. Nayfeh, M. H. Nayfeh, and S.-T. Yau, "Flexible supercapacitor sheets based on hybrid nanocomposite materials," *Nano Energy*, vol. 2, pp. 133–137, 2013.

[33] X. Zhou, C. Peng, and G. Z. Chen, "20 V stack of aqueous supercapacitors with carbon (-), titanium bipolar plates and CNT-polypyrrole composite (+)," *AIChE Journal*, vol. 58, pp. 974–983, 2012.

[34] D. Wei and T. W. Ng, "Application of novel room temperature ionic liquids in flexible supercapacitors," *Electrochemistry Communications*, vol. 11 (10), pp. 1996–1999, 2009.

[35] S. Y. Ahn, Y. C. Lee, H. Y. Ha, S. A. Hong, and I. H. On, "Effect of the ionomers in the electrode on the performance of pemfc under non-humidifying conditions," *Electrochimica Acta*, vol. 50, pp. 673–676, 2004.

[36] F. Lufrano and P. Staiti, "Conductivity and capacitance properties of a supercapacitor based on nafion electrolyte in a nonaqueous system," *Electrochemical and Solid-State Letters*, vol. 7, pp. A447–A450, 2004.

[37] S. Zhang, C. Peng, K. C. Ng, and G. Z. Chen, "Nanocomposites of manganese oxides and carbon nanotubes for aqueous supercapacitor stacks," *Electrochimica Acta*, vol. 55, pp. 7447–7453, 2010.

Chapter 6

Spray processing of TiO_2 nanoparticle/ionomer coatings on carbon nanotube scaffold-based electrodes for solid-state supercapacitors

6.1 Introduction

Chapter 5 listed the advantages of solid-state supercapacitors compared with their liquid electrolyte-based equivalents for applications such as flexible and wearable elec-

tronics, and described a solid-state supercapacitor with multi-wall carbon nanotube (MWNT)/ionomer hybrid electrodes on either side of a proton conducting Nafion membrane, fabricated by the spray deposition technique, achieving an electric double layer (EDL) capacitance of 145 F g^{-1} at 2 mV s^{-1} and 91 F g^{-1} at 150 mV s^{-1}, leading to a high power density of 9.4 kW kg^{-1} for a three-cell stack [1]. In this arrangement, the ionomer provided a mechanism for retained H^+ mobility within the electrode, and chemical compatibility with the separator, while the MWNTs allowed percolation of electrons through the electrode and easy transfer to the current collectors.

Now, to further increase energy storage, ∼30 nm anatase TiO_2 nanoparticles were added into the electrode. Although widely studied as a potential intercalation host in lithium ion battery (LiB) anodes and in dye-sensitised solar cells where it shows pronounced photo-electrochemical activity, TiO_2 is generally considered a poor supercapacitor material due to a poor electrical conductivity and the stability of the anatase structure [2, 3], e.g. 0.012 F g^{-1} in a 1 M $LiClO_4$/ethylene carbonate-diethylcarbonate electrolyte [4]. However, hybrid TiO_2-based composite electrodes have reached 912 F g^{-1} at 10 mV s^{-1} in aqueous Na_2SO_4 when the TiO_2 was hydrogen treated and mixed with MnO_2 due to induced pseudo-capacitance [5], but the charge storage mechanism and the explicit role of TiO_2 in energy storage in these supercapacitor arrangements is not usually clearly identified.

In this chapter, a flexible 4.5 cm x 4 cm and 110 μm thick solid-state supercapacitor with

MWNT/TiO_2/ionomer electrodes was fabricated by a similar procedure as described in Chapter 5, where an aqueous suspension of the constituents suspended/dissolved in 0.5 M H_2SO_4 was sprayed directly onto both sides of a Nafion membrane, which was heated at 100 °C throughout deposition to evaporate water as the meso-porous MWNT-based electrodes formed with no need for re-immersion in any liquid electrolyte. A much larger solid-state supercapacitor was fabricated by the same method to demonstrate scalability of the approach, as shown in Fig. 6.1. The 4.5 cm x 4 cm nano-hybrid solid-state supercapacitor provided both attractive energy (31.8 Wh kg^{-1}) and power (14.9 kW kg^{-1}) densities, enabled by the dispersion of TiO_2 into the ionomer, over the conducting MWNT scaffold.

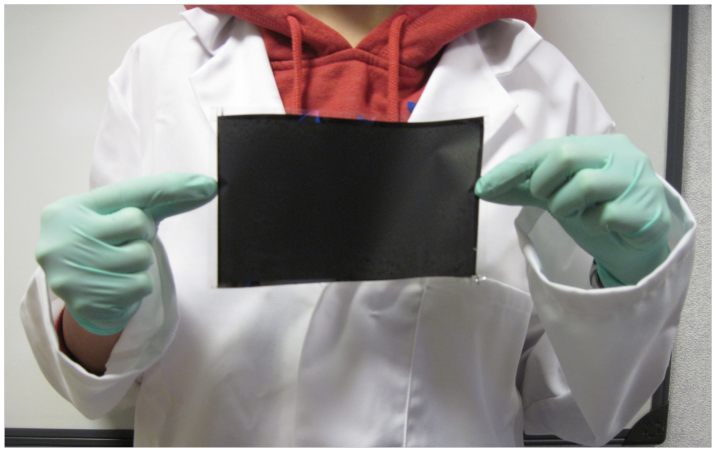


Figure 6.1: An as-sprayed 18 cm x 10 cm flexible solid-state supercapacitor (before addition of Cu foil current collectors).

6.2 Materials and methods

6.2.1 Fabrication of MWNT/TiO_2/ionomer solid-state supercapacitors by spray deposition

The spray processing method of fabricating MWNT/ionomer solid-state supercapacitors has been described in Chapter 5, and this section will mainly show the difference of adding TiO_2 nanoparticles into the hybrid electrodes.

Membranes (Nafion, 70μm thickness, Du Pont) were pre-treated by immersing in 1 M H_2SO_4 at 60 °C for 30 min. An aqueous suspension of 2 mg ml^{-1} MWNTs (Bayer MaterialScience), 1 mg ml^{-1} ~30 nm TiO_2 nanoparticles (Sigma-Aldrich), 0.1 wt% sodium dodecylbenzenesulfonate (SDBS, Sigma-Aldrich) and 50 wt% Nafion ionomer (Sigma-Aldrich) in 0.5 M H_2SO_4 was prepared by sonication at 600 W and 20 kHz for 15 min. The stable suspension was pumped at 3 ml min^{-1} into a spray head, and atomised using compressed air at 310 kPa to be deposited onto one side of the membrane which was maintained at 100 °C on a heating plate connected to a vacuum chuck with a total spray area of 20 cm × 20 cm. The membrane with one side covered with the sprayed electrode was flipped and sprayed on the other side using the identical procedure. The thickness of each electrode was controlled by the spray duration to be ~10 μm.

Cu foil current collectors of 10 μm thick were added onto the two sides of the test-

ing supercapacitors by gentle manual pressing. Indium tin oxide (ITO)-coated glass substrates (Sigma-Aldrich) with a 90% transmission rate of 300-1200 nm wavelengths were used as transparent current collectors for testing if the solid-state supercapacitor showed any photocatalytic effects, both under a Xenon lamp with a 200-800 nm wavelength range that mimics natural sunlight, and in darkness.

6.2.2 Characterisation

The surface chemistry of the as-received TiO_2 and sprayed electrode was analysed by X-ray photoelectron spectroscopy (XPS) in an ion pumped VG Microtech CLAM 4 multichannel detecting analyser equipped with a Mg K_α source. The XPS analyser operated at a constant pass energy of 100 eV for wide scans and 20 eV for detailed scans. The sprayed electrode chemistry was also investigated using Raman spectroscopy (Horiba LabRAM ARAMIS) with a 532 nm wavelength laser. The transmission behaviour of the ITO-coated glass substrates was measured by UV-Vis-NIR spectrophotometer (Varian Cary 5000) in a 200-1200 nm wavelength range. The surface morphology of the electrodes was examined by scanning electron microscopy (SEM, JEOL 840F at 3 kV), and transmission electron microscopy (TEM, JEOL 2010 at 200 kV and JEOL 3000F at 300 kV).

Cyclic voltammetry (CV) was performed over a range of scan rates from 5 to 500 mV s^{-1}, galvanostatic charge/discharge was measured at 1 V with a current density of 1

A g^{-1}, and electrochemical impedance spectroscopy (EIS) was performed from 0.01 to 10^6 Hz using an AC voltage of 5 mV rms.

To study the dehydration-rehydration behaviour of the solid-state supercapacitor with MWNT/TiO_2/ionomer electrodes, CV was performed in three conditions: (a) immediately after a cell was dehydrated in a vacuum oven at 105 ^{o}C for 16 hrs; (b) dehydration + the cell was exposed to air for 3 hrs; and (c) dehydration + the cell was hydrated over steam for 2 hrs.

6.3 Results and discussion

6.3.1 Electrode surface chemistry

Fig. 6.2 shows the Raman spectra for both as-sprayed MWNT-only and MWNT/anatase TiO_2 electrodes. Both spectra showed a G band at 1582 cm^{-1} corresponding to the -C-C- bond in the wrapped graphene plane, and a D band at 1330 cm^{-1} corresponding to the C-related defects within the as-received MWNTs. The 2D and G+D bands were typical for MWNTs [6]. The peaks in the 100-700 cm^{-1} region confirmed the presence of anatase TiO_2 with a dominating Eg mode at 147 cm^{-1} [7], indicating that as expected the as-sprayed nanocomposite electrode preserved the structures of both MWNTs and anatase TiO_2. The Raman spectrum was taken from the as-sprayed MWNT/TiO_2 electrode instead of a MWNT/TiO_2/ionomer electrode because the latter exhibited a

broad peak superimposing all other peaks due to the amorphous nature of the ionomer. It was therefore implicit in this approach that the ionomer had no significant chemical interaction with either MWNTs or TiO_2.

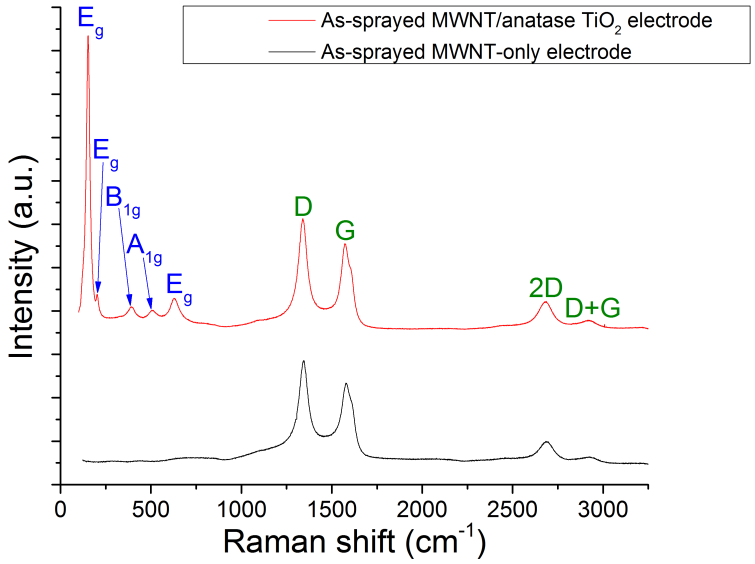


Figure 6.2: Raman spectra for an as-sprayed MWNT-only electrode and an as-sprayed MWNT/anatase TiO_2 electrode.

Figs. 6.3(a) and (b) show the XPS wide scan spectra for the as-received TiO_2 powder and the as-sprayed MWNT/TiO_2/ionomer electrode. Both spectra showed a strong Ti_{2p} peak at 459 eV and other peaks of Ti_{3p} and Ti_{3s} at 38 and 62 eV, indicating TiO_2 was incorporated into the as-sprayed electrode. The as-sprayed electrode in Fig. 6.3(b) also had a much stronger C_{1s} peak at 284 eV than Fig. 6.3(a) due to the presence of the MWNTs as the scaffold of the electrode; weak S peaks at 169 and 233 eV were due to retained dilute H_2SO_4 from the spray solution; F_{1s} at 689 eV was due to the end

groups of Nafion ionomer; and Na_{1s} at 1072 eV was due to a small amount of SDBS surfactant required for the MWNT dipersion.

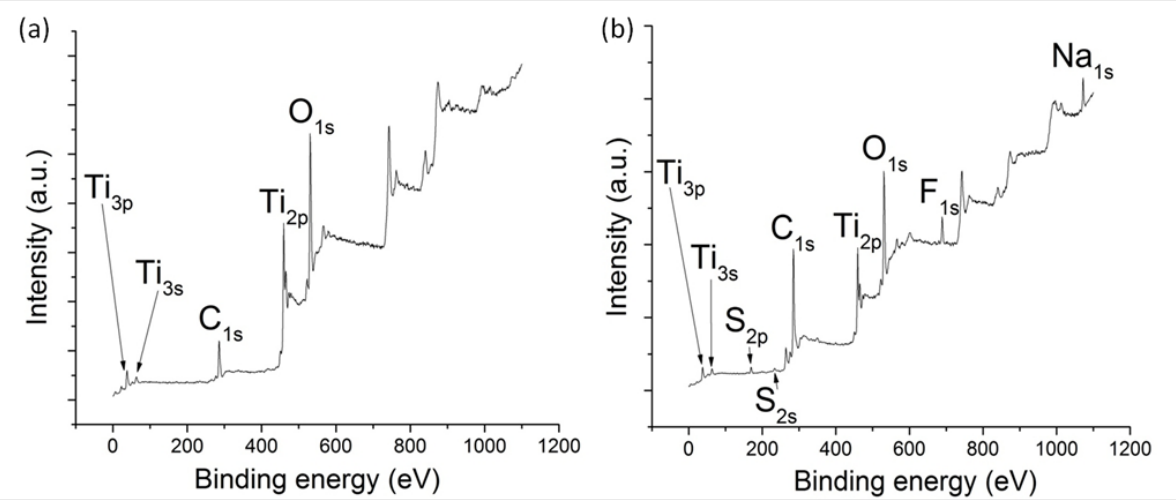


Figure 6.3: XPS spectra of (a) wide scan for the as-received TiO_2 powder; (b) wide scan for the as-sprayed MWNT/TiO_2/ionomer electrode.

Fig. 6.4(a) shows a detailed XPS Ti_{2p} spectrum for the as-received TiO_2 powder where the two peaks at 465 and 459.3 eV corresponded to the characteristic Ti $2p_{1/2}$ and Ti $2p_{3/2}$ peaks of Ti^{4+} [8], seen in all the as-sprayed electrodes. Fig. 6.4(b) compares the detailed O_{1s} spectra for the as-received TiO_2 powder, the as-sprayed MWNT/TiO_2/ionomer electrode and a dried then rehydrated (steam for 2 hrs) MWNT/ TiO_2/ionomer electrode. All spectra exhibited peaks at 530.5 eV corresponding to Ti-O-Ti and at 532.6 eV attributed to Ti-OH [5]. The peak area ratio of Ti-OH : Ti-O-Ti increased from 1:3 for the as-received TiO_2 to 2:3 for the as-sprayed electrode, indicating suspension in an aqueous-based solution during spraying increased hydroxyl group concentration on the TiO_2 surface [9]. The peak area ratio further increased to 7:5

for the rehydrated electrode, confirming adsorbed water molecules were responsible for surface OH groups.

6.3.2 Electrode microstructure

Fig. 6.5(a) shows an SEM micrograph of the as-sprayed MWNT/TiO_2/ionomer electrode with ∼30 nm TiO_2 nanoparticles adhered to the interconnected MWNTs in a number of locations within the scaffold. Fig. 6.5(b) shows a TEM micrograph of a cluster of TiO_2 nanoparticles adhered to some MWNTs thickened due to a coating of ionomer [1]. Fig. 6.5(c) is a high resolution TEM (HRTEM) image showing both the crystalline carbon nanotube multi-walls and a thin textured outer layer of ionomer coating on both MWNTs, and on the embedded TiO_2 nanoparticles.

6.3.3 Electrochemical characterisation of the solid-state supercapacitor

Fig. 6.6(a) shows the cyclic voltammograms of a solid-state supercapacitor arrangement with MWNT/ TiO_2/ionomer electrodes. The current increased readily at potential reversal for a wide range of scan rates, indicating fast charge/discharge kinetics, which is usually much more restricted in solid-state systems, e.g [10, 11]. The capacitance was 484 F g^{-1} per electrode at 5 mV s^{-1} (85 mF cm^{-2}) and 322 F g^{-1} at 100 mV s^{-1} (57 mF

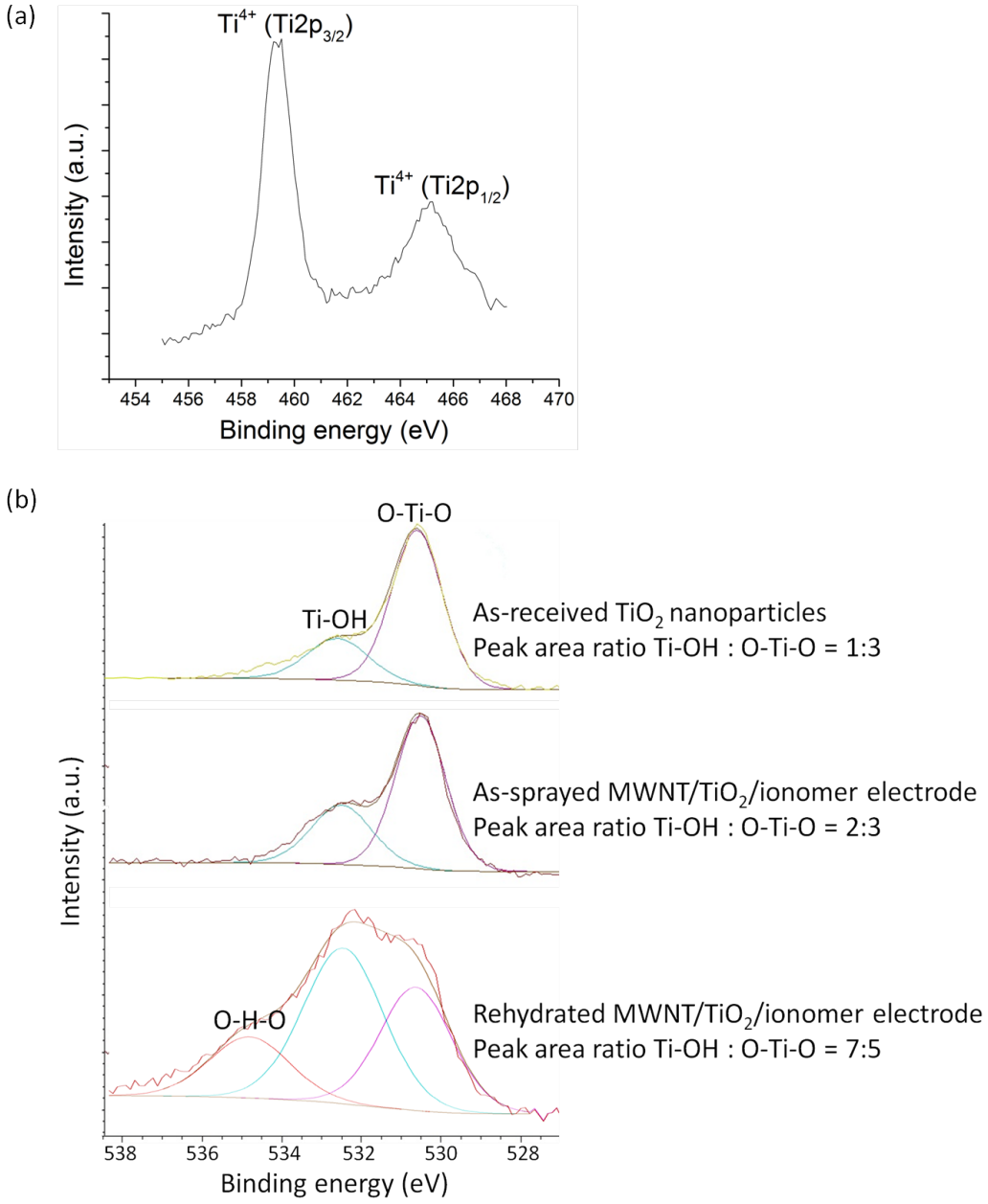


Figure 6.4: XPS spectra of (a) detailed Ti_{2p} scan for the as-received TiO_2 nanoparticles; and (b) detailed O_{1s} scan for as-received TiO_2 powder, as-sprayed MWNT/TiO_2/ionomer electrode and dried then rehydrated MWNT/TiO_2/ionomer electrode.

cm^{-2}). A capacitance of 118.5 F g^{-1} at 1 A g^{-1} was reported for a solid-state supercapacitor with reduced graphene oxide electrodes and a H_2SO_4 treated Nafion membrane

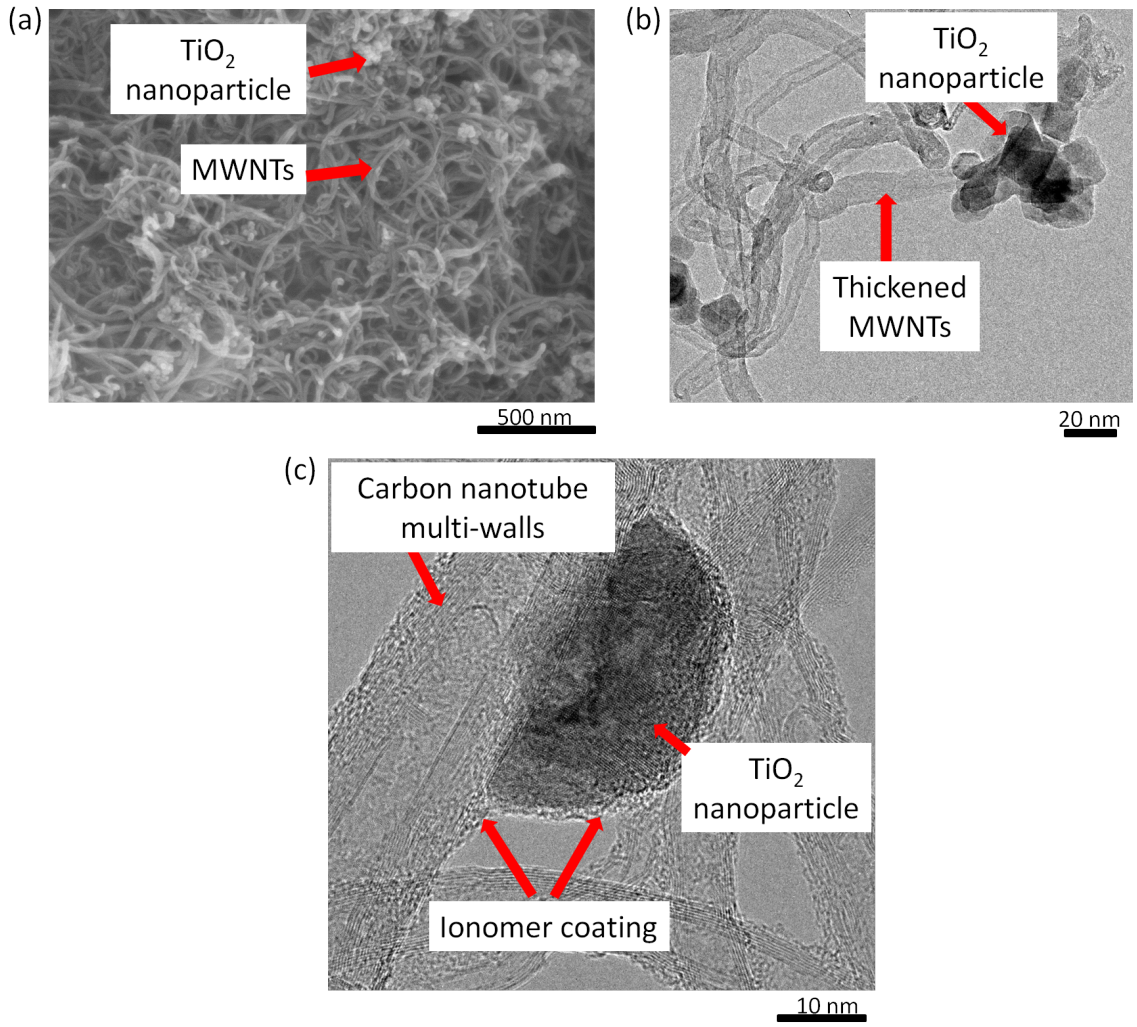


Figure 6.5: (a) SEM image of the as-sprayed MWNT/TiO_2/ionomer electrode; (b) TEM image of the electrode; and (c) HRTEM image of the MWNTs and a TiO_2 nanoparticle partially covered with an ionomer coating.

separator [12]. At the time of writing, the capacitance in this paper is the highest for a solid-state supercapacitor based on either EDL capacitance, pseudo-capacitance or their combination.

The superimposed peaks in the CV curves at ~0.3 and ~0.4 V in Fig. 6.6(a) were due

to the redox activity of hydroxyl group attached to Ti (as shown by the XPS data in Fig. 6.4(b)), where adsorbed water molecules from the spray solution were dissociated at an oxygen vacancy at/near TiO_2 surface to form an -OH group, and one remaining proton was transferred to a neighbouring oxygen atom creating another -OH group [13]. Some hydroxyl groups were further dissociated to H^+ and O^{2-} [14]. These redox reactions directly led to pseudo-capacitance according to [9]:

$$H_2O \rightarrow H^+ + OH^- \tag{6.1}$$

$$OH^- \rightarrow H^+ + O^{2-} \tag{6.2}$$

Fig. 6.6(b) is the cyclic voltammograms of the same supercapacitor after 300 cycles, with fading redox peak height, leaving a more marked EDL-like parallelogram shape, typical of liquid electrolyte-based supercapacitors but not usually seen in solid-state supercapacitors. Nonetheless, capacitance remained high at 320 F g^{-1} at 5 mV s^{-1} (56 mF cm^{-2}) and 229 F g^{-1} at 100 mV s^{-1} (40 mF cm^{-2}), decreasing by only 9.8% at 2000 cycles. The high performance arose from the high concentration of H^+ ions generated by the hydroxyl reaction catalysed in the TiO_2 that were able to rapidly reach the TiO_2 surface through intrinsic lattice oxygen vacancies [15]. Attracted by the negatively charged -SO_2F- end groups in the ionomer coating on the MWNT/TiO_2, these H^+ ions, along with the H^+ ions which were already available from retained acidic solution, were comparatively mobile in the ion-conducting ionomer coating.

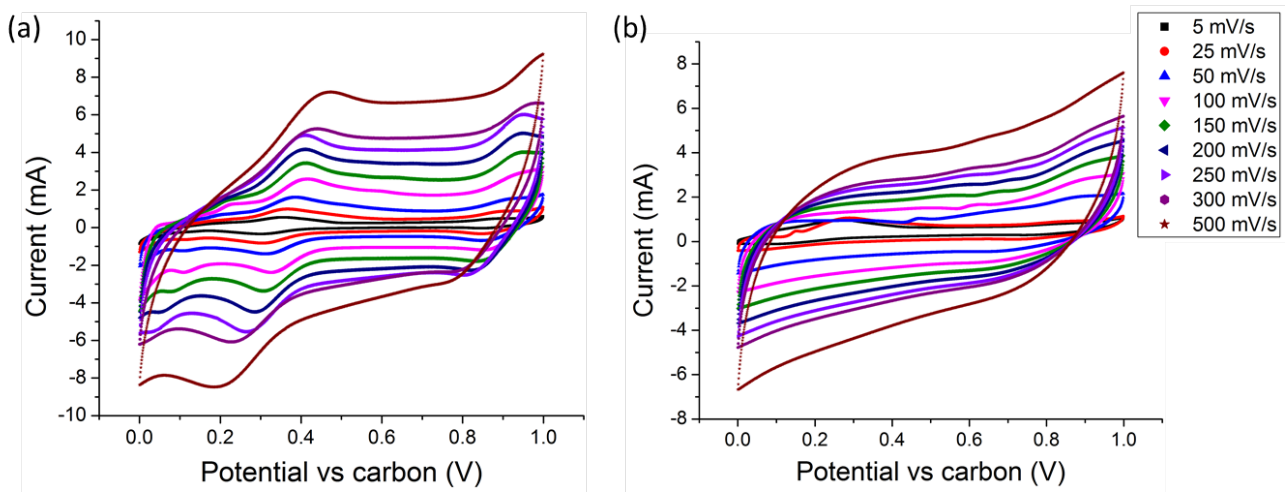


Figure 6.6: (a) Cyclic voltammograms of a solid-state supercapacitor with MWNT/TiO_2/ionomer electrodes; and (b) cyclic voltammograms of the same solid-state supercapacitor after 300 cycles when the hydroxyl group reaction faded.

Fig. 6.7(a) shows the corresponding galvanostatic charge and discharge cycles at 1 A g^{-1}, with an estimated capacitance of 460 F g^{-1} (81 mF cm^{-2}). The majority of the curves was linear showing fast charging/discharging kinetics, and the non-linearity at 0.3-0.4 V corresponded with the hydroxyl group redox reactions, at a similar cyclic voltammogram peak position in Fig. 6.6(a). Fig. 6.7(b) shows one charge/discharge cycle for the symmetric solid-state supercapacitors with MWNT/TiO_2/ionomer, MWNT/ionomer and MWNT-only electrodes, all at 1 A g^{-1}, demonstrating that the MWNT/TiO_2/ionomer electrode stored ∼three times the charge of the MWNT/ionomer, and ∼five times of the MWNT-only electrodes.

Fig. 6.8(a) shows the corresponding Nyquist plot with an estimated equivalent series

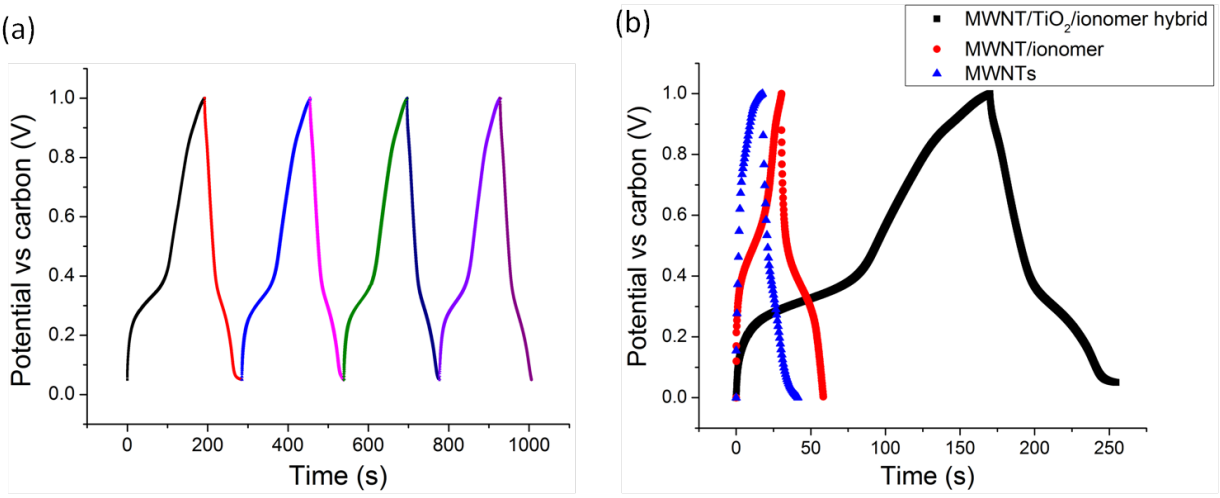


Figure 6.7: (a) Galvanostatic charge/discharge cycles of a solid-state supercapacitor with MWNT/TiO_2/ionomer electrodes at 1 A g^{-1}; and (b) galvanostatic charge/discharge curves of the symmetric solid-state supercapacitors with MWNT/TiO2/ionomer, MWNT/ionomer and MWNTs-only electrodes, all at 1 A g^{-1}.

resistance (ESR, intersection on the real axis at high frequency) of 2.5 Ω compared with 5.5 Ω for the MWNT/ionomer and a charge transfer resistance (the semi-circle diameter) of 1.8 Ω compared with 7 Ω for the MWNT/ionomer in Chapter 5, showing a decrease in resistance at the electrode/electrolyte interface [12]. In order to investigate ion mobility directly, as used in Chapter 5, the imaginary capacitance *C"* was studied as a function of frequency by using EIS [1, 16, 12]. The relaxation time τ_0 relates to the time needed to charge a supercapacitor to 63.2% of its final capacitance [17] and was obtained from the frequency f_0 at which the imaginary part of the capacitance *C"* was a maximum, and where $f_0=1/\tau_0$, as shown in Fig. 6.8(b). τ_0 was reduced to 0.3 s for the solid-state configuration with MWNT/TiO_2/ionomer electrodes from 1.3 s and 0.5 s for MWNT-only and MWNT/ionomer electrodes respectively [1], supporting an

increase in H^+ mobility in the presence of TiO_2.

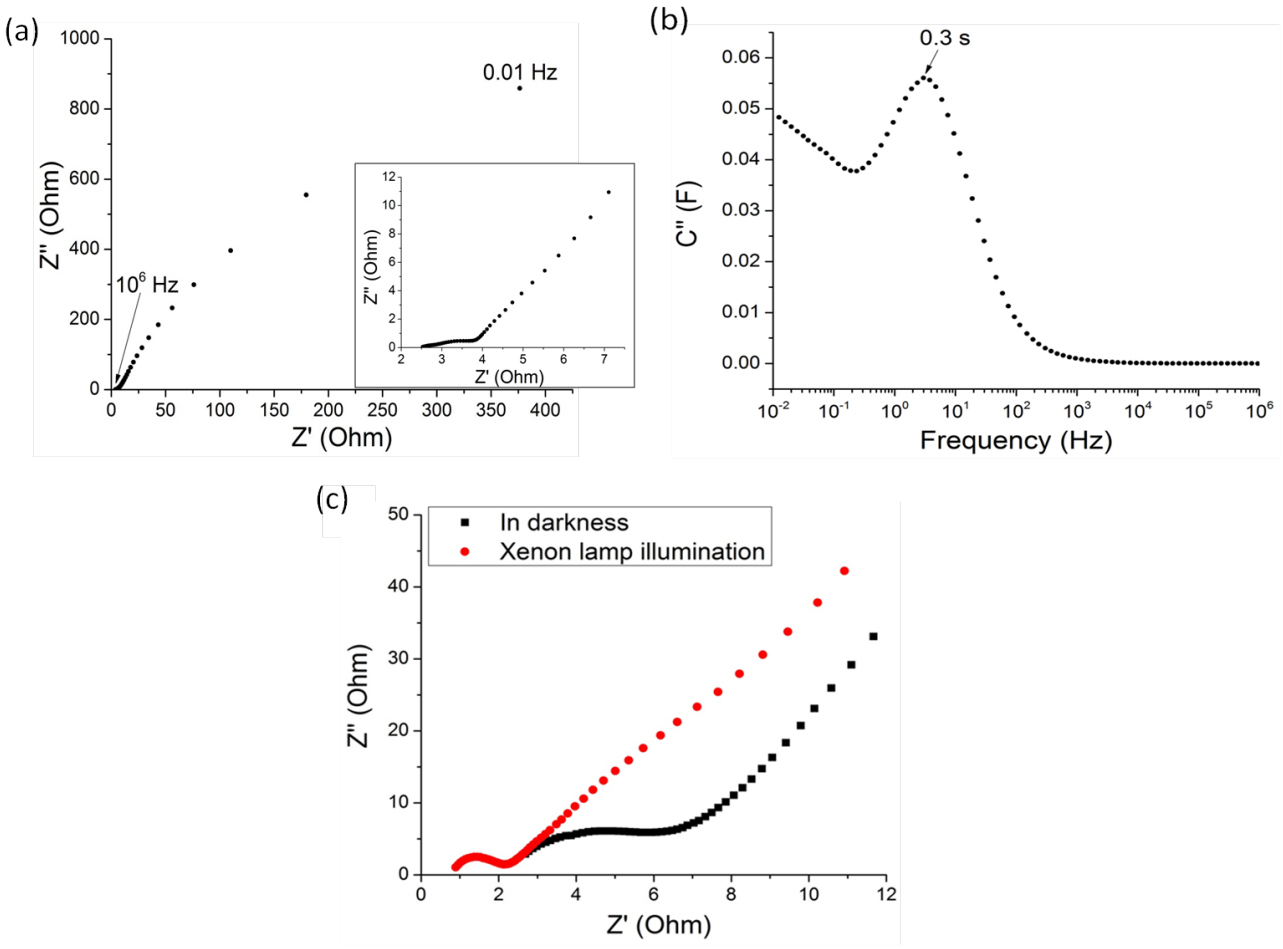


Figure 6.8: (a) Nyquist plot of a solid-state supercapacitor with MWNT/TiO_2/ionomer electrodes between 10^6 Hz and 0.01 Hz under normal light; (b) a graph of imaginary part of the capacitance vs frequency from the EIS results in (a) to estimate relaxation time τ_0; and (c) Nyquist plots in the high frequency region of a solid-state supercapacitor with MWNT/TiO_2/ionomer electrodes tested under a Xenon lamp and in darkness.

To study the effect of light on the solid-state supercapacitor with MWNT/TiO_2/ionomer electrodes, Fig. 6.8(c) shows the Nyquist plots for the cell tested under light and in darkness. The ESR decreased from 2.7 to 0.8 Ω and the charge transfer resistance

decreased from 5.2 to 1.3 Ω from in darkness to under light, respectively, showing "sunlight" reduced the resistance of the hybrid electrode and slightly enhanced a continuous presence of electrons in the conduction band in TiO_2 [18]. In addition, the large EDL capacitance achieved in the electrodes may be contributed by the increase in the conduction band electron concentration as EDL performance is mainly governed by the conduction band electrons rather than valence band electrons of the electrode material [19].

To study dehydration-rehydration behaviour, a cell was left in vacuum at 105 ^{o}C (within the stable ionomer temperature range [20, 14]) for 16 hrs. Fig. 6.9(a) shows the CV curves with no charge storage, indicating all water molecules and hydroxyl groups had evaporated. Fig. 6.9(b) shows the same CV curves after the cell was exposed to laboratory air on the bench for 3 hrs, indicating some recovery of mobile H^+ behaviour and EDL-type response, with a capacitance of 10% of the pristine capacitance. When more fully rehydrated over steam for 2 hrs, Fig. 6.9(c) shows the re-appearance of redox peaks associated with hydroxyl groups, which was confirmed by XPS in Fig. 6.4(b). The capacitance returned to 22% of the pristine capacitance. Fig. 6.9(d) shows a plot of normalised peak current from Fig. 6.9(c) against square root of scan rate, which can be used to show the restored pseudo-capacitive contribution of an electrode material in a system, according to [2]:

$$i/v^{1/2} = k_1 v^{1/2} + k_2 \tag{6.3}$$

where $v^{1/2}$ is the square root of scan rate, $i/v^{1/2}$ is the normalised peak current by the square root of scan rate, k_1 is a constant corresponding to the pseudo-capacitive contribution, and k_2 is a constant corresponding to the EDL capacitive contribution. The data in Fig. 6.9(d) fitted closely to a linear relationship showing that the normalised peak current was proportional to the square root of scan rate, indicating that the reaction was diffusion controlled and pseudo-capacitive [2]. The current response at the fastest scan rate of 500 mV s^{-1} was not used as the scan time was too fast for redox reactions to complete. The linear relationship and a k_1 slope gradient of 0.01 confirmed that the role of adsorbed water and its dissociation in the presence of TiO_2 underpinned the pseudo-capacitance. However, the CV curves now deviated more strongly from a parallelogram shape, showing that the aggressive dehydration/steam treatment apparently led to some irreversible damage and increase in device resistance.

As described in Chapter 2, metal oxide-based supercapacitors normally provide a high energy density but compromised power density, whereas carbon-based supercapacitors provide higher power densities with a lower energy density. Fig. 6.10 is a Ragone plot of power density against energy density for the performance of commercial supercapacitors and LiBs, and different types of solid-state supercapacitors taken from the recent literature [21, 22, 23]. Here, the solid-state supercapacitor with MWNT/TiO_2/ionomer

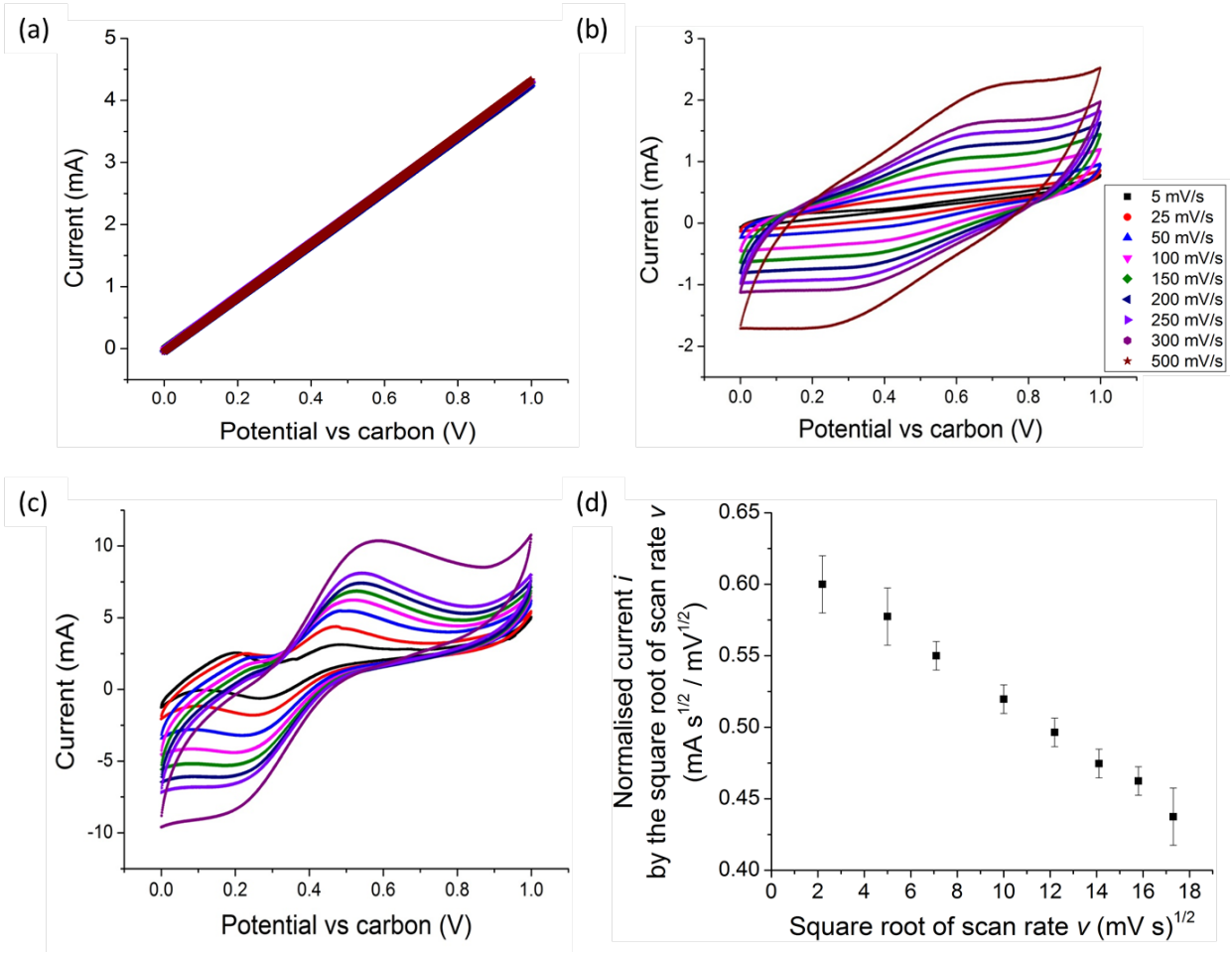


Figure 6.9: (a) Cyclic voltammograms of the a solid-state supercapacitor immediately after dehydrating in vacuum at 105 ^{o}C for 16 hrs; (b) cyclic voltammograms of (a) after exposing to laboratory air on the bench for 3 hrs; (c) cyclic voltammograms of (a) after rehydrating over steam for 2 hrs; and (d) a plot of CV normalised peak current in (c) against the square root of scan rate.

electrodes yielded an attractive combination of energy density of 31.8 Wh kg^{-1} and power density of 14.9 kW kg^{-1}.

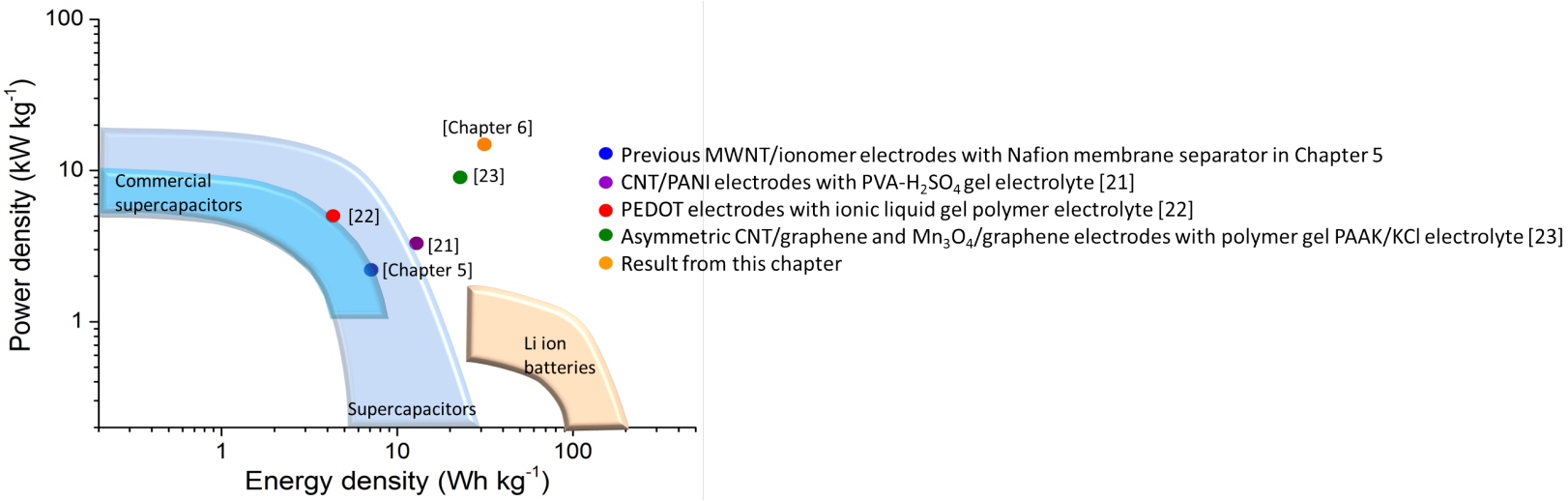


Figure 6.10: A Ragone plot of power density against energy density for supercapacitors and LiBs, and different types of solid-state supercapacitor performances taken from the literature, where PANI is an abbreviation of polyaniline [21], PEDOT is poly(3,4-ethylenedioxythiophene) [22] and PAAK is potassium polyacrylate [23].

In summary, solid-state supercapacitors with MWNT/TiO_2/ionomer electrodes by spray processing provided a virtuous combination of both electronic and protonic conduction without the need for a liquid electrolyte. Critically, the TiO_2 catalysed pseudo-capacitive hydroxyl reactions, facilitating mobile proton generation, as shown in Fig. 6.11. H^+ ion mobility throughout the electrode was then facilitated by the ionomer coating that covered both the TiO_2 nanoparticles and MWNTs. Nonetheless, electrons were still able to move readily through the electrically percolating MWNT network and across the electrode-current collector interface.

6.4 Conclusions

Solid-state supercapacitors with MWNT/TiO_2/ionomer electrodes were fabricated by the spray deposition processing method. Very high capacitances of 484 F g^{-1} per electrode at 5 mV s^{-1} and 322 F g^{-1} at 100 mV s^{-1} were achieved, boosted by a reversible redox pseudo-capacitive reaction of hydroxyl groups in TiO_2 nanoparticles, that facilitated mobile proton generation. After 300 CV cycles, the redox reaction faded but the solid-state supercapacitor still achieved a high EDL capacitance of 320 F g^{-1} at 5 mV s^{-1} and 229 F g^{-1} at 100 mV s^{-1}, maintaining for 2000 cycles with an only 9.8 % capacitance decrease.

The supercapacitor cell showed that irradiation under sunlight may increase the conduc-

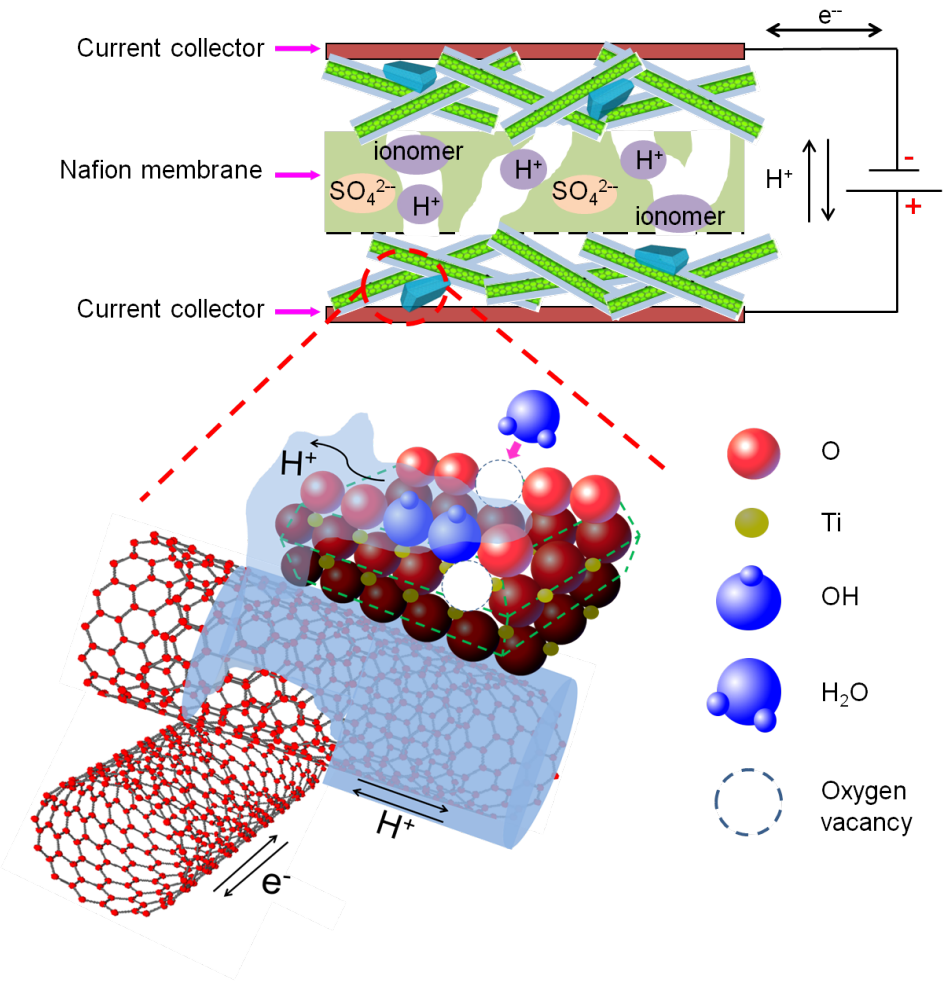


Figure 6.11: A schematic diagram of the MWNT/TiO_2/ionomer solid-state supercapacitor full cell and the hybrid electrode structure in detail to show the pseudo-capacitive reaction in the TiO_2 nanoparticle to generate H^+, which was transported by the ionomer coating on both of the nanoparticles and MWNTs.

tion band electron concentration in TiO_2 and reduce the electrode internal resistance, but there was no significant effect on the energy stored. Dehydration-rehydration behaviour confirmed that hydroxyl groups were involved in the high pseudo-capacitance in the presence of TiO_2, and this mechanism has been successfully exploited in a solid-state supercapacitor arrangement for the first time. The arrangement was scalable to 10's of centimetres easily, and the working device could be exposed to ambient air

and moisture with little/no packaging, while providing attractive long term cycling behaviour.

Bibliography

[1] C. Huang and P. S. Grant, "One-step spray processing of high power all-solid-state supercapacitors," *Scientific Reports*, vol. 3 : 2393, p. DOI: 10.1038/srep02393, 2013.

[2] J. Wang, J. Polleux, J. Lim, and B. Dunn, "Pseudocapacitive contributions to electrochemical energy storage in TiO_2 (anatase) nanoparticles," *Journal of Physical Chemistry C*, vol. 111, pp. 14925–14931, 2007.

[3] Y. Xie, L. Zhou, C. Huang, H. Huang, and J. Lu, "Fabrication of nickel oxide-embedded titania nanotube array for redox capacitance application," *Electrochimica Acta*, vol. 53, pp. 3643–3649, 2008.

[4] H. Liang, F. Chen, R. Li, L. Wang, and Z. Deng, "Electrochemical study of activated carbon-semiconducting oxide composites as electrode materials of double-layer capacitors," *Electrochimica Acta*, vol. 49 (21), pp. 3463–3467, 2004.

[5] X. Lu, G. Wang, T. Zhai, M. Yu, J. Gan, Y. Tong, and Y. Li, "Hydrogenated TiO_2 nanotube arrays for supercapacitors," *Nano Letters*, vol. 12, pp. 1690–1696, 2012.

[6] M. Zdrojek, W. Gebicki, C. Jastrzebski, T. Melin, and A. Huczko, "Studies of multiwall carbon nanotubes using raman spectroscopy and atomic force microscopy," *Solid State Phenomena*, vol. 99, pp. 265–268, 2004.

[7] G. Liu, H. G. Yang, X. Wang, L. Cheng, H. Lu, L. Wang, G. Q. M. Lu, and H.-M. Cheng, "Enhanced photoactivity of oxygen-deficient anatase TiO_2 sheets with dominant 001 facets," *Journal of Physical Chemistry C*, vol. 113, pp. 21784–21788, 2009.

[8] D. Briggs and J. T. Grant, eds., *Surface analysis by Auger and x-ray photoelectron spectroscopy*. IM Publications, 2003.

[9] B. Chen, J. Hou, and K. Lu, "Formation mechanism of TiO_2 nanotubes and their applications in photoelectrochemical water splitting and supercapacitors," *Langmuir*, vol. 29, pp. 5911–5919, 2013.

[10] B. E. Grancisco, C. M. Jones, S. Lee, and C. R. Stoldt, "Nanostructured all-solid-state supercapacitor based on Li_2S-P_2S_5 glass-ceramic electrolyte," *Applied Physics Letters*, vol. 100, pp. 103902–1–4, 2012.

[11] J. Zhou, J. Cai, S. Cai, X. Zhou, and A. N. Mansour, "Development of all-solid-state mediator-enhanced supercapacitors with polyvinylidene fluoride/lithium trifluoromethanesulfonate separators," *Journal of Power Sources*, vol. 196, pp. 10479–10483, 2011.

[12] B. G. Choi, J. Hong, W. H. Hong, P. T. Hammond, and H. Park, "Facilitated ion transport in all-solid-state flexible supercapacitors," *ACS Nano*, vol. 5, pp. 7205–7213, 2011.

[13] R. Schaub, P. Thostrup, N. Lopez, E. Lagsgaard, I. Stensgaard, J. K. Norskov, and F. Besenbacher, "Oxygen vacancies as active sites for water dissociation on rutile $TiO_2(110)$," *Physical Review Letters*, vol. 87 (26), p. 266104, 2001.

[14] E. Chalkova, M. B. Pague, M. V. Fedkin, D. J. Wesolowski, and S. N. Lvov, "Nafion/TiO_2 proton conductive composite membranes for PEMFCs operating at elevated temperature and reduced relative humidity," *Journal of the Electrochemical Society*, vol. 152 (6), pp. A1035–A1040, 2005.

[15] T. Norby, "Proton conduction in solids: bulk and interfaces," *MRS Bulletin*, vol. 34, pp. 923–928, 2009.

[16] P. L. Taberna, P. Simon, and J. F. Fauvarque, "Electrochemical characteristics and impedance spectroscopy studies of carbon-carbon supercapacitors," *Journal of the Electrochemical Society*, vol. 150 (3), pp. A292–A300, 2003.

[17] F. Beguin and E. Frackowiak, eds., *Supercapacitors - Materials, Systems, and Applications*. Wiley-VCH, 2013.

[18] P. M. Sommeling, H. C. Reiffe, J. A. M. van Roosmalen, A. Schonecker, J. M. Kroon, J. A. Wienke, and A. Hinsch, "Spectral response and iv-characterization of

dye-sensitized nanocrystalline TiO_2 solar cells," *Solar Energy Materials and Solar Cells*, vol. 62 (4), pp. 399–410, 2000.

[19] B. E. Conway, *Electrochemical Supercapacitors, Scientific Fundamentals and Technological Applications*. Kluwer Academic / Plenum Publishers, 1999.

[20] C. Heitner-Wirguin, "Recent advances in perfluorinated ionomer membrans: structure, properties and applications," *Journal of Membrane Science*, vol. 120, pp. 1–33, 1996.

[21] C. Meng, C. Liu, L. Chen, C. Hu, and S. Fan, "Highly flexible and all-solid-state paperlike polymer supercapacitors," *Nano Letters*, vol. 10, pp. 4025–4031, 2010.

[22] G. P. Pandey and A. C. Rastogi, "Solid-state supercapacitors based on pulse polymerized poly(3,4-ethylenedioxythiophene) electrodes and ionic liquid gel polymer electrolyte," *Journal of the Electrochemical Society*, vol. 159 (10), pp. A1664–A1671, 2012.

[23] H. Gao, F. Xiao, C. B. Ching, and H. Duan, "Flexible all-solid-state asymmetric supercapacitors based on free-standing carbon nanotube/graphene and Mn_3O_4 nanoparticle/graphene paper electrodes," *Applied Materials & Interfaces*, vol. 4, pp. 7020–7026, 2012.

Chapter 7

Conclusions and Future Work

7.1 Conclusions

This thesis has focused on using a scalable spray deposition technique to fabricate both film electrodes and flexible solid-state supercapacitors based on single wall carbon nanotubes (SWNTs) and multi-wall carbon nanotubes (MWNTs).

Layer-by-layer (LbL) spray deposition was used to fabricate SWNT-COOH/SWNT-NH_2 electrodes. The LbL electrode showed a 65% increase in density and a 38% increase in electrical conductivity compared with a pure SWNT electrode. The LbL electrode tested in a 1 M H_2SO_4 electrolyte exhibited a pronounced electric double layer (EDL) capacitance of 94 F g^{-1} at 2 mV s^{-1}, compared with 29 F g^{-1} for a pure SWNT electrode and 63 F g^{-1} for a SWNT-COOH electrode, which was due to the high conductivity and compact structure of the LbL electrode, facilitating faster charging/discharging

kinetics and more active area per unit volume.

Heating the LbL electrode in vacuum at 150 ^{o}C for 30 mins and in a H_2 atmosphere at 300 ^{o}C for 2 hrs removed the functional groups and unzipped some SWNTs to form multi-layer graphene sheets. These heat treatments increased the capacitance further to 151 F g^{-1} at 2 mV s^{-1} and 118 F g^{-1} at 100 mV s^{-1}. The three-dimensional scaffold structure formed by 1D SWNTs and 2D multi-layer graphene sheets offered a combination of basal plane (exposed by the SWNTs) and edge plane (exposed by the multi-layer graphene sheets) carbon, and enhanced the overall capacitance.

Symmetric solid-state supercapacitors were then fabricated by spraying a suspension of MWNTs and ionomer in a dilute version of the H_2SO_4 electrolyte directly onto both sides of a Nafion membrane, ensuring the H^+ ions fed into all parts of the interior of the electrode to promote electrolyte wetting and ion adsorption. The specific capacitance of a fully dried solid-state supercapacitor with MWNT/ionomer electrodes was 145 F g^{-1} per electrode at 2 mV s^{-1} and 91 F g^{-1} at 150 mV s^{-1}, compared with 57 F g^{-1} at 2 mV s^{-1} and 44 F g^{-1} at 150 mV s^{-1} for the MWNT-only electrodes. The energy density of the MWNT/ionomer electrode charged to 1 V at 1 A g^{-1} was 12.9 Wh kg^{-1} and the power density was 3.3 kW kg^{-1}. The comparatively fast kinetics and high capacitance arose because of an inter-penetrating meso-porous structure in which the MWNT scaffold offered a stable lattice for fast electronic conduction and long cycling; while the ionomer coating on the MWNTs provided complementary proton conduc-

tion and promoted chemical compatibility with the membrane-type separator. A three solid-state-cell stack was charged to 3 V and provided a power density of 8.9 kW kg^{-1} at 1 A g^{-1} and 9.4 kW kg^{-1} at 2 A g^{-1}. The power density of this three-cell stack was maintained at almost 100% after 200 cycles and at 88% after 2000 cycles.

TiO_2 nanoparticles were then incorporated into the electrodes by the same spray deposition technique to fabricate solid-state supercapacitors. Very high capacitances of 484 F g^{-1} per electrode at 5 mV s^{-1} and 322 F g^{-1} at 100 mV s^{-1} were achieved, due to a redox reaction between the hydroxyl group on the TiO_2 nanoparticles and surface adsorbed water molecules, producing an extra number of protons which were retained and mobile through TiO_2 vacancies and fed into the ionomer coating on the MWNTs and TiO_2 nanoparticles. After free water molecules were removed, the solid-state supercapacitor still exhibited a high EDL capacitance of 320 F g^{-1} at 5 mV s^{-1} and 229 F g^{-1} at 100 mV s^{-1}, maintained at 90% after 2000 cycles.

Light and dehydration recoverability of the cell were tested to show that sunlight may increase the conduction band electron concentration in TiO_2 and reduce the electrode internal resistance and a severely dehydrated cell was able to recover EDL behaviour by simply exposing to air. Pseudo-capacitive behaviour was recovered by rehydrating a dehydrated cell over steam.

The pristine solid-state supercapacitor with MWNT/TiO_2/ionomer electrodes provided

a combination of high energy (31.8 Wh kg^{-1}) and power (14.9 kW kg^{-1}) densities at 1 A g^{-1}, which is the one of the highest reported for solid-state supercapacitos at the time of writing.

7.2 Suggestions for future work

The spray processing route may be developed towards fabricating solid-state Li-ion batteries (LiBs). For the anodes, anatase TiO_2 or Si nanoparticles or nanorods may be used as both have high theoretical capacities (e.g 4200 mAh g^{-1} for Si [1]). Two main challenges are the relatively low electron transport and limited cyclability due to the repeating volumetric changes during charging and discharging. Spraying three-dimensional electrodes of carbon nanotube (CNT) scaffold decorated or interconnected with TiO_2 or Si nanoparticles or nanorods may be suitable for the LiB anode with a high electron transport and the ability to accommodate large strain without pulverisation.

Bibliography

[1] C. K. Chan, H. Peng, G. Liu, K. McLwrath, X. F. Zhang, R. A. Huggins, and Y. Cui, "High-performance lithium battery anodes using silicon nanowires," *Nature Nanotechnology*, vol. 3, pp. 31–35, 2008.